Aalborg University

Titania and copper based Polystyrene Nanocomposite Materials and Investigation of their Antibacterial Properties

Supervisors:
Vladimir Popok
& Peter Fojan
Assoc. Professors
Department of Physics and
Nanotechnology

Submitted By :
Cesarino Mario Jeppesen

Declaration of Authorship

I, Cesarino Mario Jeppesen, declare that this thesis titled, ‘Titania and copper based Polystyrene Nanocomposite Materials and Investigation of their Antibacterial Properties’ and the work presented in it are my own. I confirm that:

- This work was done wholly or mainly while in candidature for a research degree at this University.
- Where any part of this thesis has previously been submitted for a degree or any other qualification at this University or any other institution, this has been clearly stated.
- Where I have consulted the published work of others, this is always clearly attributed.
- Where I have quoted from the work of others, the source is always given. With the exception of such quotations, this thesis is entirely my own work.
- I have acknowledged all main sources of help.

Signed: ____

Date: ____

"If you thought that science was certain - well, that is just an error on your part.."

Richard Feynman.

Abstract

The work carried out in this thesis investigates the application of Metal-polymer nanocomposites in order to find a possible solution of the recurring issue of bacterial infection. For this thesis, Copper clusters are produced using the magnetron sputtering cluster apparatus (MaSCA) and then are deposited onto quartz and silicon substrates coated by a Polystyrene (PS) film of desired thickness. Titania nanoparticles are prepared using the gas aggregation cluster source (GAS) in Prague and are also deposited unto quartz and silicon substrates coated by a thin film of PS. Thermal annealing, after cluster deposition, is used to control the immersion depth of clusters into the PS films. Furthermore these prepared samples are then characterized using Atomic Force microscopy (AFM) and Scanning Electron Microscopy (SEM) and optical measurements before the samples are subjected to antimicrobial tests. The second part of the project then focuses on the bactericidal effects of the prepared samples. Herein the techniques used to assess the antimicrobial effects include Colony Forming Units (CFU) plate counting, as well as Fluorescence microscopy using molecular probes to observe morphological damage to the bacterial cells. As will be discussed later, the efficiency of the prepared substrates depends on the different bactericidal mechanism. Also investigated is the degree to which the substrates can be reused in order to give an insight to the killing efficiency over time.

Preface

This paper is composed by group 5.242, 9-10th semester nanobiotechnology student at the Department of Physics and Nanotechnology at Aalborg University. The main theme of this masters project is entitled *Characterization of nanobio structures* with this project focusing on *Titania and copper based Polystyrene Nanocomposite Materials and Investigation of their Antibacterial Properties.*

References in this report are made as fig. x.y, tab. x.y, sec. x.y, eq. x.y, etc. for figures, tables, sections and equations respectively. Sources are cited by number of the form [x].

The report is divided into three parts; *Introduction* covering introduction to the paper and selected theory, *Materials and methods* covering which and how experiments are executed and lastly *Results and discussion* covering the results from the experiments, as well as a discussion and a conclusion.

The work presented in this thesis has been conducted at the Department of Physics and Nanotechnology at Aalborg University. HoweverTitanium Nanoparticle (TiNP) were deposited in collaboration with the Department of Condensed Matter Physics, Charles University Prague, Czech Republic. Furthermore Copper Nanoparticle (Cu NP) are deposited by, Florian Ceynowa, a fellow masters student enrolled at the Department of Physics and Nanotechnology at Aalborg University .

Special thanks is given to **Florian Ceynowa**, who was responsible for the deposition of Copper clusters.

The work presented in this thesis is in part based on the previous report that also dealt with he production and characterization of polymer metal based nanocomposites [1]. This was done in collaboration with Svetomir T. Hitov a fellow masters student enrolled at the department of Physics and Nanotechnology in Aalborg University.

I would in particular also like to express my deepest gratitude towards my supervisors Peter Fojan and Vladimir Popok for their guidance, and support throughout the duration of this thesis.

CESARINO MARIO JEPPESEN

10/06/17

Contents

Chapter 1

Introduction

Nanotechnology is one of the scientific fields that promises great opportunities for developing new and advanced technologies that can improve our way of life and solve a number of increasing problems in health care, environment, food industry. Since the fundamental article by [2], nanotechnology has advanced tremendously.

In recent years the growing concern of antibiotic resistance of bacteria has presented a major problem. This problem continues to grow each year due to widespread use of antibiotic to treat bacterial infections, which leads to proportional increase in antibiotic resistance. Because of the selective pressure, these resistant microorganisms have a greater chance of survival and growth [3, 4]. In addition medical devices are susceptible to bacterial colonization which in turn leads to implant related infections as well as Urinary Track (UT) and Respiratory Track Infectionss (RTIs). These infections hinder the long term use of such medical devices which due to bacterial colonization of the polymer surface leads to the formation of biofilms. Biofilms, defined as matrix-enclosed microbial accretions [5], have inherent property to adhere to biological and non-biological surfaces. Furthermore, their not entirely elucidated development and dynamic behavior makes destroying them difficult[6].Systematic therapies can be applied to treat these device related infections, but remain ineffective due to the use of a high concentration of antibiotics whereby these biofilms are resistant to antibiotic treatment as well as host defense mechanisms. [7] An alternative approach is exemplified by designing medical device surface properties in order to moderate interfacial interactions between these devices and host tissue. This will in turn curb adhesion of bacteria to human tissue surfaces and implanted biomedical devices [7–9]. In hospital a environment, this problem manifests itself as catheter associated infections and Urinary Track Infectionss (UTIs) that are, among other things, a result of the presence of bacterial biofilms catheter surfaces, medical implants and devices [3, 5].

Further understanding in antibacterial properties of nanoparticles has lead to application of nanoparticles in fighting bacterial infections and contaminations. The antibacterial property has been linked to the surface to volume ratio of nanoparticles. This Surface Area (SA) to volume ratio enhances the biological and chemical activity by increasing the contact area of Nano particles (NPs) with microorganisms [10]. The sizes of NPs is also a key factor which enables their relatively easy penetration into bacterial cells [11, 12]. The SA to volume ratio of NPs is a useful property in the development of nanocomposites among include antimicrobial coatings for application in medical devices [13–16].
Studies have also shown that highly reactive metal oxide NPs exhibit biocidal action against Gram-positive and Gram-negative bacteria [17, 18]. The penetration, characterization and surface modification of nanosized inorganic particles present the possibility for a new generation of bactericidal materials that circumvent the growing antibiotic resistance and cost of using antibiotics [11].

For this report, the antibacterial activity of Copper and Titanium Dioxide NPs will be investigated using strain a of *Escherichia coli*. Nanotoxicity will be monitored upon the exposure of the bacterial strains to NPs embedded in thin Polystyrene (PS) films. The microorganisms will be cultured in liquid media and once exposed to the NPs, and UV in the case of TiO_2 NP, the growth kinetics will be observed by estimating the number of Colony Forming Units (CFU) after incubation. Prior to antibacterial tests the polymer films will be spin coated, on two different substrates, i.e. silicon and quartz, with a thickness of 50 nm. The Cu NPs and TiO_2 NPs will be fabricated and embedded on the surface of the polymer film using cluster beam technique, in particular Magnetron Sputtering Cluster Apparatus (MaSCA). The bactericidal experiments are carried out to test whether or not Polymer nanocomposites are an alternative approach in treating the problems mentioned above in order to circumvent the use of antibiotics.

Chapter 2

Metal-polymer Composites and Bacterial Growth

2.1 Cluster-beam Technique

2.1.1 Cluster Formation

An accepted definition of a cluster that of an aggregate that is made up of a quantified number of constituents, which can either be atoms or molecules. In this context a countable number of particles refers to 2-10^n, with n being an integer of magnitude 6 or 7. Furthermore when the integral particles are one refers to such a system as being homo-atomic (or homo-molecular) and in the case when the constituents are not identical the system is referred to as being hetero-atomic (or hetero-molecular). Clusters have gained interest as they are considered to constitute a new type of material due to their characteristic properties which differ from their bulk counterparts [19].

The formation of clusters can be subdivided into four fundamental stages:

- Vaporization – in this stage atoms or molecules are produced in the gas phase. Due to the rapid cooling of the gas supersaturation occurs which in turn leads to the formation and growth of the clusters from the excess vapor.

- Nucleation –Second stage is formation of a cluster nucleus by the condensation of molecules or atoms.
- Growth – during this stage more molecules or atoms are added to the initially formed nucleus and the cluster thereby increases in size. Contrary to the growth procedure, clusters can also shrink as a result of evaporation or fragmentation.
- Coalescence – During this process, smaller clusters merge in order to form even larger clusters.

[20]. The nucleation probability of a cluster at thermal equilibrium is usually very small and therefore requires a thermal non-equilibrium that is brought about by the various cluster sources (Magnetron sputtering, Laser vaporization e.t.c). During this nucleation process clusters of a stable phase are formed from the metastable state, the supersaturated vapor of the material, that leads to the formation of a cluster nucleus from initial collision of atoms. Theoretically if the thermal energy of the beam is less than the binding energy of the dimer, then a triple atom collision results in the formation of a dimeric nucleus whereby the excess energy released is removed by the third atom (from an inert gas) eq. (2.1) and the dimer nucleus acts as a site for further cluster growth.
At first growth is achieved by the addition of individual atoms to the dimer nucleus and followed by subsequent growth via coalescence. However due to the fact that addition of more atoms is an exothermic process, there exists a competition between the growth and decay of the clusters. During this phase clusters can therefore shrink by losing individual atoms or can undergo fragmentation. Hence to make the nucleation process more favorable to cluster growth a carrier gas is injected into the nucleation chamber. Cooling is therefore achieved when the cluster losses energy by colliding with other atoms that possess higher kinetic energy eq. (2.2).

$$A + A + A(kE_1) \;\rightarrow\; A_2 + A(kE_2 > kE_1) \tag{2.1}$$

$$A_N(T_1) + B(kE_1) \;\rightarrow\; A_N(T_2 < T_1) + B(kE_2 > kE_1) \tag{2.2}$$

where B can be an inert carrier gas atom. Clusters, in addition, can also lower their internal energy by ejecting one or more atoms from the cluster which is known as endothermic desorption process [20, 21].

Different cluster sources can be implemented in order to provide a thermal non-equilibrium that influence the size distribution of clusters generated, these include: the Knudsen cell, Supersonic (free Jet) Nozzle Sources, Laser Vaporization-Flow Condensation Source, Pulsed-Arc Cluster Ion Source, Ion Sputtering Source, Magnetron Sputtering Source, Gas-Aggregation/smoke Source amongst others.

For this project the magnetron sputtering source is used to produce both the copper and titania clusers .In magnetron sputtering a plasma is first ignited typically using argon over a target where a D.C or R.F potential is applied and further confined using a magnetic field. The argon ions are then accelerated onto the desired target resulting in sputtering and ejection of the target material. Similarly secondary electrons are also emitted and contribute to the plasma ionization. Confinment of the secondary electrons using the magnetic field in turn increases the propability that ionization occurs leading to a denser plasma and higher rate of sputtering [22]. In addition aggregation of atoms is facilitated by adding an inert gas, for example helium as described previously.
As for the TiO_2 NPs, the Gas Aggregation Cluster Source (GAS) is employed where in this source the target material is heated until the material is at the gas phase. The evaporated atoms then interact with inflowing inert gas at both low pressure and temperature. This causes supersaturation of the gas vapour leading to the formation of clusters as described in the eq. (2.1) and eq. (2.2). The growth of clusters continues in the condensation chamber until they are forced through a nozzle into the low pressure region [20]. More details on the cluster apparatus' used for this thesis can be found in chapter 3.

2.1.2 Cluster-surface Interaction

In order to apply clusters for various practical applications, these clusters need to be deposited on the surfaces of interest or similarly can be embedded into materials so as to modify said surfaces/materials and utilize their specific properties. Interaction of a beam of clusters with a surfaces falls into three different regimes depending on the collision energy; soft landing, pinning and energetic collisions. Illustration of two of these energy regimes is given in fig. 2.1 [20, 23].

In the aforementioned cluster apparatuses, the soft landing which is the low energy deposition regime is utilized. In this regime, the kinetic energy per cluster atom (or molecule)

is lower than the binding energy of the cluster components and does not lead to cluster fragmentation upon impact of clusters with the surface. Soft landing is therefore used when the composition of the clusters is to be preserved, however the structure of the clusters may be distorted. This distortion is linked to the physiorption and formation of Van Der Waals (VDW) bonds with surface atoms, as represented in fig. 2.1(a). Despite the various applications of this regime, the issue with clusters produced is their high diffusive mobility that causes large clusters to aggregate into islands or smaller clusters to coalesce into larger particles [23].
As mentioned previously, particles on the surface interact and as a result can either coalesce leading to the merging of two or more clusters which is the case for smaller clusters. On the other hand larger clusters can form aggregates and result in islands on the surface [23]. If however the clusters neither agglomerate nor coalesce then the morphology is a random paving of clusters as reported in the works of [24]. In the case that there is significant diffusion but no coalescence, then clusters form the morphology consistent with large branching islands that have been represented and explained by the numerical deposition diffusion aggregation model (diffusion limited aggregation model) [23, 25].

On the other hand, when the kinetic energy per atom is higher than the cohesive energy then the impact is considered to be of high energy and is termed implantation as seen in fig. 2.1(b). Deformation of the clusters will occur when the kinetic energy of the clusters is above the cohesive energy where clusters will then either flatten or spread across the surface. However if the kinetic energy is sufficient enough and larger than the implantation energy the clusters will as a result undergo implantation thereby entering the surface [20, 25].

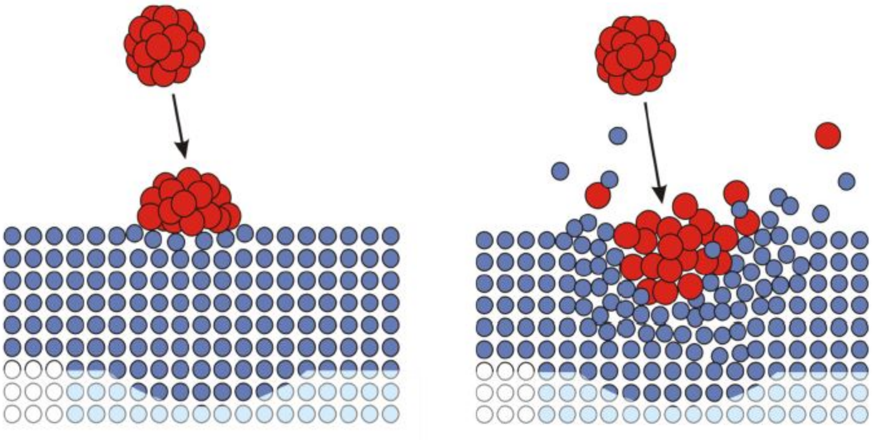

(a) Cluster Deposition (b) Cluster Implantation

FIGURE 2.1: Representation of cluster deposition or implantation depending on the energy regime ; soft landing (a) and hard landing (b) [23]

2.2 Polymer composites with metal nanoparticles

Noble metal NPs have gained interest in the research and industrial sectors due to their optical, catalytic as well as electronic properties. In addition when these noble NPs are embedded into a polymer matrix for instance, the aforementioned properties are enhanced even further due to quantum size effects [26–28]. Nanocomposite materials that are comprised of these metal NPs in their matrix display promising technological applications due to the collective property of their constituents [29–31] and exhibit unique optical properties arising from their Localized Surface Plasmon Resonance (LSPR). This is the case as these NPs in a dielectric matrix, in this case polymers, display interesting absorption as a result of the coherent oscillation of conduction band electrons following excitation by electromagnetic radiation. The study of said polymer films containing embedded metal nanoparticles has attracted great interest, with various applications due to their distinctive mechanical, electrical and optical properties. Metal NPs on the surface/embedded in the polymer have also been shown to posses antimicrobial properties which can be tuned by adjusting both the size and shape of the nanoparticles [15, 32]. In order to produce polymers with NPs on polymer surfaces various methods can be employed such as; evaporation, thermal decomposition of organometallic precursors to sputtering of NPs followed by thermal annealing.

In addition there exists various surface modifications that are aimed to introduce surface assisted antibacterial properties. Polymers as well as polymer coatings are a possible route when interest is in controlling the release of organic molecules, drugs or inorganic antimicrobial compounds [33].Covalent immobilization of antibiotic molecules is an alternative approach that also hinders bacterial adhesion [34]. Lastly as will be the focus of this report, a different approach, based on either inorganic or hybrid organic-inorganic coatings, which promise the possibility to release antimicrobial compounds as well as intrinsic antibacterial activity [35]. These different approaches can be seen in fig. 2.2 below.

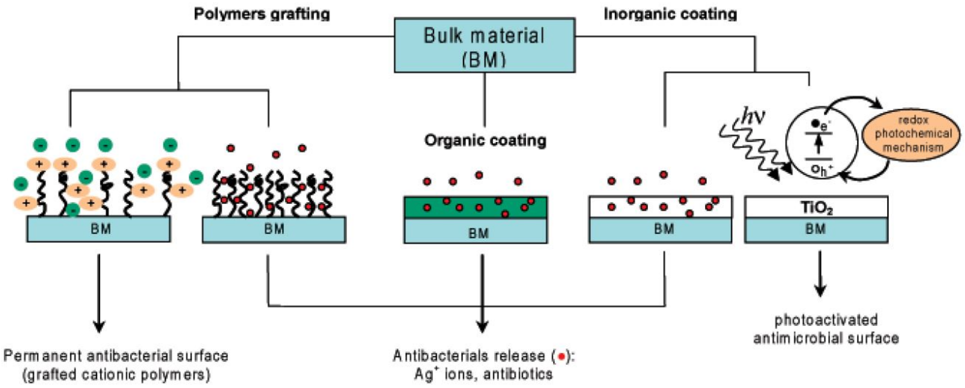

FIGURE 2.2: Surface modification approaches that provide for the release of antibacterial agents. Such modified surfaces can be implemented in coating medical devices. [35]

2.2.1 Optical Properties of Nanoparticles

As a material gradually reduces in size, the percentage of surface atoms on the other hand increases when compared to their bulk counterparts. In the case for metals as they approach the nanoscale, the surface-to-volume ratio of the material becomes significantly large affecting their electronic energy states and give rise to unique optical, chemical and electrical properties which deviate from the bulk material [36]. These various properties can be observed as quantum coinfinment in semi-conductor particles, surface plasmon resonance in nobel metal particles and super paramagnetism in magnetic materials [37].

Upon interaction of electromagnetic waves with metals, the electric field gives rise to a coherent oscillation of the conduction electrons as seen in fig. 2.3 , this phenomena is known as Surface Plasmon Resonance (SPR) which as mentioned earlier is unique to nobel metal

NPs [38]. This oscillation is the result of the displacement of the electron cloud relative to the nucleus, with the oscillation frequency dependent on the electron density as well as the geometry of the charge distribution [39]. The displacement $\vec{D}(\vec{r},\omega)$ caused by the oscillation can be written in terms of the electric field $\vec{E}(\vec{r},\omega)$, the vacuum permittivity constant, ϵ_0, and the dielectric function of the metal, $\epsilon_{metal}(\omega)$ [38],as:

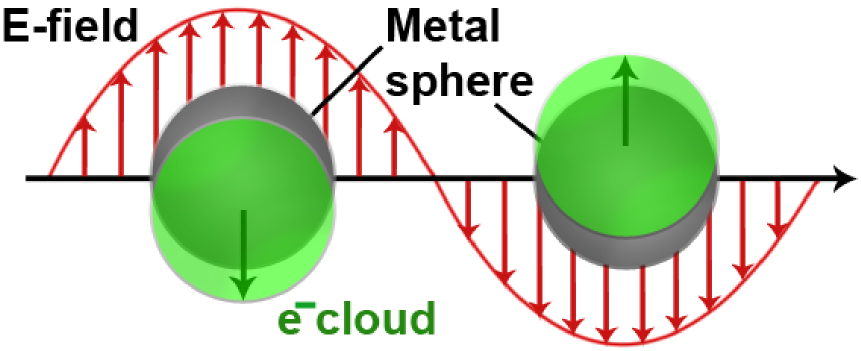

Figure 2.3: Schematic description of electron cloud displacement under the influence of an electromagnetic wave [39]

$$\vec{D}(\vec{r},\omega) = \epsilon_0\epsilon_{metal}(\omega)\vec{E}(\vec{r},\omega) \tag{2.3}$$

where $\epsilon_{metal}(\omega)$ is complex given as:

$$\epsilon_{metal}(\omega) = \epsilon_1(\omega) + i\epsilon_2(\omega) \tag{2.4}$$

where $\epsilon_{metal}(\omega)$ is dominated by its real part [38].

For NPs with radii much smaller than the incident wavelength, the charge oscillation differs from regular SPR under the assumption that the electron cloud of the particle experiences the same electric field [38]. Due to the oscillation, surface charges are introduced, making the surface charge positive where the electron cloud is absent and negative where the electron cloud is present [40]. This results in a restoring force due to the Coulomb attraction between electrons and nuclei which is partially damped due to heat formation and light scattering. This phenomenon can be described as a dipolar oscillator with a resonance frequency $\omega_{plasmon}$, often denoted as LSPR [38]. SPR appears as a sharp absorption at the resonance frequency $\omega_{plasmon}$. Furthermore LSPR is highly dependent on the surrounding environment which causes the SPR peak to shift.

Mie theory can be applied In order to relate the particle size and the environment to the intensity of light scattered or absorbed. When light interacts with metal nanoparticles the light is absorbed (given as the absorption cross-section σ_{abs}) and scattered (given as scattering cross-section σ_{sca}) [38]. This in turn causes the light passing through the particles to undergo extinction (given by extinction cross-section σ_{ext}) and is linked through:

$$\sigma_{abs} = \sigma_{ext} - \sigma_{sca} \tag{2.5}$$

By introducing the polarizability of the sphere as, α, with ($\epsilon_{particle}$) having same form as eq. (2.4)

$$\alpha = 3V\epsilon_0 \frac{\epsilon_{particle} - \epsilon_{medium}}{\epsilon_{particle} + 2\epsilon_{medium}} \tag{2.6}$$

Where V, is the volume of a sphere ($V = \frac{4}{3}\pi R^3$) and using the extinction coefficient given below as;

$$\sigma_{ext} = 3\frac{2\pi}{\lambda}\sqrt{\epsilon_{medium}} Im(\alpha) \tag{2.7}$$

Rewriting eq. (2.7) using $V = \frac{4\pi}{3}R^3$ and assuming negligible scattering for very small particles, this reduces eq. (2.5) to $\sigma_{abs} \approx \sigma_{ext}$, giving

$$\sigma_{abs} \approx \sigma_{ext} = 9V\frac{2\pi}{\lambda}\epsilon_{medium}^{3/2}\frac{Im(\epsilon_{particle})}{|\epsilon_{particle} + 2\epsilon_{medium}|^2} \tag{2.8}$$

It is hence possible to obtain an approximate form of the extinction cross section of a NP using Mie theory under the assumption that the particle is much smaller than the incident wavelength. This in turn implies that the absorption is the major contributing factor to the extinction. This condition results in the occurrence of a LSPR peak whose position and intensity depend on the dielectric environment (and hence the refractive index) of the medium ($\epsilon_{medium} = n_{medium}^2$) [41].

2.2.2 Stabilization of Nanoparticles by Polymers

Stabilization of NPs is necessary due to NPs being sensitive to impurities that arise during their synthesis which can bind to the NPs. These processes are often undesirable and irreversible but can be circumvented by stabilization with high molecular compounds such as polymers [16].

Nanoparticle solutions are representative of a typical colloidal system comprised of a continuous phase and a dispersed phase. Herein the continuous phase is the dispersed medium, which is the solvent and the dispersed phase being the nanoparticles. Such a system is said to be stable only when its dispersed phase can exist as separate individual particles for a prolonged period of time.[16].
Colloidal solutions are governed by two forms of stability; kinetic and aggregation stability. The kinetic stability denotes the stability of the system relative to gravity forces. Here crucial factors determining the stability of colloids include dispersion forces and viscosity of the medium. For such a system, the stability decreases with increase in particle size. The other form of stability is aggregation stability. This type of stability is concerned with the system's ability to preserve the degree of particle dispersity. Here NPs create large aggregates that can adsorb ions on their surface from the solution thereby forming an adsorbtion layer [16].

The adsorption layer consists of potential determining ions and counter- ions. In addition aggregation stability of these systems can be described by the formation of solvate shells of dispersed medium molecules around colloidal particles which prevent particles from aggregating. These solvate shells act as wedges and hinder particles to aggregate as the particles cannot come into contact with each other [16]. Hence for this work, the polymer PS has been used as a dispersive medium to stabilize the nanoparticles as well as present a surface to which they can adhere to.

The use of polymers in developing nanocomposities does not only provide a supporting function by stabilizing nanoparticles. The use of polymers in developing nanocomposites also enhances the antimicrobial performance of such a system that due to three main phenomena: 1; the synergy between the polymer and metal nanoparticle which increases the antibacterial capacity of the composite as compared to that of separate components; 2,

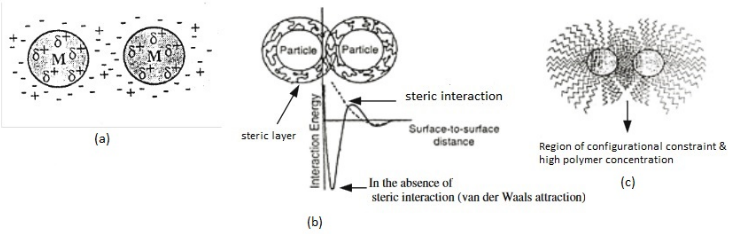

FIGURE 2.4: Nanoparticle stabilization by polymer either due to (a) electrostatic stabilization, (b) steric stabilization or (c) high polymer concentration [16]

The long term release of ions, therefore prolonging the bactericidal effect of the nanocomposite and 3, the increase in surface area that is associated with the fine dispersion of the metal nanoparticles in the polymer matrix [42, 43]. The release of ions for elemental metal particles requires the presence of water and oxygen. It is therefore crucial to retain these within the polymer. Other properties of the material such as crystallinity and matrix polarity can influence the rate of ion release as these properties constitute the diffusion barrier to water molecules and ions during their propagation[43]. In addition ion release increases with the polarity of the polymer, where the polar nature of the polymer facilitates the diffusion of water molecules[43]

In order to understand the embedding of these metal NPs one is to consider the chemistry/physics of the interface as described by *Kovacs et al.* where nanoparticles on the surface are considered to be thermodynamically unstable. These Nanoparticles can then either by wetting or embedding mechanism undergo transition into the surface of interest [44]. When considering the surface energies, NPs with surface energies less than the substrate undergo wetting whilst when NPs have surface energies larger than the substrate, they can become embedded into the material. The process of NP immersion into the surface is driven by surface free Gibbs energy, which for metal NPs decreases when immersed into a polymer. This thermodynamic driving force originates as a result of the system reducing its surface energy which in turn allows for the immersion of the NPs [45, 46].

This thermodynamic behavior, leading to the the embedding of NPs was postulated by *Kovacs et al.*, [45] and is given in equation eq. (2.13). At first when considering a metal NP of surface area σ on the polymer surface, the surface free energy of the NP is then given as:

$$G_s = \sigma\gamma_{np} \tag{2.9}$$

Here, γ_{np}, denotes the surface energy of the nanoparticle. In the case when the NP is considered to be embedded into the surface, the surface energy is then substituted with the interfacial energy of the NP and the surrounding polymer. Hence the difference between the surface energies of the particle when it is on the surface and when inside the polymer represents the net change in the free energy of the system and is given by eq. (2.10) [45, 46]:

$$\Delta G_s = \sigma(\gamma_{np/polymer} - \gamma_{np}) \tag{2.10}$$

Here $\gamma_{np/polymer}$ represents the interfacial energy between the polymer and NP. Furthermore the net change in the free energy, ΔG_s, can be derived by measuring the work done whilst travelling from the surface to inside of the polymer. In this case when a particle of surface area σ is being embedded in the polymer with a surface energy of $\gamma_{polymer}$, this results in a void with a free energy of $\sigma\gamma_{polymer}$ and upon filling this void with a NP then an energy corresponding to σW is regained (here ,W, is the work of adhesion between the particle and the polymer). Consequently in this case the net change in the free energy of the system, ΔG_s, would be given as: [45, 46]

$$\Delta G_s = \sigma(\gamma_{polymer} - W) \tag{2.11}$$

Furthermore when taking eqs. (2.10) and (2.11) into account the work of adhesion between the particle and the polymer becomes;

$$W = \gamma_{np} + \gamma_{polymer} - \gamma_{np/polymer} \tag{2.12}$$

where *Kovacs et al.* then determined that embedding is favorable when $\Delta G_s < 0$ and in conclusion that complete embedding is possible when:

$$\gamma_{np} > \gamma_{np/polymer} + \gamma_{polymer} \tag{2.13}$$

Kovacs et al. also considered from a kinetic point of view, that metal NPs situated on the surface of the polymer can undergo wetting or dewetting and become embedded into the polymer as a result of annealing above the glass transition temperature [45, 46].

2.2.3 Spin Coating of Polymer Films

The earliest report of spin coating can be traced back to the works of *Alfred Emslie et al.* [47] where the spreading of a thin axisymmetric film of Newtonian fluid onto a planar substrate rotating with constant angular velocity was investigated. As a result, spin coating nowadays is considered a leading technique in producing uniform thin films. Films produced with this technique are in the range of micrometers to nanometers and is applied in various fields such as in the manufacture of integrated circuits, optical mirrors and even color television screens. The viscous force and surface tension causes a thin residual film to be retained on the flat substrate and centrifugal forces drive the rest of the liquid radially outwards. The film produced is thus due to the interplay of outward fluid flow as well as evaporation [48, 49]. In many instances, such as for this report, the coating material is polymeric and is applied in the form of a solution from which the solvent evaporates [48].

Spin coating procedure can be broken down into four stages which are deposition, spin up, spin off and finally evaporation of solvents. Amongst the various stages, spin off and solvent evaporation are considered to have the biggest impact on final coating thickness [48]. Deposition, fig. 2.5(a), is the stage of delivering an excess of the solution to be coated unto the surface of the substrate, where a portion of the substrate is wetted. During deposition, the solution is placed on a substrate that is mounted on a rotating stage and accelerated to the desired speed. Spreading of the solution takes place on account of centrifugal forces [48].
Spin-up, fig. 2.5(b), is when the substrate is accelerated up to its final rotation speed with fluid expulsion from the wafer surface due to the rotational motion. The initial depth of the solution on the wafer surface causes spiral vortices to be formed. These vortices arise as a result of the twisting of the top of the fluid as the wafer below rotates rapidly. Eventually the as the fluid becomes thin enough it begins to rotate with the wafer. Once the wafer reaches its desired speed the viscous shear drag balances the rotational acceleration [48].
The third stage, spin off/stable fluid flow fig. 2.5(c), is when the substrate spins at a constant rate and fluid viscous forces dominates the fluid thinning behavior. This stage is responsible for the gradual fluid thinning characteristic. Generally the fluid thinning is g uniform; however this is is not the case when considering volatile solutions, where interference colors are usually observed. Edge effects are also observed in this stage as the

fluid flows uniformly outward thereby forming droplets (at the edge) that are flung off. Depending on the surface tension, viscosity and rotation rate, there may be a difference in coating thickness at the edge of the coated substrate [48].
The final stage is evaporation fig. 2.5(d). At this stage the substrate is spinning at a constant rate and solvent evaporation dominates the coating thinning behavior. At this point the film begins to dry. Furthermore the shrinkage of the film layer is due to solvent loss resulting in the formation of a thin film [48].

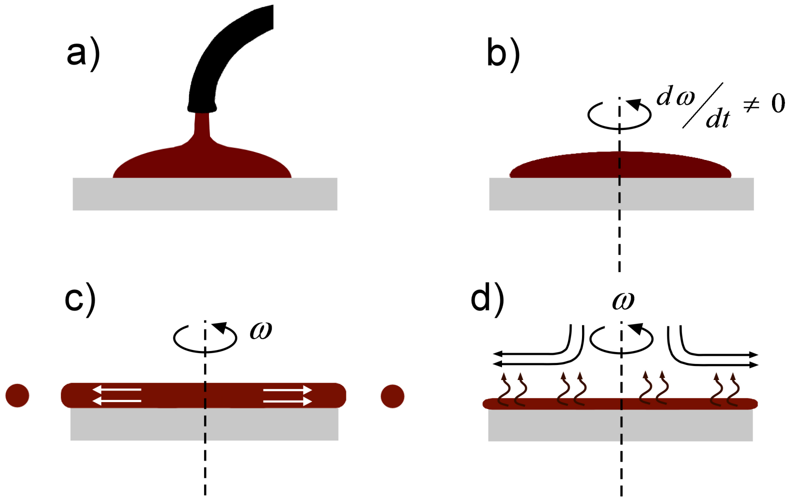

FIGURE 2.5: Spin coating procedure depicted as four stages; (a) deposition, (b) spin-up, (c) spin-off and (d) evaporation [50]

The film forming process is driven by several parameter such as the angular velocity, solution viscosity and the dispense volume that are related to the thickness obtained. Here the major parameters being the the fluid viscosity and the rotating angular frequency. Whereas the dispense volume should be sufficient in order to wet the entire surface [48]. These parameters can be altered as desired in order to control film thickness. In addition to controlling the thicknesses, it is also fundamental to control the surface smoothness and uniformity of the film. As a general consensus the thinner the film, the more uniform the layer [51] however for thicker films surface roughness can be reduced by heating above the glass transition temperature of the polymer [52].

When taking into account the solvent and polymer used, the film thickness can be controlled by the polymer concentration and hence the viscosity, as well as the spinning speed and the rate of solvent evaporation.

2.3 Bacterial structure and growth

The term microorganism is used to categorize several species such as archaea, some fungi, algae, as well as bacteria, which can be further subdivided as either being eukaryotic or prokaryotic depending on the structure of the cell. Prokaryotes are further subdivided into the domains of Bacteria and Archaea, whilst eukaryotes belong in the domain of Eukarya [53].

Prokaryotic cells consist of several intracellular components which are not bound to the membrane bound, this can be seen in fig. 2.6, showing the structure and components of a rod-like bacteria (*E.coli*). A general characteristic of prokaryotes is the lack of a cellular nucleus. Their genome is in the form of a single strand of Deoxyribonucleic acid (DNA) (circular DNA). Some bacteria also contain DNA plasmids which can be transferred to other bacteria and often provide drug resistance as well as the ability to produce toxins [53].

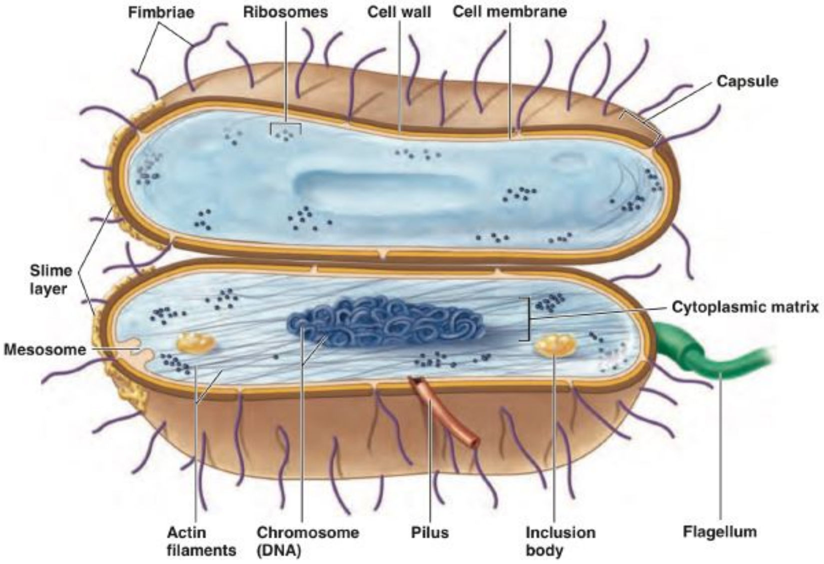

Figure 2.6: The structure of a rodlike bacterial cell that shows the composition of the cell. Not all components are present in all bacterial cells [53].

The cell envelope that encloses the prokaryotic can contain flagella and axial filaments that provide for the bacterial cell mobility. In addition there exists external components attached to the cell envelope known as pilus and fimbriae. These external components are responsible for the interaction with the surrounding medium. Furthermore the cell envelope is also comprised of two primary layers, the cell wall and cell membrane. These layers are separated slightly by the periplasmic space, which is a vital reaction site for substances during transport in and out of the cell [53]. The cell wall accounts for the shape of the bacterium providing structural integrity and keeps the bacterium from collapsing or bursting due to deviations in osmotic pressure. This stability in turn depends on the macromolecule Peptidoglycan (PG) which is composed of a repeating framework of extensive glycan chains; N-acetyl muramic acid and N-acetyl glucosamine crosslinked by short peptide fragments [53]. The cell wall is fundamental to bacterial survival and without it the bacterium will be prone to lysis. Beneath the cell wall, the cell membrane can be found which is a thin flexible bilayer mainly composed of phospholipids. This bilayer is embedded with nitrate and sulfate rich proteins. Some of these membrane proteins are found on the surface of the membrane and others spun through the entire membrane, known as peripheral and integral membrane proteins respectively [53]. Bacterial cell membranes typically consist of 30-40 % phospholipids and $60 - 70$ % proteins from the total membrane mass. However there are some prokaryotes which differ from this model such as the membranes of mycoplasma and archaea [53].

The cell envelope can include one or two cytoplasmic lipid membranes that classify the bacterium as either being Gram-negative or Gram-positive bacteria. The Gram-positive bacteria envelope, depicted in fig. 2.7, consists of a thick PG cell wall that ranges from 20 to 80 nm in thickness as well as a cell membrane. Additionally the Gram-positive bacteria cell wall is also composed of closely bound acidic polysaccharides (including teichoic acid) embedded in the framework of the peptidoglycan layer and lipoteichic acid which is attached to lipids in the cell membrane. Typically Gram-positive bacteria have a very thin periplasmic layer or none at all [53].

In comparison Gram-negative bacteria, as seen in fig. 2.7, consists of a thinner layer, 1-3 nm , of PG and unlike Gram-positive bacteria , consist of an outer membrane. This outer membrane is similar to the cell membrane but also contains specialized types of lipopolysaccharides and lipoproteins. These lipid molecules constitute the top layer matrix of the membrane where porin proteins are located. These porins act as transport proteins and regulate the transport of molecules in and out of the cell. The porin proteins therefore define the selective permeability of the membrane for these bacteria. More importantly the thin PG layer means that Gram-negative bacteria are more flexible but in turn more susceptible to lysis [53]. On the other hand due to the additional membrane layer, the Gram-negative bacterium is less prone to (some) antimicrobial chemicals and thus makes infections caused by them intractable.

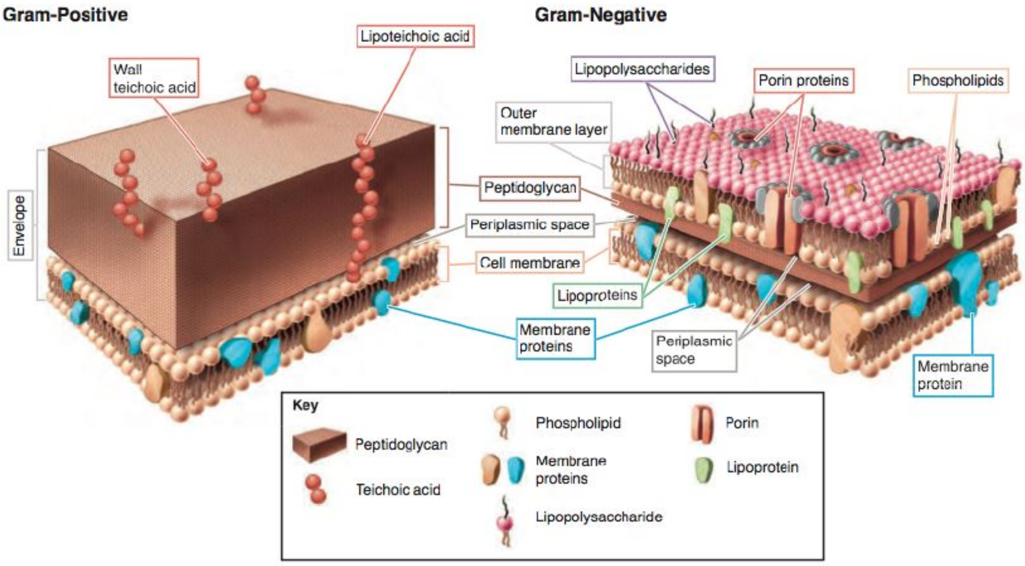

FIGURE 2.7: An illustration of the Gram-positive and Gram-negative cell envelope. Here it is evident that in the case of the Gram-positive bacteria the nature, i.e. thickness, of the PG layer in comparison to the Gram-negative cell envelope [53].

As previously mentioned, *E.coli* will be the main focus when testing the antibacterial properties of the prepared polymer metal nanocomposites. *E.coli* is a Gram-negative, rod-like facultative anaerobe bacterium which ferments lactose but prefers aerobic respiration given that oxygen is present. The *(E. coli)* chromosome contains 4288 genes measuring about 1 mm when unfolded, in comparison to the dimensions of the bacterium itself which is 1 µm in length [53]. A common habitat of *(E. coli)* is the digestive tract of most warm-blooded animals. *E.coli* lives in symbiosis with the host in the digestive tract, producing vitamins and acids that are beneficial to the host, as well as proteins toxic to intestinal pathogens. Nonetheless when *(E. coli)* exists in large concentrations it can become pathogenic and hence hazardous to the host leading to food and water poisoning often resulting in diarrhea [54]. Furthermore 80% of UTI cases can be traced to *(E. coli)* [54], which makes *E. coli* an ideal candidate as a target microorganism.

Microorganisms subjected to metals in their environment have to coupé and in most instances procure a strategy to withstand metal toxicity. Several mechanisms have been investigated and although complex and diverse, these resistance and adaptation mechanisms can be categorized functionally fig. 2.8 [55].

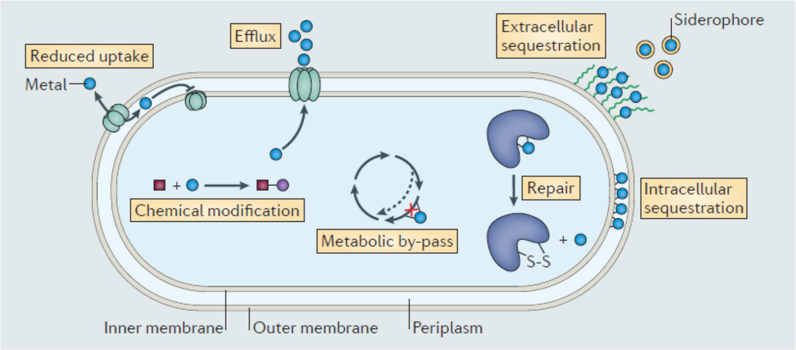

FIGURE 2.8: The various proposed mechanism that microorganism adapt inorder to deal with various deadly metals [55].

The different mechanisms as depicted in fig. 2.8 include Chemical modification, Efflux, Extracellular sequestration, intracellular sequestration, metabolic by pass, reduced uptake and lastly repair.

In chemical modification, toxic metals have undergone specific redox and covalent reactions which alter their chemical reactivity converting toxic metal species to less toxic forms. Such chemical modifications apart from altering the redox state of the metal can also generate organometallic (small) molecule compounds or metal crystal precipitates[55].

For Efflux, resistance to toxicity is determined by genetic markers that encode for a range of membrane transporters responsible for the transport of toxic metals outside the cell. Expression of these systems is driven by regulators which bind to the metals, whereby activity of these transporters is regulated either by ATP hydrolysis or chemiosmotic potential[55].

Other microorganisms, through extracellular sequestration, are capable of up-regulating expression of extracellular polymers or siderophores as a response to metal exposure. These molecules contain functional groups that can coordinate metal ions which can trap or precipitate metal ions in the extracellular environment . Furthermore soluble siderophores bound to toxic metals via membrane transporters are subjected to reduced uptake or even increased efflux. Metals are also capable of binding to (or precipitating at) the bacterial cell wall through reactions with lipopolysaccharides [55]..

Microorganisms are also capable of precipitating metals as metal oxides, -sulphides, -protein aggregates or elemental metal crystals that become associated with the cytoplasmic membrane. These toxic metals thus become isolated in the cytoplasm or periplasmic space. Cytoplasmic proteins can then be used to isolate, bind or store these metals [55].
Microorganisms can also by-pass metabolic pathways that contain metal disrupted enzymes and circumventing toxic metal ligands. This is done by producing alternative proteins with catalytic cores which do not bind to the toxic metal ligands as well as diverting metabolites towards alternative pathways [55].
Cellular chaperones, enzymes or antioxidants can also be used to repair molecules that contain redox sensitive functional groups. These functional groups tend to be disrupted due to oxidation by primary reactions with metals or catalytic by-products of metals, for instance Reactive Oxygen Species (ROS) [55].
Lastly in order to control the uptake of toxic metals microorganisms have evolved a strict regulatory mechanism used to control the activity of membrane transporters and therefore reduce the uptake of toxic metals. Such regulation, expression and activity of proteins involved in membrane transporters is vital for metal resistance and adaptation to toxic metals [55].

2.3.1 Microorganisms Population Growth Dynamics

The growth of microorganisms can be studied by modelling the increase in popopulation size through a mathematical description. Consider a single cell of a bacteria in a medium with optimal conditions, then the bacteria will divide (double) according to a specific generation time(doubling time, t_g) given by the equation eq. (2.14) .

$$n = \frac{t}{t_g} \tag{2.14}$$

Considering bacterial growth that begun with one cell, this can be described by the equation eq. (2.18), where in the beginning there has been no division (n= 0) and hence the number of cells (N) = 2.

$$N = 2^n$$

(2.15)

Accordingly the number of cells after a certain number of divisions, taking into account the initial number of cells (N_0), is then expressed as

$$N = N_0 * 2^{\frac{t}{t_g}} \tag{2.16}$$

The expression can be described exponentially with the basis e (Eulers number) (where 2 = (e^{ln2})) and the above expression, eq. (2.18), becomes;

$$N = N_0 * (e^{ln2})^{\frac{t}{t_g}}$$

(2.17)

and simplifies to;

$$N = N_0 * (e^{\mu * t}) \tag{2.18}$$

Where μ is the specific growth rate. This constant is unambiguous for every bacterial species growing under optimum conditions. However these conditions cannot be maintained indefinitely. For instance in a batch culture, the bacteria are able to reproduce until all nutrients are consumed or to the point where the environment is not filled with toxins. In the case of such a system, bacteria growth is described according to four phases of development; Lag phase, Exponential phase, stationary phase and Death phase [6, 56].

Lag phase; during this initial phase after inoculation of the culture into fresh medium, there is no growth. Despite the lack of apparent cell division the cells grow in mass, synthesize enzymes, proteins and the metabolic activity increases. The length of this phase

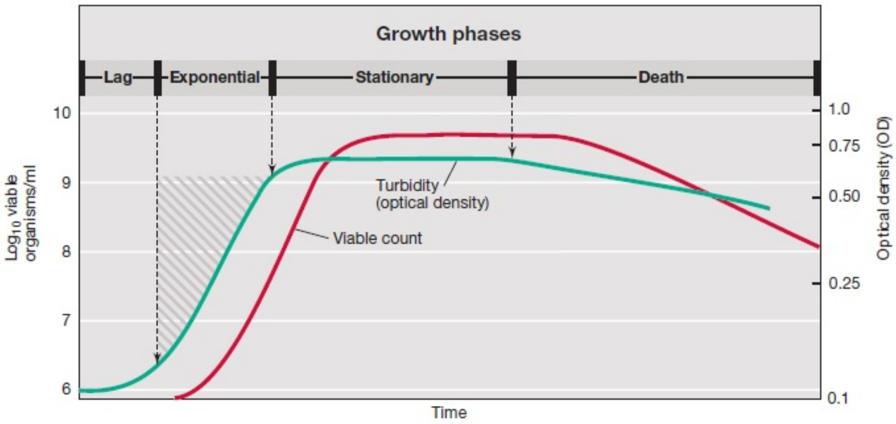

FIGURE 2.9: Illustration of the growth phases for bacteria in a batch culture. The viable count measures the number of cells capable of reproducing. The turbidity measures the light scattered from the liquid medium [6].

depends on the various factors such as the size of the inoculum, the time necessary for damage recovery and the time required to synthesize new metabolic enzymes.

The exponential phase is characterized by a balance of growth where at this stage the cells are dividing regularly by binary fission. The cells divide at an exponential rate depending on the composition of the growth medium and conditions of the incubation. The growth at this stage is characterized by the generation time and the doubling time of the bacterial species as described above eq. (2.18).

The stationary phase occurs as exponential growth cannot be sustained in a batch culture. At this stage the population growth is limited by the consumption of available nutrients in the medium and the accumulation of end products or inhibitory metabolites. During this phase it is hard to determine whether some cells are dying and an equal number are still dividing.

The Death phase occurs when incubation continues beyond the stationary phase. At this stage the number of viable cells in the population decline. This condition occurs as a result of the total depletion of nutrients in the growth medium/environment [6, 56].

2.3.1.1 Enumerating bacterial cell growth

In microbiology studies there are certain occasions where it is essential for one to be able to estimate the number of bacterial cells in a broth culture or liquid medium. The determination of the number of cells can be carried out either directly or indirectly. These methods include turbidimetric measurements, standard plate count, cell mass determination, direct microscopic counts and the measurement of cellular activity[6]. The methods presented for this thesis include turbidimetric measurments as well as standard plate counting in order to estimate the effects of the polymer nanocomposites prepared.

In viable cell counting, a cell is termed viable if it is able to divide and form a population (or colony). The number of cells that are capable of forming colonies, once plated, are usually determined by using a suitable agar medium. One assumes that in the viable counting procedure each viable cell can grow and further divide to yield a colony, in this the colony numbers are therefore proportional to the cell numbers [6].

Two commonly used approaches in performing a plate count include the spread plate method and the pour plate method. For the spread plate method a volume of 100 mL or less of a diluted culture solution is spread evenly on the surface of an agar plate. This is done by using a sterile glass spreader or a Dragulska spatula. Following this the plate is then incubated at the appropriate temperature to allow for colonies to grow before counting the colonies formed. It is important that the surface of the plate is not moist in order to allow culture solution soaks in so as to ensure the cells remain stationary. In addition using volumes in excess of 0.1 ml would mean that the excess liquid would not soak in thereby causing the colonies to overlap(coalesce) as they form. This proves to be an issue when counting the number of colonies formed[6].

Whereas in the pour plate method a volume of 0.1 mL to 1 mL of the liquid culture is pipeted into a sterile petri dish and melted agar medium is then added. The liquid culture solution and agar medium are then mixed by swirling the plate. As the sample is mixed with the molten agar medium a larger volume of sample can therefore be used than the former method. It is important that the microorganisms to be counted must be able to withstand the temperature of the molten agar. In this method colonies form throughout the plate and not just on the agar surface. These methods can be seen in the fig. fig. 2.10 below.

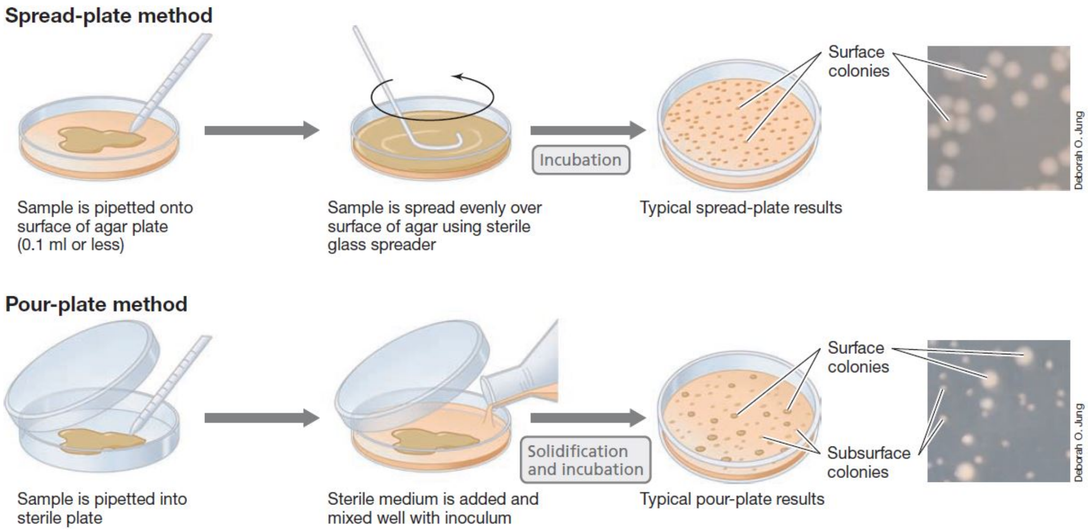

FIGURE 2.10: methods applied in order to estimate number of CFU [6].

In both methods described above, the number of colonies developing on the plate must not exceed or fall below a certain threshold. In certain cases when there are crowded plates, some cells do not form colonies or some colonies tend to fuse which in turn leads to incorrect measurements. Hence the need to dilute cell suspensions before plating in order to obtain a statistical valid count. Plates with colonies in the range 30 – 300 are considered. When and if the number of colonies are to small, the statistical significance of the calculated colonies will be too low. In any case, to obtain an appropriate colony number the sample to be counted should be diluted which is done by several 10. Fold dilutions of the sample. With dense culture a serial dilution can therefore be used to obtain a suitable dilution for the sample in question fig. 2.11 [6].

The number of colonies observed by use of a viable count experiment depends on many factors including the inoculum size, the viability of the culture as well as the chosen growth medium and incubation conditions. These factors influence on the number of colonies formed. Viable counts may be subject to several errors including pipetting inconsistencies, inhomogeneity of sample and improper mixing [6]. Henceforth to yield accurate counts great care and consistency is necessary during sample preparation and pipetting. Data obtained are expressed as CFU rather than the actual number of viable cells due to a colony forming unit consisting of one or more cells. Contrast to the difficulties in relation to viable counting the procedure yields the best estimation of the number of viable cells in

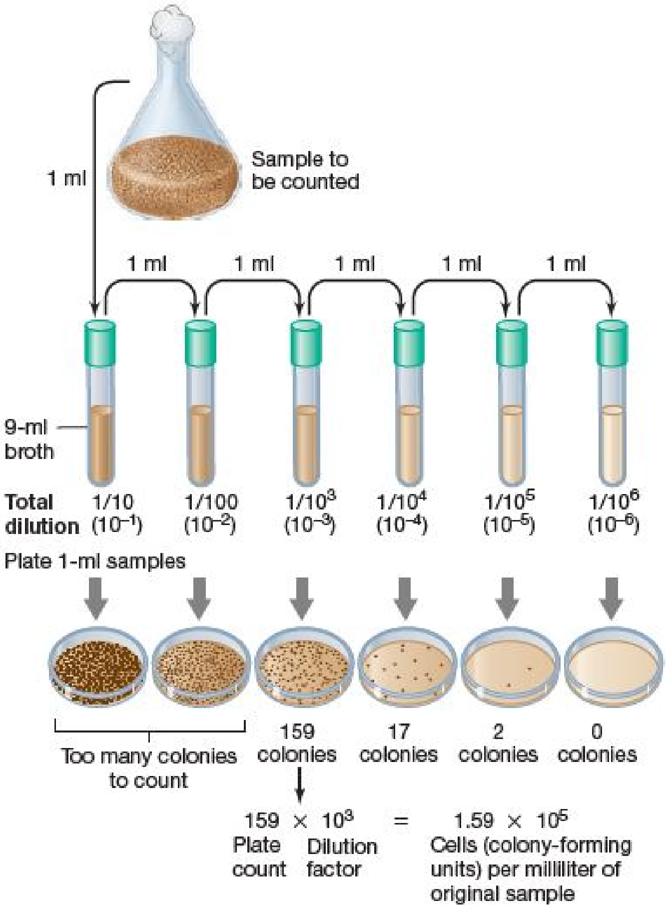

FIGURE 2.11: Viable cell counting using the serial dilution technique and pour plate method [6].

a sample with a high sensitivity. In addition by using highly selective culture media and growth conditions, one is able to target only a particular species or even a single species in a mixed population of microorganisms present in a sample [6].

2.3.2 Bacterial Adhesion and biofilm formation

Bacterial adhesion is a process that is governed by various factors from the associated flow conditions, the presence of serum proteins or antibiotics, the bacterial properties to the material surface characteristics. The adhesion to a material surface can be described by two phases an initial, instantaneous and reversible phase followed by an irreversible time dependent phase [57] Phase one, fig. 2.12,of bacterial adhesion consists of the initial attraction of the cells towards the surface due to the effects of physical forces that include Van der Waals attraction forces, gravitational forces, Brownian motion as well as the effects of surface electrostatic charge and hydrophobic interactions. These physical interactions can then be further subdivided as being long range interactions with distances greater than 50 nm between cells and surfaces or short range interactions with distances being less than 50 nm between cell and surface. These short and long range interactions are important in the initial phase thereby making bacterial adhesion possible [58]. As for the bacterial properties, such as the hydrophobicity and surface charges, and in addition the material surface characteristics including chemical composition, roughness and configuration are also important for bacterial adhesion [57]

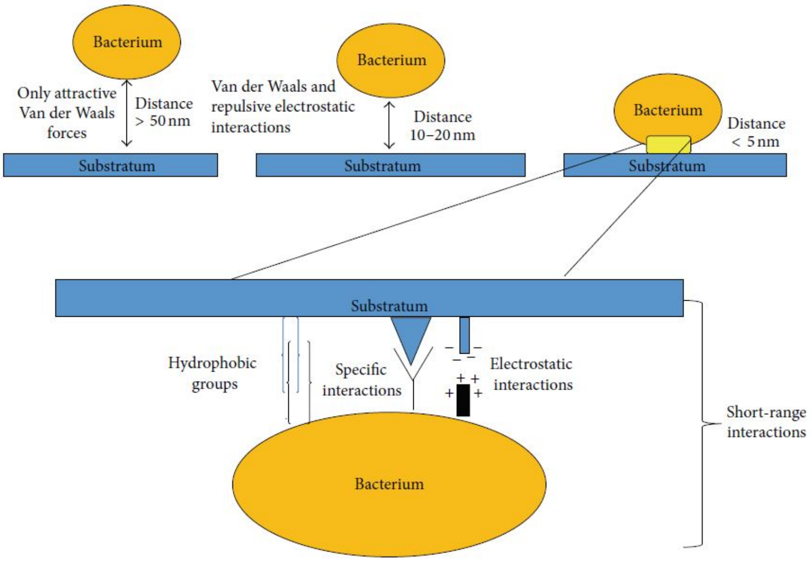

FIGURE 2.12: Physical forces that play a role in the initial attraction of bacterial cells unto surfaces that constitute phase one of bacterial adhesion[58].

Phase two addresses molecular specific reactions between the bacterial surface structure and substratum surfaces that are coated or uncoated with the host matrix proteins. The bacterial surface polymeric structures that include capsules, fimbriae or pili are then responsible for the firm attachment of the bacteria to a surface. Beyond this phase, certain bacterial strains can then form a biofilm if appropriate nutrients are available. The biofilm formation includes various steps where at first planktonic bacteria first attached themselves on a solid surface that may be unmodified or consist of host plasma proteins. This is then followed by cell proliferation, cell-cell interaction and finally the production of an extracellular polymeric matrix where the bacteria accumulate in clusters that eventually form the biofilm as a whole fig. 2.13. Mature biofilms pose a threat as they are resistant to both the action of the innate and adaptive immune system and to the action of antimicrobial agents and disinfections. Furthermore biofilms also contain a large sub population of persister cells which constitute dormant cells capable of surviving antimicrobial treatment [59].

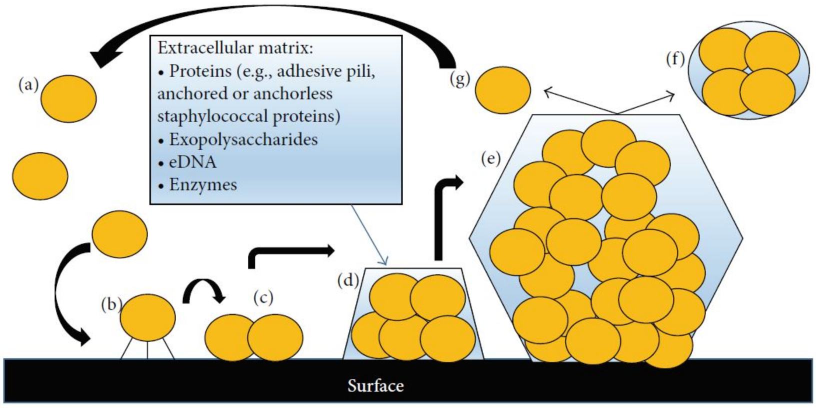

FIGURE 2.13: The various stages of biofilm formation that consist of (a) planktonic cell; (b) reversible attachment to the surface; (c) irreversible attachment; (d) formation of microcolonies; (e) formation of a mature three-dimensional biofilm. Lastly cell detachment from the biofilm: (f) an active process leaving planktonic cell; (g) a passive process that can be shed through mechanical disruption [58].

2.4 Antibacterial Action of Metal and Metal Oxide Nanoparticles

During the years nanotechnology has fashioned a novel route taking advantage of the antimicrobial behaviour of metals and highly active metal nanoparticles have been synthesised. In particular, metal nanoparticles exhibiting biocidal activity can be immobilised or coated onto surfaces with potential applications in several fields including water treatment, medical devices and food processing [60]. A way to enhance the applicability of metal nanoparticles, is their combination with polymers thereby obtaining a composite materials. Metal nanoparticles can for instance be incorporated on the surface of a polymer or embedded into the matrix depending on both the desired application as well as the polymer matrix to be used [43].

Use for NPs has emerged in the field of medicine, where their size dependent physical and chemical properties are being explored extensively. In addition, the sizes of NPs can be adopted to most biological molecules and structures hence this makes them an ideal candidate for the *in vivo* and *in vitro* biomedical research. They are also used in targeted drug delivery systems, imaging and sensing. As mentioned earlier in this report interest lies in their potential antimicrobial application. That is why, in this section we will focus on hypothetical mechanisms which are attributed to some NPs antibacterial properties and the factors that govern this properties.

There are several factors that have been proposed that influence metal NPs antibacterial properties. These include the chemical composition of nanoparticles, the concentration and size of nanoparticles, the shape of nanoparticles, the target species and photo activation which are schematically shown in fig. 2.14 [10].

Composition of the NPs is maybe the most important factor from all. Most of the studies that have been conducted in recent years are concerned with Silver Nanoparticles (Ag NPs) and Gold Nanoparticles (Au NPs). Cu NPs are also subject to research. From the metal oxide most studied are ZnO, Ti_2O, SiO_2, MgO, CuO, etc. The activity of some of these oxide NPs is attributed to the generation of ROS (see section 2.4.1). Effort has been also put in creating combined NPs with enhanced physico-chemical and antibacterial

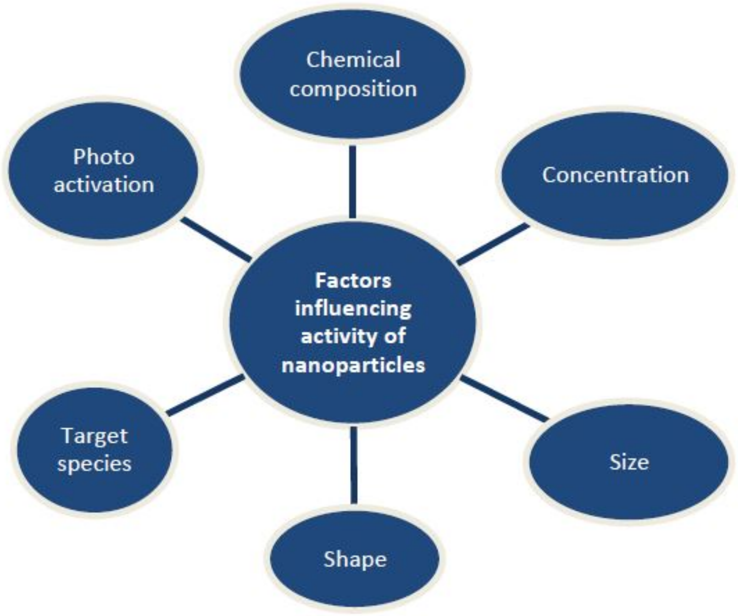

FIGURE 2.14: Schematic description of metal nanoparticles toxicity factors [10]

properties. For example, magnesium and aluminium oxides NPs [61] and TiO_2 NPs doped with silver, carbon and sulfur [17].

In relation to concentration NPs, as expected, show increased antibacterial properties in higher concentrations. Different authors give different values for the Minimum Inhibitory Concentration (MIC) and polarized. For example, for *E.coli* treated with Ag NPs authors are reporting for MIC: [12] - 6.6 $\mathrm{nmol\,L^{-1}}$, [62] - 10 $\mathrm{mg\,mL^{-1}}$, [63] - 60 $\mathrm{mg\,mL^{-1}}$. Similar experiments with Cu NPs are reported. [64] reported the same concentration of 60 $\mathrm{mg\,mL^{-1}}$ for complete inhibition of growth as they did for Ag NPs. [4] give values of 3.0 $\mathrm{\mu g\,mL^{-1}}$ for MIC and 7.5 $\mathrm{\mu g\,mL^{-1}}$ for Mimimum Bactericidal Concentration (MBC). This discrepancies between the authors may be attributed to the different size and structure of the NPs used. It is also known that, in general, smaller NPs means higher antimicrobial activity. This is attributed to the increased SA of the smaller NPs, which allows them to interact more easily with the cells.

The shape-dependent activity is believed to be governed by the percentage of active facets in the NP. Spherical nanoparticles predominantly had 100 facets with only small percentage of 111 facets, rod-shaped nanoparticles (e.g., pentagonal rods) had both 111 facets on side surfaces and 100 facets on the ends, truncated triangular nanoparticles had 111 facets on the top basal planes. High-atom-density facets, such as 111 facets, favour reactivity of silver, and therefore nanoparticles with high number of 111 facets, such as truncated triangular nanoparticles, showed higher antimicrobial activity [10].

In regards to the target species number of studies have shown that for Ag NPs antibacterial action is higher against Gram-negative rather than Gram-positive bacteria. In contrast, ZnO shows increased activity against Gram-positive.This is belived to be a result of the unique interaction between the NPs and microorganism's cell wall, membrane and PGs.

There is also evidence that some NPs (especially those composed of metal oxides - TiO_2, ZnO) show increase activity when photoactivated with Ultraviolet (UV) light. This is believed to be the result of formation of ROS from this photo activated NPs [10]. These NPs are known to be effective against both Gram-positive and Gram-negative bacteria, making them highly efficient as antibacterial agents. Furthermore as a result of the mixed ionic and covalent bonding in metal oxide systems the surface structure has a greater influence for the local surface chemistry when compared to pure metals [65].

The size of nanoparticles can influence whether or not they penetrate bacterial cells by endocytosis or direct diffusion [66]. For nanoparticles which are between 10 and 100 nm typically cross the membrane by endocytosis . This happens in three stages; at first the particles adhere to the membrane after which the membrane wraps around the particle and lastly the lipid-particle complex becomes detached from the membrane. On the other hand for small nanoparticles with diameters of a few nanometers, endocytosis is not an effective way for their uptake due to the low adhesion energy and instead is directly diffused.[66].

2.4.1 Main Hypothetical Mechanisms

There are three main hypothetical mechanism about how NPs are able to inhibit bacterial growth:

- Metal ion absorbtion
- ROS generation
- Accumulation of NPs on bacterial wall and membrane

In solution most of the known NPs are subject to dissolution. This means that we can find increased concentrations of Ag^+, $AgNO_3$, Cu^{2+}, etc. These metal ions are believed to be absorbed inside the cell and can bind to various cell constituents leading to inhibition of the cells function. Depending on the metal property, antibacterial activity can be influenced by two general aspects; the metal reduction potential and the metal donor atom selectivity. Metals are reported to be able to catalyse site-specific damage to cellular proteins via an oxidation process that results in the loss of catalytic activity and triggers an active process of protein degradation [55]. Furthermore, metal ions bind to atoms of donor ligands such as O, N and S through strong and selective interactions [55, 67] wherein external metal ions can replace original metals that were present in biomolecules which in turn causes cellular dysfunction in a process k.a ionic mimicry or molecular mimicry. The terminology depends on whether metal ions or metal complexes are involved. Therefore some metals can promote the destruction of Fe-S clusters whilst other metals can replace non-catalytic metal binding sites and inhibit enzyme activity. [55]

ROS generation is another mechanism believed to be involved in the antibacterial action of NPs. It is especially prominent in some metal oxide NPs (as already mentioned TiO_2 NPs). Consequently an oxidative stress can be induced if these ROS exceed the cell antioxidant capacity and hence lead to the destruction or damage of cellular proteins, lipids and DNA [68]. In addition to the aforementioned effects, increasing levels of ROS triggers the cells programmed death due to pro inflammatory signaling cascades.

Finally, NPs are believed to be accumulated on the bacterial membrane and wall. This lead to increased permeability and disruption in membrane function, which can increase the effect of the other two proposed mechanisms, because more NPs are able to penetrate inside the cell. The peptide portion and the glycan strands of the PG are reported to underwent structural variation and decomposition. This can lead to the creation of "pits" inside the wall.

2.4.1.1 Mechanisms of Action of Copper Nanoparticles

Copper being a redox active transition metal can exist between two redox states the reduced cuprous state (Cu_2O) or oxidized cupric species (CuO)which can dissolve to copper ions [43]. These oxides in the nanoform have been shown to have antimicrobial activity

against both Gram positive and negative bacteria [69–72] .
The antibacterial activity of Cu NPs is linked to a decline in cell membrane integrity as well as the generation of ROS [4]. Cu NPs, thus act on the cell membrane of microorganisms facilitated by the presence of membrane pores in the nanometer size regime. Hence nanoparticles with the appropriate charge and size are able to penetrate the membrane and induce cell death either due to the production of ROS or by the disruption of cellular function which affects the proteins and DNA caused by oxidative stress.
In particular the biocidal action of CuO is mainly due to the direct interaction of Cu ions with the cell components, whereas Cu_2O bacteriostatic action is based on the binding of cu ions with thiol groups thereby causing disruption of cellular function. [4, 69].
Furthermore Cu(II) ions in bacterial cells are reduced to Cu(I) ions by sulfhydryl, which are then responsible for causing oxidative stress by production of ROS that leads to lipid peroxidation, protein damage and DNA degredation [4].
The bactericidal effects of copper-polymer nanocomposites are then based on three phenomena; the release of copper ions, the release of copper nanoparticles from the nanocomposite and biofilm inhibition as shown in fig. 2.15 [73].

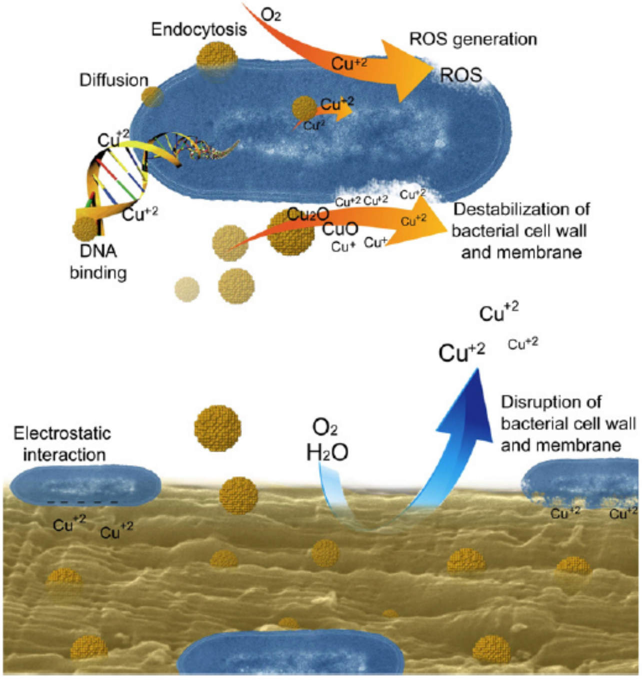

FIGURE 2.15: Illustration of the antibacterial effects of copper-polymer nanocomposites [73].

During the release of ions, the copper ions reach the outer membrane(or cell wall) of the bacteria and either interact with sulfhydryl groups thereby causing denaturation of proteins in the bacterial membrane, or react with Amines and carboxyl groups in N-acetylglucosamine and N-acetylmuramic acid in the peptidoglycan layer. These interactions destabilize and disintegrate the bacterial cell wall and membrane (the bacteriolytic effect). Furthermore the ions released in the bacteria bind to DNA and are cross-linked within and between nucleic acid strands hindering cell replication. Released ions can also generate ROS and cause lipid peroxidation and protein oxidation [73].
On the other hand released copper nanoparticles can adhere to the bacterial surface through electrostatic forces and molecular interaction. These nanoparticles can then penetrate the bacteria either by endocytosis or direct diffusion depending on the size of the nanoparticles. In addition the copper nanoparticles can also release ions and trigger the aforementioned effects of released ions [73]. Copper nanoparticles that move to the surface of the nanocomposite can inhibit biofilm formation as surface nanoparticles significantly reduce the cell surface hydrophobicity hence altering the attachment of bacteria [74]

2.4.1.2 Titanium Oxide Nanoparticles and their antibacterial mechanism

As mentioned earlier this thesis will apart from the antimicrobial effects of nanocomposites containing Cu NPs also focus on the application of TiNP used in polymer nanocompasites.

As Titanium dioxide (TiO_2) is a semiconductor, the adsorption of a photon with sufficient energy causes electrons to move from the valence band ($e_{vb}{}^{-}$) to the conduction band ($e_{cb}{}^{-}$) which in turn results in a positively charged hole in the valence band($h_{vb}{}^{+}$) as seen in fig. 2.16 and represented in eq. (2.19) . Once formed the hole and electron pair($e^{-} - h^{+}$) can then either undergo fast recombination within a time range of pico seconds or charge trapping if suitable e^{-} or h^{+} scavengers are available [35]. For instance, in aqueous environments, electrons react with molecular oxygen whilst the holes on the other hand react with HO^{-} or H_2O thus forming ROS eqs. (2.20) and (2.21). In solution, these products, can react to yield H_2O_2 eq. (2.22),or even further to give hydroxyl eq. (2.23) and hydroperoxyl eq. (2.24) radicals,. In addition further recation of these radicals with organic compounds results in mineralization eq. (2.25) as illustrated in fig. 2.19 [35].

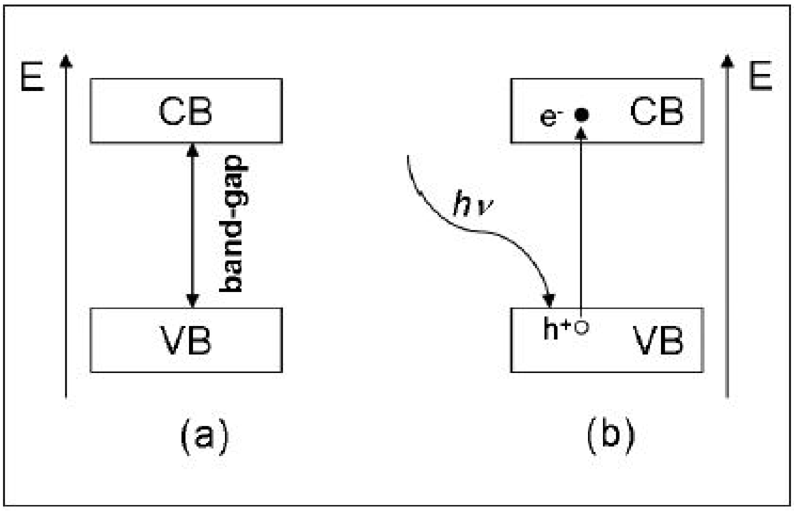

FIGURE 2.16: Illustration of the band energetic structure in (a) and the mechanism of photo-irradiation in a semiconductor(b). [9]

$$Ti0_2 \;\; + hv \rightarrow e_{cb}{}^{-} + h_{vb}{}^{+} \tag{2.19}$$

$$0_2 \quad + {e_{cb}}^- \rightarrow {0_2}^- \cdot \tag{2.20}$$

$$ {h_{vb}}^+ + H_2O \rightarrow \cdot OH + {H^+}_{aq} \tag{2.21}$$

$$\cdot OH + \cdot OH \rightarrow H_2O_2 \tag{2.22}$$

$${O_2}^- + H_2O_2 \rightarrow \cdot OH + OH^- + O_2 \tag{2.23}$$

$$O_2^- \cdot + H^+ \rightarrow \cdot OOH \tag{2.24}$$

$$\cdot OH + organic + O_2 \rightarrow CO_2, H_2O \tag{2.25}$$

When the crystallite diameter of semiconductor particles falls bellow a critical radius, about 10 nm), each charge carrier appears to have quantum similar to a particle in a box. Due to this confinment the band gap is increased and the band edges are shifted yielding in turn larger redox potentials [75].The rate of charge transfer increases for these systems and as a consequence quantized semiconductor particles show higher photoactivity than their bulk counter parts [75].

For efficient photocatalytic activity, a strong electron acceptor is required in order to hinder recombination of ${e_{cb}}^-$ and ${h_{vb}}^+$ [76]. Ti alloys resistance to corrosion and their biocompatibility are maintained by a surface oxide layer that consists mainly of TiO_2. The surface oxide layer is usually found to exsist in the amorphos state. TiO_2 on the other hand can be found as three main polymorphs; brookite anatase and rutile, which all have different band gap energies required to excite an electron from the valence band to the conduction band [9]. The most common studied forms are Anatase and Rutile which have a band gap energy of 3.2 eV and 3.0 eV which correspond to an excitation wavelength of 385 and 410 nm respectively. Furthermore anatse is considered as being more photochemically active due to the higher surface adsorptive capacity and higher rate of charge trapping[9, 35]. Furthermore TiO_2 can be produced through the oxidation of Ti itself [77].

Among the different polymorphs of titania , rutile is the most thermodynamic stable form in the bulk regime and anatase is the most stable when the size regime is below 14 nm [78]. For these forms, the basic structure consists of a titanium atom that is surrounded by six oxygen atoms in an octahedral configuration. Deviations between the different polymorphs is a result of the sharing of the edges and corners of a basic unit ($\mathrm{tiO_6}$) with that of the adjacent one. In anatase, the $\mathrm{TiO_6}$ octahedral units are connected by sharing edges, whereas the rutile phase is built by sharing the corners along the a and b indices as well as sharing the corners along the c direction fig. 2.17. The distortion of the $\mathrm{TiO_6}$ octahedral units in anatase is slightly larger and in addition the Ti-Ti bond distance in anatase is shorter resulting in a more stable form than in rutile. The structural differences in turn results in different electronic band structures.From a themodynamic view point the more rapid the crystallisation of anatase is related to the polymorphs lower surface free energy despite the lower Gibbs free energy for rutile [78, 79]

Of the two forms, anatase has been reported to be more photocatalytically active [80, 81]. The higher activity of anatase is explained by the difference in surface chemistry, where anatase has a higher capacity to adsorb oxygen in the form of $\mathbf{O_2^-}$ and $\mathbf{O^-}$ and also the dissociative adsorption of water molecules as $\mathbf{H^+}$ and $\mathbf{OH^-}$ in comparision to the nondissociative water adsorbtion to rutile faces as $\mathbf{H_2O}$ [82, 83]. In addition as reported by *Ohtani et al.* [84] high photocatalysis activity is achieved when two criteria are fulfilled; a large surface are for absorbing substrate and a high degree of crystallinity in order to reduce the fast recombination of photoexcited e^-/h^+ recombination.

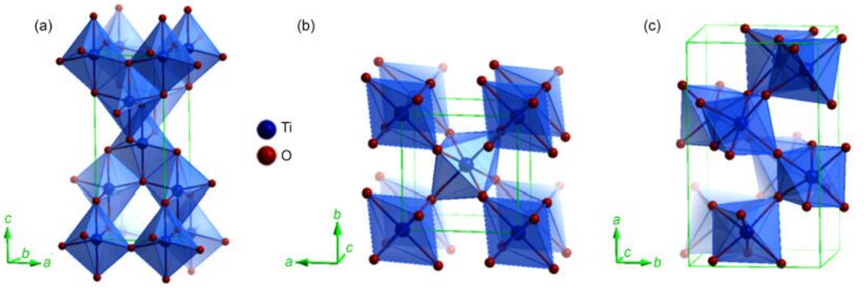

FIGURE 2.17: Representation of the anatase (a), Rutile(b) and Brookite(c) forms of titania.[85]

The photocatalytic properties of TiO2 has been shown to catalyse the oxidation of pollutants by *Fujushima and Honda* [86] in adittion to the ability of killing microorganisms *Matsunaga et al.* [87]. Furthermore photocatalytic surfaces can be superhydrophilic as a result of UV irradiation , whereupon spreading of water occurs (contact angle is reduced) on these surfaces so that dirt can be washed off with applications in self-cleaning windows or glass covers,for highway tunnel lamps [88], in dental implants [89], as well as paint coatings [90] among other various applications.

The main mode of action of TiO_2 NPs is believed to be connected with thier ability to produced ROS upon UV photo activation. As already mentioned these reactive species can interact with many of the biomolecules, leading to oxidation of the cell membrane and disturbing its barrier functions, inactivation of proteins and DNA degradation. It is reported that in *E.coli* TiO_2 NPs in contact with the constituents of the bacterial cell wall (PGs, Phosphatidyl-ethanolamines (PEs) and Lipo-polysaccharides (LPSs)) can lead to there direct degradation [18].

The mechanism of irradiated TiO_2 NPs has been studied for both Gram- positive and Gram negative bacteria. It was originally postulated that the mode of action was the depletion of Coenzyme A (CoA) by dimerization resulting in the inhibition of respiration which was shown by *Matsunaga et al.* [91] on E.coli cells. *Matsunaga et al.* illustrated that there was a decrease in coA in relation to increase in exposure time(irradiation time) and subsequently increase in the dimeric CoA concentration thereby resulting in an inhibition of respiration. In contrast to Matsunaga et al's work, it has been proposed that the main mechanism is due cell wall and membrane damage. This has been shown via Transmission electron microscopy (TEM),Scanning Electron Microscopy (SEM) and Atomic Force Microscopy (AFM) studies, used to show membrane damage and subsequent breakdown of cells upon comparing TiO_2 NPs treated and untreated bacterial cells [35]. Microscopic studies indicated morphological alterations that were indicative of cell wall damage as a result of UVA irradiated TiO_2 NPs surfaces.

Furthermore leakage of intercellular components via detection of lipid peroxidation products has been shown via the release of Malondialdehyde (MDA) by *Hu et al,Kambala et al.*[92, 93] resulting from polyunsaturated fatty acids attacked by ROS such as hydroxyl radicals and H_2O_2. These ROS are produced due to irradiation of TiO_2 surfaces. The activity of TiO_2 on the disruption of the phospholipid bilayers was checked via X-Ray

Diffraction (XRD), laser kinetic spectroscopy and Fourier Transform Infrared Spectroscopy (FTIR). The free radicals ·OH and H_2O_2 are responsible for killing the bacteria which are close to the TiO_2 surface however direct oxidation of bacterial components is also possible upon direct contact with TiO_2 surfaces. This occurs directly on membrane components without the ROS as intermediates. The fig. below fig fig. 2.18 represents the mechanism of photocatalytic disinfection with TiO_2 irradiated by UV light.

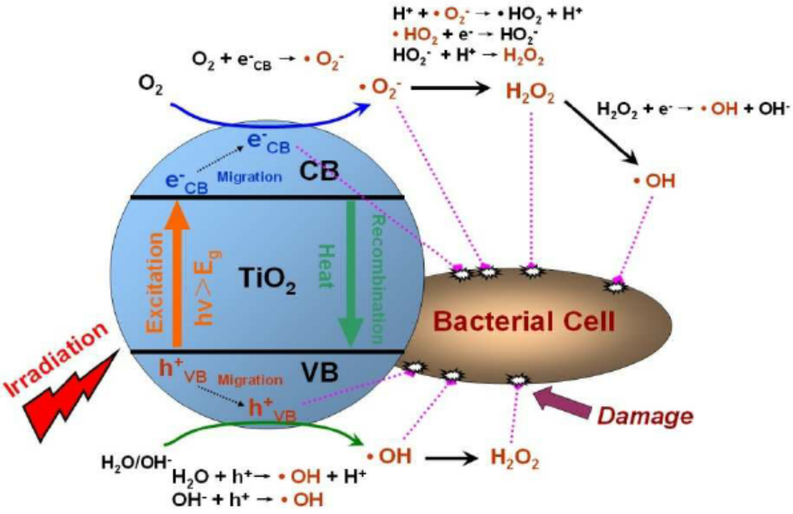

FIGURE 2.18: A schematic diagram illustrating the mechanism of photocatalytic disinfection of TiO_2 irradiated by UV light on a bacterial cell. [94]

Furthermore hydrogen peroxide can also act at a distance if there are ferrous ions present, thus producing the hydroxyl radical via the fenton reactioneqs. (2.26) and (2.27), [35].

$$Fe^{3+} + O^{2-}\cdot \rightarrow Fe^{2+} + O_2 \tag{2.26}$$

$$Fe^{2+} + H_2O_2 \rightarrow Fe^{3+} + OH^- + \cdot OH \tag{2.27}$$

Sunada et al. [95] suggested a three step mechanism in which irradiated TiO_2 surfaces killed bacteria. The first step occurs when the outer membrane is partially damaged, although this does not affect cell vitality but it however alters the permeability of the bacterium making it susceptible to reactive species. The change in permeability enables reactive species to enter the cell thereby attacking the cytoplasmic membrane by lipid peroxidation, that of which *Sunada et al.* considered to be the second step/stage. Within this second stage, the structural and functional disordering of the inner membrane leads to cell lysis. The last step occurs as a result of longer reaction times, where dead bacteria are completely mineralized mainly to CO_2 and H_2O fig. 2.19 [35].

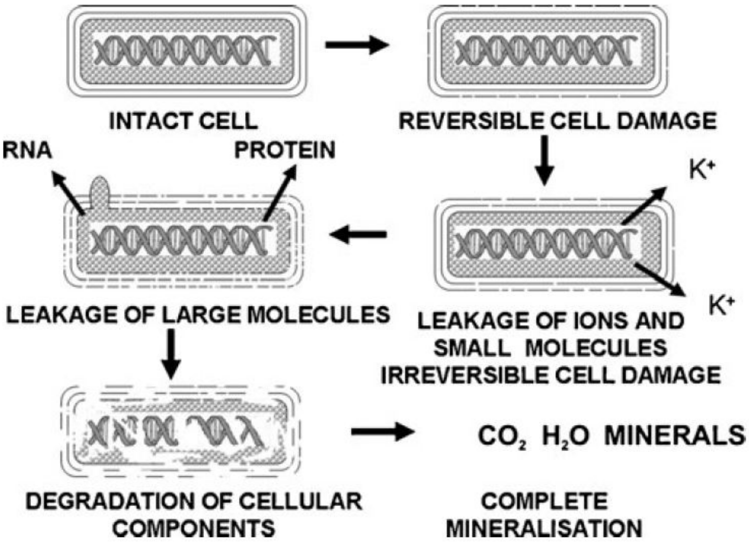

FIGURE 2.19: A schematic diagram illustrating the mechanism of photocatalytic disinfection of TiO 2 on Bacteria. [35]

The oxidizing species that are generated at irradiated tio2 surfaces are important for the photocatalytic activity, that include either trapped or free holes, $^{\bullet}OH$ radicals, $O_2^{\bullet-}$ and

. Holes are thought to be the primary oxidizing species, which are then trapped within picoseconds at the photocatalyst surface. By aid of Transient Absorption, two holes are thought to exist which exhibit absorption at different wavelengths; the deep hole at 520 nm and the shallow at 1200 nm. Shallow trapped holes react rapidly with chemisorbed substances whereas, deep trapped holes on the other hand react with mobile physiosorbed substances due to the localized nature. [86]
$^{\bullet}OH$ radicals that are a result of oxidation of surface hydroxyl or adsorbed water are important in starting oxidation reactions for substances that adsorb weakly on these tio2 surfaces. [86] it is also thought that $^{\bullet}OH$ radicals are produced due to a nucleophilic attack of water on a trapped hole at a surface lattice oxygen.

In addition there are also several reactions of H_2O_2 which is produced by either the reduction of molecular oxygen or the disproportionation of superoxides that could both produce $^{\bullet}OH$ that can either be surface absorbed or free [86]. Superoxide, $O_2^{\bullet -}$, plays a role in the complete mineralization of organic substances but more interestingly as reported by *Nosaka et al.* [96] the reaction between a superoxide and a trapped hole lead to the formation of a singlet oxygen, $1O_2$, of which is a strong oxidant. However this oxidant has a short lifetime in comparison to $^{\bullet}OH$ radicals and trapped holes thought to be a result of rapid deactivation of the singlet oxygen at TiO_2 surfaces. Molecular oxygen is also an essential in that it generates the active species $1O_2$, H_2O_2 and $O_2^{\bullet -}$ that are part of the catalytic reactions described above. In addition molecular oxygen also accelerates the mineralization of organic substances as postulated by *Sundua et al.* [95]. Furthermore *Berger et al.* [97] showed that molecular oxygen not only captures photogenerated electrons thus suppressing charge recombination, but also improves the charge separation thereby making it possible to trap more photogenerated holes. Molecular oxygen is also vital in maintain the stoichiometry of TiO_2, where under O_2 deficient conditions, oxygen atoms at the surface of TiO_2 would be lost during photocatalytic reactions due to hole trapping resulting in loss of the photocatalytic activity [86, 98]

Studies carried out by *Yoshihiko et al.* [99] showed that the photocatalytic reactions could occur at remote distances away from the TiO_2 surface. The different oxidizing species produced could act at several impact distances from the TiO_2 surface in different reaction media.

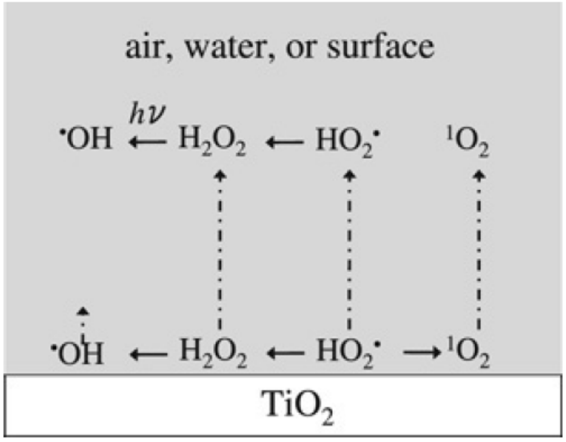

Figure 2.20: Illustration of the active oxygen species related to the photocatalytic tio2 surfaces and their diffusion away from the irradiated tio2 surface. [86]

Chapter 3

Materials and Methods

3.1 Deposition of Nanoparticles into Polystyrene film

3.1.1 Copper cluster deposition using Magnetron Sputtering

For this thesis, Cu NPs are produced using the cluster-beam technique with the advantage of specifically controlling the size regime of the NPs to be produced.

For experimental purposes, a MaSCA is utilized to produce size selected Cu clusters. The schematic picture of the apparatus can be seen in fig. 3.1 and detailed description can be found in [100]. The experiments are carried out under vacuum, where first the copper target is sputtered by a plasma and the clusters are then nucleated in the aggregation chamber, from which they are expanded through the nozzle. Following this, the clusters are collimated into a beam using a skimmer. The beam then passes through an Einzel and two pairs of deflectors, by which it can be focused and the direction can be adjusted in order for the beam to enter the Quadrupole Mass Selector (QMS), where the clusters can be size selected and deflected at an angle of 90° into the deposition chamber. All chambers are evacuated by turbomolecular pumps that are backed by rotary vane pumps, where a background pressure of 1×10^{-7} mbar is necessary prior deposition.

A copper target of 99.999 % purity purchased from Goodfellow Ltd is applied for cluster formation. Size-selected Cu_n clusters are then deposited on clean quartz, Si, as well as

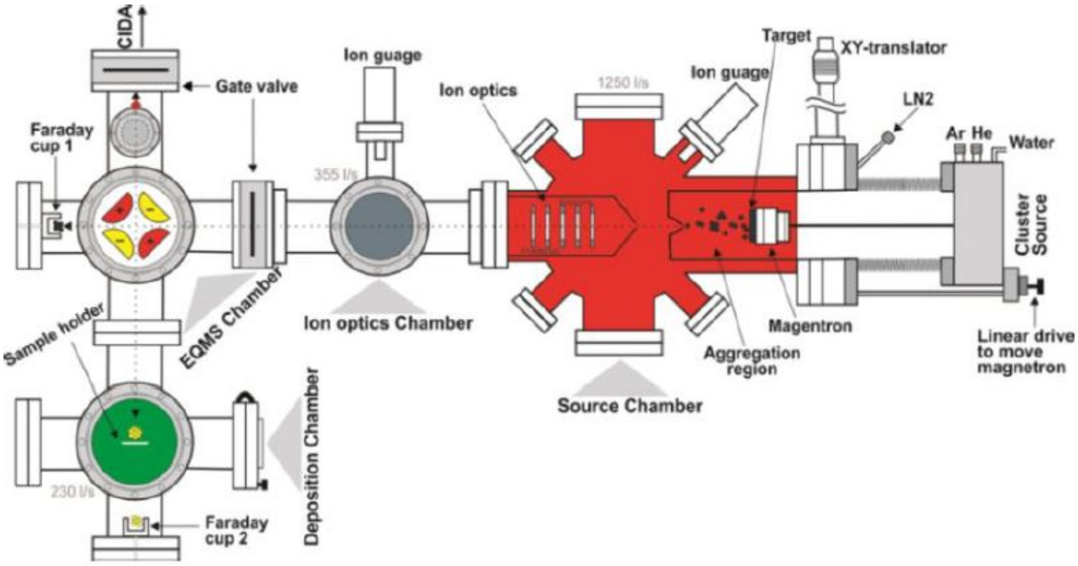

FIGURE 3.1: Schematic representation of magnetron sputtering cluster apparatus [100].

Si and quartz spin coated with 50 nm thick PS films. For the size-selection a quadrupole voltage, $U_Q = \pm 500\,\mathrm{V}$ is applied, furthermore the deposition time is varied in order to obtain differnt cluster surface coverage.

The magnetron source NC200U-B nanoclustersource, used in this experiment is purchased from Oxford Applied Research. The source consists of a planar magnetron coupled with water cooling behind the target so as to keep the temperature in the thermal regime in order to facilitate cluster formation. The target cathode distance can also be adjusted, which in this experiment is set to 0.3 mm. Furthermore the source has a line for the sputtering gas and an additional two lines to supply for different carrier gases. In this report Ar is used as the sputtering gas whereas He is supplied as the carrier/aggregation gas. The source is then externally supplied with the necessary voltage to ignite the plasma; it also consists of a linear drive that can be used to vary the distance between the sputtering source and nozzle. This linear drive can be used to control the path length in the aggregation tube. Moreover the aggregation tube itself is cooled using liquid nitrogen that flow around coils wrapped around the aggregation tube [101].

Another vital component is the electrostatic quadrupole mass spectrometer (QMS) that consists of four equally separated cylindrical electrodes surrounded by a grounded shield.

These electrodes are separated into pairs with bias voltage and opposite polarity. Approximating the electrodes as hyperbolic entails then the voltage which is applied U_Q, will result in an electric field consisting of hyperbolic equipotential lines. Hence a particle having a kinetic energy of, $E_{kinetic} = \frac{mv^2}{2}$, with mass m and velocity v is then equal to the electrostatic energy/pass energy of the quadrupole:

$$E = U_{QP} \times q \tag{3.1}$$

where q is the particle charge. This energy in turn should balance the kinetic energy of a particle and thus the relation;

$$\frac{m}{q} = \frac{2 \times U_{QP}}{v^2} \tag{3.2}$$

Consequently one can size select for the clusters size by manipulating the voltage applied under the assumption that all the particles have the same charge and velocity. An image of the quadrupole mass selector along with a schematic representation of the beam path through a QMS can be seen in the fig. 3.2. When an electrical potential is applied, the electrodes produce a hyperbolic equipotential field that will in turn deflect the clusters in opposite directions as a result of their charge as illustrated in fig. 3.2(b) and hence by tuning the potential the clusters of a certain mass can be selected.

The parameters used for Copper cluster deposition can be seen in section 3.1.1.

Sample	*Ar(sccm)*	*He,(sccm)*	*Cluster current(pA)*	*temperature(° C)*	*Deposition time(mins.)*
Sample 1	69	6	26	-22	20
Sample 2	71	2	27	-22	22
Sample 3	71	2	25	-23	22
Sample 4	70	6	18	-23	21
Sample 5	70	2	31	-22	30
Sample 6	70	2	28	-22	25

TABLE 3.1: The experimental parameters used for Cu NP deposition. Samples 1-4 were deposited on quartz, whereas sample 5 & 6 were deposited on Si. The samples contained 50 nm PS that was spun prior deposition of clusters.

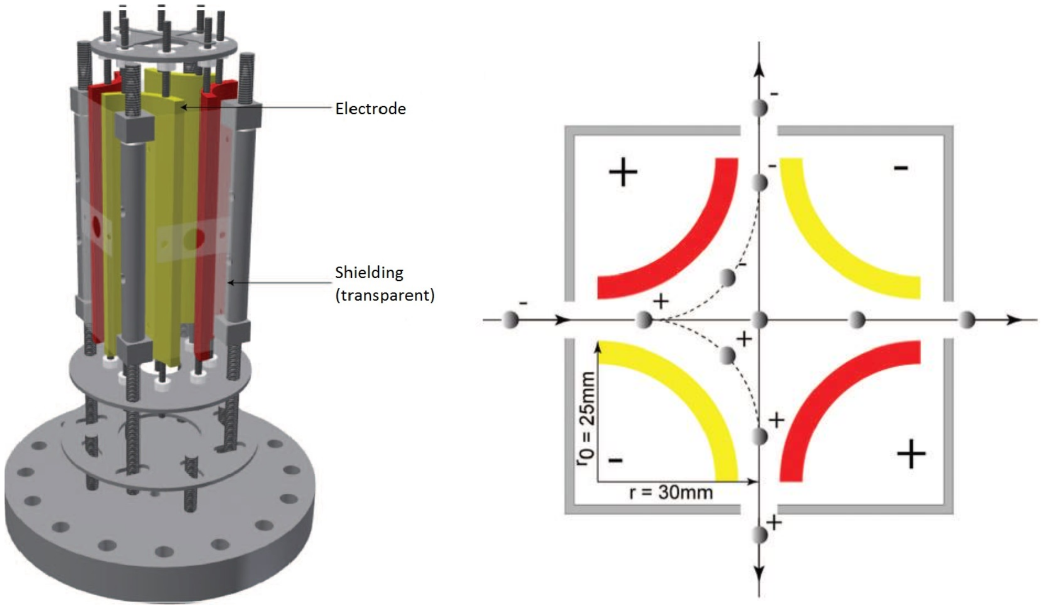

(a) (b)

FIGURE 3.2: Illustration of (a) the QMS applied for the size selection of clusters and (b) shows a cross section of the QMS with trajectory of the particles [102].

3.1.2 Titanium Dioxide Clusters prepared by Gas Aggregation Cluster Source

Furthermore the TiO_2 NPs used in this report are produced in collaboration with Prague univeristy. Si and Quartz substrates with and without 50 nm thick PS films were first prepared in house, before cluster deposition in Prague. The TiO_2s clusters were prepared using GAS, were for this deposition technique, the magnetron is located inside a cooled aggregation chamber. Meaning in this case the magnetron is separated from the rest of the deposition chamber by a small orifice. Since the magnetron is separated from the rest of the deposition chamber, sufficiently high pressure that is needed to produce and drag the NPs through the output orifice can be obtained before deposition unto the desired substrate in the deposition chamber . The TiO_2 cluster deposition is shown infig. 3.3 which consists of a gas aggregation source, attached onto a deposition chamber that is pumped by rotary and diffusion pumps to a pressure of 10^{-4} pascal. The GAS. The source of material for nanoclusters production is a DC, water-cooled magnetron equipped with a Titanium target (purity 99.99

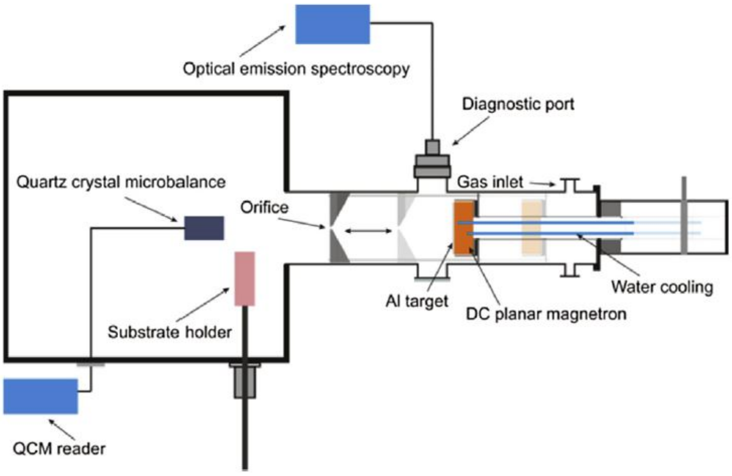

FIGURE 3.3: Illustration of the Gas Aggregation Cluster source . [103]

Furthermore the prepared TiO_2 NP nanocomposites have either, not been oxidized after deposition, oxidized after deposition or oxidized during flight mode and are designated respectively as type 1,2 or 3 fig. 3.4in this thesis.

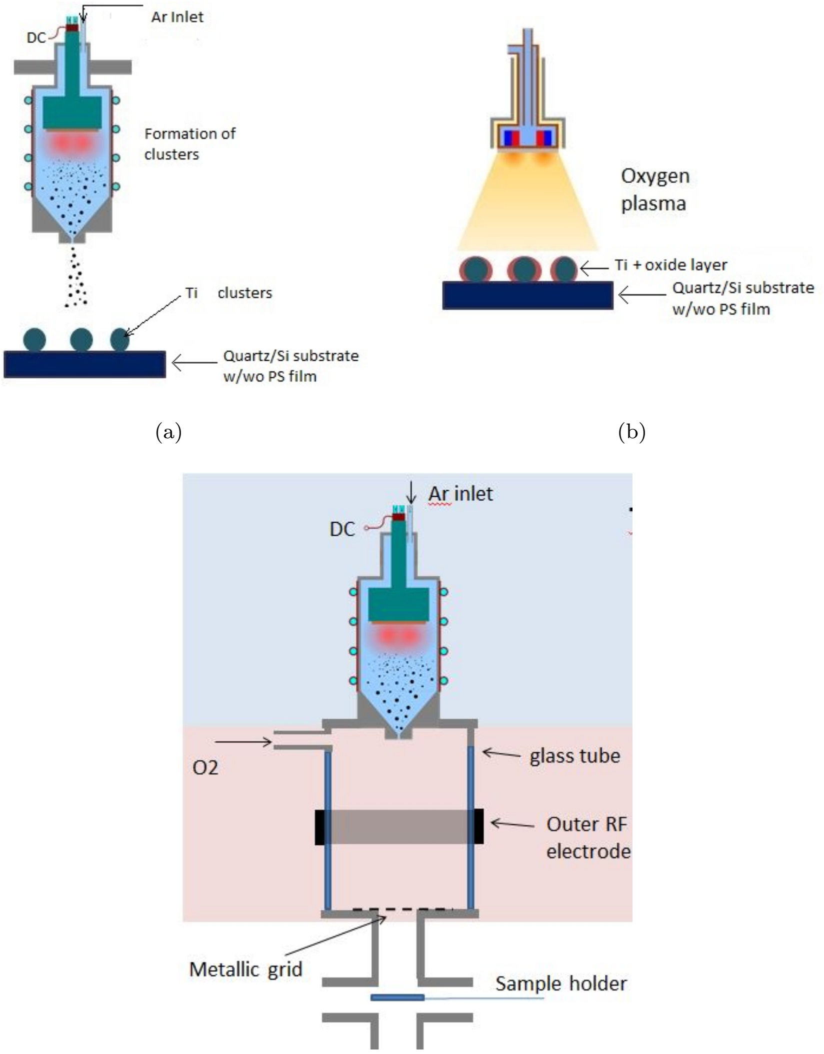

(a) (b)

(c)

Figure 3.4: Illustration the different types of clusters that were produced for this thesis which include; (a) that were deposited on the substrates with no treatment during or after deposition. The second type (b) that were oxidized after deposition onto substrates with oxygen plasma treatment. Lastly type 3, (c), that were oxidized in flight during cluster formation.

3.2 Lauria Bertini Medium and *E.coli* culture preparation

At first Luria Bertani (LB) medium for *E.coli* and for agar platting is prepared, for this a 500 mm blue cap flask as well as a 250 mL Erlenmeyer flask is used. In the blue cap flask 250 mL LB medium is prepared and for the main culture agar plates 40 ml LB medium (20 ml per plate) is prepared. For the 250 mL LBmedium the following ingredients are weighed out; 2.5 g Tryptone (91079-40-2), 1.25g Yeast extract(8013-01-2) and 2.5 g NaCl are mixed in 100 mL mili-Q water before filling to a final volume of 250 mL of which the ingredients are represented in the table below 3.2. Whereas for the main culture Agar plates 0.4 g Tryptone, 0.2 g Yeast extract, 0.28 g NaCl and 0.375 g Agar (9002-18-0) are weighed out and mixed in 40 mL mili-Q water.

Table 3.2: Ingredients used for preparation of LB medium

Compound	*Amount needed*	*CAS #*	*Supplier*
Tryptone	5.0 g	91079-40-2	AppliChem. GMBH
Yeast extract	2.5 g	8013-01-2	Merck Industries
Agar	3.75	9002-18-0	AppliChem. GMBH
NaCl	2.5	7647-14-5	...

Following this the solutions are allowed to mix on a magnetic stirrer for approximately 20 mins. before being autoclaved at 121 °C and 1 bar in order to ensure sterility. After autoclaving the agar solution is then allowed to cool (to approximately 50 °C) whilst being stirred before pouring into sterile petri dishes. For each petri dish 20 ml of the LB agar is poured and allowed to cool. After the agar is hardened the petri dishes are inverted and stored in the refrigerator at 4 °C, Over Night (ON).

In order to prepare the *E.coli* culture for platting, *E.coli* cells from (company and batch no) are used. Two separate liquid cultures are prepared. The first where 4 µL of the *E.coli* cells are mixed in 4ml of LB medium whilst for the other 8 µL of *E. coli* are mixed in a separate 12ml sterile tube also containing 4 ml LB medium. This is done to obtain a 1:1000 and 1:500 solution for the pre culture growth respectively. The solutions are then placed in the incubator shaker set at 230 rpm and 37 °C and are grown ON.

3.2.1 Streaking of *E.coli* culture onto Agar plates

Following the pre culture growth, a sterile inoculum loop of 10 µL volume is used to streak the ON culture, fig. 3.5, to the already prepared agar plates after which the edges of the agar plates were sealed with parafilm. The plates were then inverted and placed in the incubator set at 37 °C and allowed to grow ON.

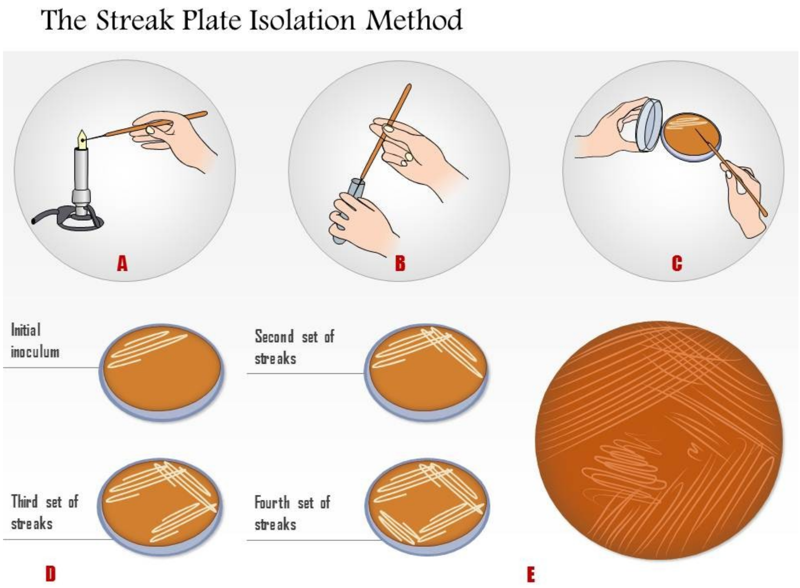

FIGURE 3.5: The streak plate isolation method used to obtain single colonies of bacterial cells [104].

The following day a colony is selected and placed into a sterile flask containing 4 mlof LB media in order to produce a liquid pre-culture. The4 ml of LB media is extracted from the stock solution in the presence of a lit bursen burner in order to create an upward airflow thus preventing contamination of the stock LB media. The sterile flask is then placed in the incubator set at 30 °C so as to extend the lag phase and allowed to grown for 14 hours. Subsequently 240 ml of fresh LB media is also prepared and The3.6 g agar is added to the solution before being autoclaved. This LB agar solution is then allowed to cool to approximately 50 °C before being poured unto sterile petri dishes. This procedure produces 12 LB agar petri dishes of which 6 are to be used for plating the dilution series to be carried out the following day. Henceforth the petri dishes are then inverted and stored in the refrigerator set at 4 °C.

3.2.2 Main culture, dilution series and OD measurements

After having grown the pre culture ON, 1ml aliquot is extracted and placed into a 200 ml Erlenmeyer flask containing 49 ml LB media. The inoculum is then sealed with a sterile cap and placed into the incubator set at 37 °C and 230 rpm, whilst the pre culture is placed in an ice bath to stop cell growth and 2ml is used to measure the Optical Density (OD) using the UV 1800 spectrophotometer.

The inoculum is then allowed to grow and the OD is measured periodically after 20 mins. Once the OD has reached between 2 to 2.5, a volume of 225 µL of the inoculum is extracted and placed into a 12ml sterile flask containing 2.25ml LB media (that is placed in an ice bath). This solution then represents the 1:10 dilution, the procedure is repeated where 225 µL is extracted from the 1:10 dilution and added to another sterile flask with 2.25ml LB media to produce dilutions of 1:100 and henceforth up to a solution of dilution 1:10^6 . Prior to extracting the aliquot the flask is shaken to ensure proper mixture of the solution.

After carrying out the serial dilutions the OD is also measured with the UV-1800 spectrophotometer, a blank is also measured using the LB media. Following the OD measurements the different dilutions are then plated onto the pre prepared agar plates. For this procedure 50 µL of the different solutions are pipetted onto six different LB agar plates representing the different dilutions of 1:10 to 1:10^6. The pipetted volume is spread onto the plates using a Drigalski Spatula. The Drigalski Spatula is first immersed in ethanol and then quickly passed through a Bunsen burner to ignite the alcohol thereby sterilizing it. Once cooled, it can then be used to evenly spread the pipetted bacterial solution on the agar plates. The LB agar plates representing the different dilutions are then placed in an incubator set at 37 °C and allowed to grow ON. These agar plates can then be used to count the number of CFU and additionally for plotting OD vs. cell number.

To measure the OD, the photometric mode is chosen in the UV 1800 spectrophotometer. The wavelength of 600 nm is selected for this purpose, additional wavelengths of 480 nm and 540 nm can also be selected. After creating the measurement mode, the spectrophotometer is slewed and auto zeroed(when measuring blank) by choosing the appropriate commands on the user interface. Following this the samples are loaded into the spectrophotometer and the OD measurements of the micro cuvettes containing the different dilutions (1:10 to 1:10^6) of the *E.coli* solutions are carried out.

Additionally the growth curve of the inoculum is obtained by measuring the OD of the solution periodically after 20 mins. The flask is shaken prior to extracting 2ml of the solution and placing in the 1mm cuvette.

3.2.3 Estimating Bacterial colonies using ImageJ

For analyzing the colonies as well as to count them the software image j version 4.0.5 is applied. An image of the agar plate is first uploaded to the software. The software is used to analyze images that contain many cells on the agar plates, where automated counting is easier. The image is first opened by selecting open image on the user interface. As the image is a coloured image (RGB) it is first converted to a grey scale image before proceeding. This is done under the option image then type and convert to greyscale is chosen (either 8 or 16 bit). Once done, the background is then subtracted from the image. Following this, the threshold is then adjusted in order to highlight the structures of interest, which are the cells to be counted. The threshold is set under the image option → Adjust → threshold. Upon completion the image will be converted to a binary image with only two pixel intensities, i.e black = 0 and white = 255.

In order to avoid any difficulties with the threshold, one can also prior to converting the image to a binary image, select the area of interest. This is done by chosing the circle/oval selection tab on the user interface and highlighting the area of interest after which the rest of the area can be cleared under the Edit → clear outside option on the user interface. Once completed the binary image can be produced under the option process → binary→ make binary. In adittion if the cells/colonies appear to overlap then under the option Process → Binary → watershed, one can separate colonies. This is done by adding a 1 pixel thick line where the division should be.

Lastly after obtaining the 8/16 bit binary image of the colonies to be counted, the Analyze option is chosen thereafter Analyze Particles(in this case the colonies). Various parameters for the colonies can then be set, such as the size by either and/or adjusting the pixel size. This is useful if many small ‘noise’ pixels are counted as pixels or when interest is in excluding certain sized colonies. Furthermore the circularity parameter excludes colonies/particles based on their circular configuration. The default range is between 0.00-1.00, where perfect circles are 1.00 and 0.00 is a straight line.

Colonies are then outlined (or by choosing mask count, the counted colonies are displayed) and the results window will then display the corresponding data for individual colonies whilst the summary table shows the total count of colonies fig. 3.8 [105].

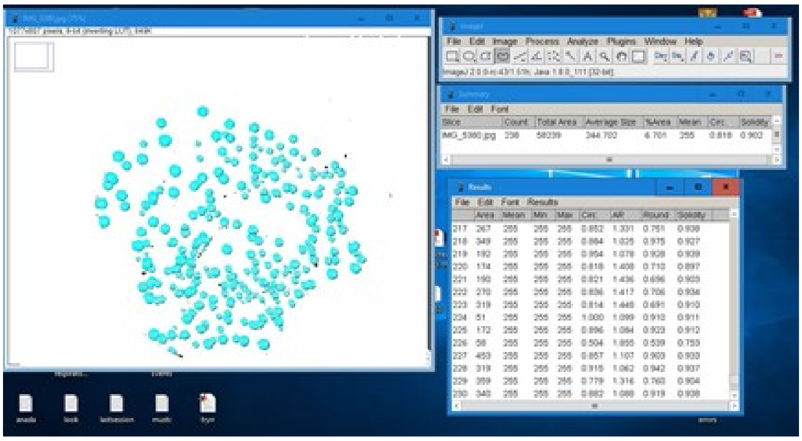

Slice	Count	Total Area	Average Size	%Area	Mean	Circ.	Solidity
IMG_5380.jpg	238	58239	244.702	4.701	255	0.818	0.902

	Area	Mean	Min	Max	Circ.	AR	Round	Solidity
217	267	255	255	255	0.852	1.331	0.751	0.938
218	349	255	255	255	0.884	1.025	0.975	0.927
219	192	255	255	255	0.954	1.078	0.928	0.939
220	174	255	255	255	0.818	1.408	0.710	0.897
221	190	255	255	255	0.821	1.436	0.696	0.903
222	270	255	255	255	0.836	1.417	0.706	0.934
223	319	255	255	255	0.814	1.448	0.691	0.910
224	51	255	255	255	1.000	1.099	0.910	0.911
225	172	255	255	255	0.896	1.084	0.923	0.912
226	58	255	255	255	0.504	1.855	0.539	0.753
227	453	255	255	255	0.857	1.107	0.903	0.933
228	319	255	255	255	0.915	1.062	0.942	0.937
229	359	255	255	255	0.779	1.316	0.760	0.904
230	340	255	255	255	0.882	1.088	0.919	0.938

FIGURE 3.6: ImageJ user interface and colony counter application used to estimate number of bacterial cells [106].

3.3 Experimental set up Antibacterial Effect of Polymer-metal Nanocomposities

3.3.1 Photocatalysis of Titania nanocomposites on *E.coli*

In order to test the antibacterial effects of the prepared titania nanocomposites, the same procedure for preparing a main culture as presented in section 3.2.2 is carried out once again.

At first having grown the ON culture, see section section 3.2.2, 200 µL is extracted and placed in a sterilized Erlenmeyer flask containing 9 ml LB media. The aliquot is then placed in the incubator shaker set at 37 °C and allowed to grow to an OD of 0.248, which is measured using the UV-1800 shimadzu spectrophotometer, as expressed section 3.2.2. Once at this OD, a volume of 225 µL is extracted and a serial dilution is performed up to the dilution factor of 1:10^5 using 2.25 ml LB media. The diluted solution is then used to carry out the antibacterial tests of the prepared nanocomposite materials. Here a volume of 200 µL of the diluted solution is extracted and deposited on a substrates containing the titania nanocomposite, i.e Si wafer with 50 nm spin coated PS film and TiO_2 NP, as well as substrates without spin coated PS film, i.e. Si wafer with TiO_2 NPs deposited on the surface. One of each sample is used as the control whilst another is exposed to Ultraviolet light using a UV lamp see fig fig. 3.7below.

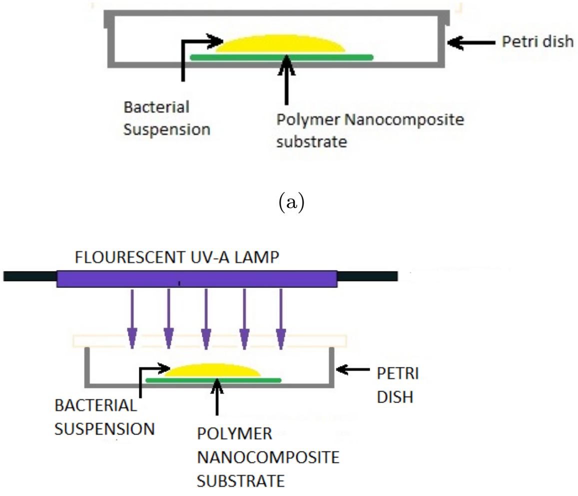

(a)

(b)

Figure 3.7: Illustration of the Titania photocatalysis experiment on *E.coli* bacterial suspension; (a) that shows the control experiment setup. Also shown is the UVA experiment (b) utilizing a fluoresecent uva lamp to photoactivate the TiO_2 NPs on the substrate used.

The experiment is carried out for 1,5,10,20 and 120 mins before extracting 50 µLs and depositing unto already prepared agar plates. The deposited solution is then spread using the spread plate method described in section 2.3.1.1. Once allowed to dry, the plates are sealed, inverted and then placed in the incubator set at 37 °C and allowed to grow ON. After 24 hrs has elapsed the number of cells are estimated using ImageJ as described in section 3.2.3 before plotting the number of cells from the control sample vs the UVA irradiated sample for each substrate.

3.3.2 Copper nanocomposites antibacterial effect on *E.coli.*

Similarly when testing the effects of Cu NPs a bacterial culture is grown as described above. However in this case a UV lamp is not utilized and the control depicts the bacteria suspension deposited on bare substrate without any Cu NPs. Once again the experiment is carried out for 1,5,10,20 and 120 mins before extracting 50 µLs and depositing unto already prepared agar plates. The deposited solution is then spread using the spread plate method described in section 2.3.1.1. Once allowed to dry, the plates are sealed, inverted and then placed in the incubator set at 37 °C and allowed to grow ON. Following this the number of colonies are then estimated using ImageJ.

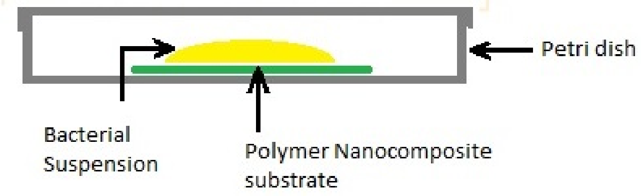

FIGURE 3.8: Illustration of the experimental setup on bacterial effect of Cu NPs on *E.coli*[106].

3.4 Investigation of prepared nanocomposite samples.

Ellipsometry was used in order to study the prepared films prior to any deposition of clusters. Whereas Both AFM and SEM techniques were employed in order to investigate the samples prepared for this work; TiO_2 NPs were mainly studied with SEM and images were used to obtain the height distributions. Whereas Cu NPs were investigated mainly with AFM. Optical spectroscopy on the other hand was used to study the embodiment of clusters into the polymer films and any effects arising therein.

3.4.1 Ellipsometry

Film measurements are carried out using the Sentech SE850 ellipsometer on silicon spin coated by PS films (50 to 90 nm thickness). A model of the sample is constructed using the User interface of the sotware to include the Si/PS/Air layers. The experimental data obtained for each measurement is then compared to the model and subsequently adjusted to fit with the experimental data see fig. fig. 3.10. As for the quartz substrates thickness measurements are not carried out due to the transparent property of quartz. Thickness of the quartz substrates are assumed to be similar to silicon substrates as they are spun with the same parameters.

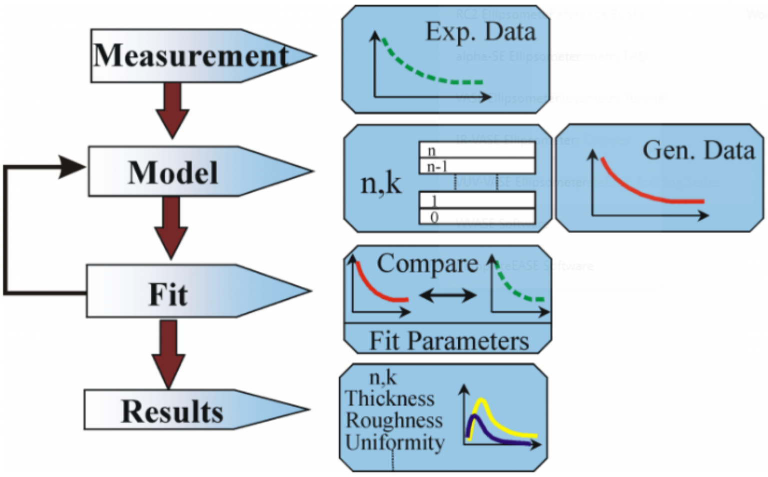

Figure 3.9: Ellipsometry data analysis flow chart. [107]

The Sentech SE850 ellipsometer consists of two compartments. The left compartment is the input box which consists of the source alternator, the compensator the polarizer and the aperture control. The right compartment is the output box with an aperture control, analyzer, detector alternator and NIR detector [108]. The sentech SE 850 is a nulling ellipsometer which minimizes the intensity of the light wave at the detector by adjusting the rotational azimuth angle of the polarizer, the compensator and analyzer. The unpolarized light emitted from the source is linearly polarized by the polarizer. Furthermore by adjusting the azimuth angle of the polarizer and compensator the light can be linearly polarized after reflection from the sample surface and nullified by adjusting the azimuth angle of the analyzer thereby minimizing the light intensity at the detector (i.e can be detected at the sub monolayer precision).

3.4.2 Atomic Force Microscopy

In Atomic force microscopy a cantilever with a sharp tip is used to scan over a samples surface. Once the tip approaches the samples surface close range attractive forces causes the cantilever to be deflected towards the surface. As the cantilever approaches even closer to the sample repulsive forces become stronger and the cantilever is then deflected away from the surface as depicted in fig. fig. 3.11 [110] there are various AFM operating modes as indicated in fig. fig. 3.11 with the most common ones being contact, tapping(semicontact) and noncontact.

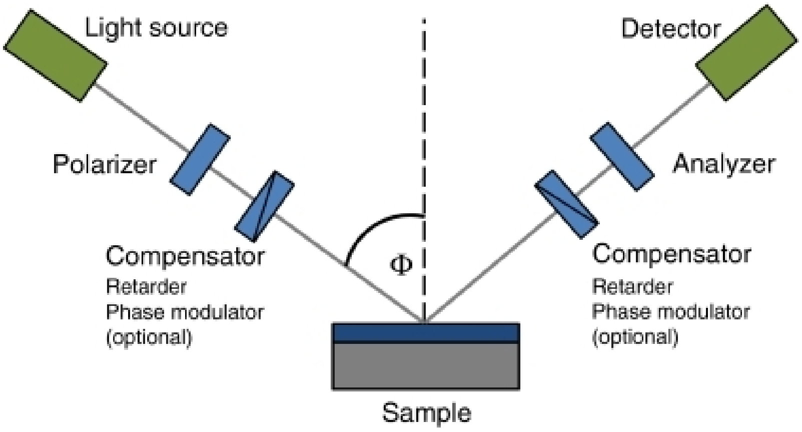

FIGURE 3.10: Schematic representation of the ellipsometer components. [109]

Deflection of the cantilever either towards or away from the surface is measured using a laser beam. Therefore by reflecting an incident beam off the cantilever any slight changes in the direction of the reflected beam will signify changes in the cantilever deflection. Using a position sensitive photo-diode (PSPD) the changes in the direction of the reflected beam and thus cantilever position can be traced [110].

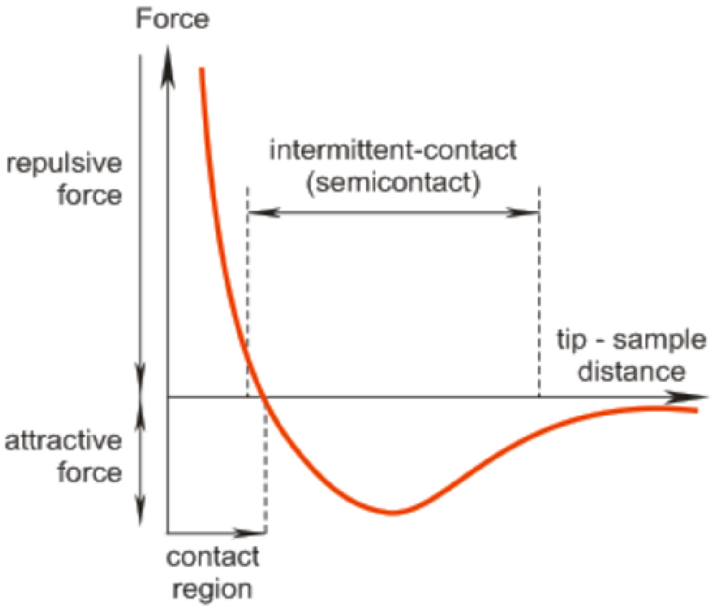

FIGURE 3.11: Chemical structure of propipium iodide. [111]

AFM images are then acquired by scanning the cantilever of over a region of interest. Due to the lowered and raised features on the sample surface the subsequent deflection of the cantilever monitored by the PSPD is then used to map the topography of the samples surface. In addition a feedback loop is used to control the height of the tip above a surface thus maintains a constant laser position in order to acquire an image of the surface features[110].

AFM measurements of the prepared substrates are carried out using the NT-MDT Ntegra Aura AFM, using the semi contact mode. In this mode, the force of pressure exerted on the cantilever towards the surface is less and allows the possibility to work with softer or materials susceptible to damage such as polymers. HA-FM AFM tips purchased from ScanSense are used to carry out the measurements. The frequency range is set to include the nominal value of the cantilevers before carrying out the measurements. The set-point, scan size and scan frequency are then defined and an image is acquired as described above.

3.4.3 Optical spectroscopy

Optical spectroscopy is a non-destructive measurement that uses the propagation of light through matter in order to acquire various properties regarding the material being studied. Optical measurments are thus concerned with the absorbtion, transmittance and reflection of UV-, IR as well as visible light through the medium being measured [112]. Optical measurements are carried out using the LAMBDA 1050 UV/Vis Perkin Elmer spectrophotometer and UV-WinLab software. The spectrophotometer applies two identical beams of light in order to determine the absorbance of a given sample; one beam is the test beam whilst the other is the reference beam. In the case of the test beam, the beam passes through the sample to a photodetector which then measures the irradiance at specific wavelengths. As for the reference beam, the irradiance passes unobstructed to the photodetector. Subsequently the transmittance of the sample is then given as the difference in irradiance between the sample and reference beam at the specified wavelength range. Prior to any measurements the optical spectrometer is set to measure the transmission and the 100% transmission(reference beam) is carried out after which the sample is loaded and transmission is measured from 350 to 800 nms with 1 nm intervals. The measured data is then exported as .csv files and plotted using MATLAB R2016a software, where the transmission spectra are converted to extinction spectra. This conversion is possible as the change of transmittance for the case of LSPR is caused by a combination of absorption and scattering of light.

3.4.4 Fluorescence Microscopy

The absorption and subsequent re-radiation of incident light from an organic or inorganic specimen results from the phenomena known as fluorescence or phosphorescence, depending on the nature of the excited state and time between photon absorption and emission. The emission of light during the fluorescence process occurs from the singlet excited states and is simultaneous with the absorption of the excitation due to a relatively short time between photon absorption and emission. The emission rates of fluorescence are typically around 10^8 s^{-1} that correspond to fluorescence lifetime close to 10 ns. When emission occurs from the triplet excited state and persists longer after the excitation light then the process is termed as phosphorescence. Here the emission rates are much slower (10^3 to 10^0 s^{-1}) since direct transition to the ground state are forbidden. As a consequence, the phosphorescence lifetimes are in the range of milliseconds to seconds [113]. Such processes are depicted in a Jablonski diagram, where the absorption of light results in the formation of an excited molecule that can in turn dissipate the energy through various processes [114].

In the Jablonski diagram the singlet grount, first and second electronic states are depicted by S_0, S_1 and S_2 respectively. At each of these electronic energy levels the fluorophores can exist in a number of vibrational energy levels depicted as 0, 1, 2 and so forth where transitions between the various states are depicted as vertical lines as seen in fig. 3.12. Most molecules only absorb light at specific wavelengths and when a molecule absorbs a photon with one of these wavelengths, the electrons are raised to a higher electronic energy state, S_1, S_2, as well as a higher vibrational excited state, in particular pi-electron systems that are require less energy to excite. This process occurs at a relatively high speed, taking only a fs (10^{-15} s) [113][p.3-5].

To be more precise, upon absorbing photons, a fluorophore is excited to a higher electronic excitation energy level before emitting photons. It is here that processes such as static quenching, collisional quenching, and Fluorescence Resonance Energy Transfer (FRET) take place. These processes are named "internal conversion", which consequently reduce

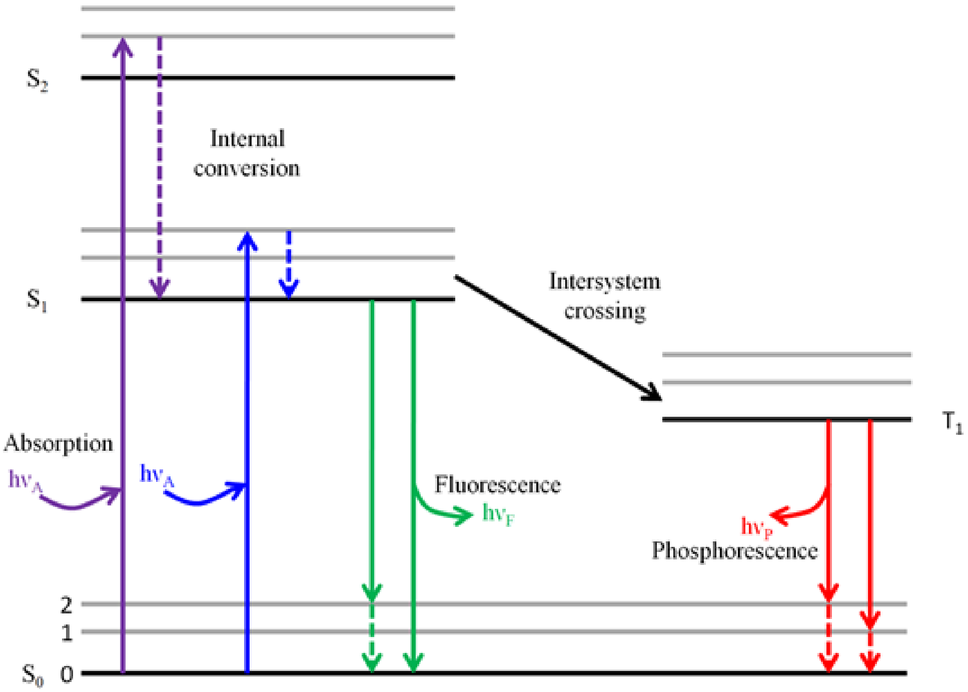

FIGURE 3.12: *A Jablonski diagram showing the excited states S_0, S_1 and the vibrational states. The vibrational states are the lines close to each other. Phosphorescence, which is a long duration light emitting process, is not examined in this report.* Taken from[113]

the electronic energy level to the lowest vibrational level of the first excited state (S_1). This is known as vibrational relaxation, and it takes about a ps (10^{-12} s) for the process to take place, which is what describes the fluorophores lifetime, which is in the range of $1 \cdot 10^{-12}$ to $1 \cdot 10^{-9}$ seconds. Fluorophores have a constant rate of emitting photons, during their emission lifetime. The internal conversion processes all occur faster than the fluorescence emission lifetime, which is why it emits photons from the electronic energy state S_1. When the fluorophore emits photons, it falls to the lowest vibrational state of S_0, returning back to its initial stable condition.[113][p.3-5]

Internal conversion is a non-radiative deactivation process where excess energy is consumed as kinetic energy or heat. Internal conversion occurs at a rate of 10 ps or less. Compared to the fluorescence emission lifetime of an excited molecule, it is much faster and occurs prior to emission. This explains why the fluorescence of a fluorophore is dependent on the lowest energy and vibrational state of S_1.

However vibrational energy is lost when electrons relax from the excited to the ground state. Due to this energy loss the emission spectrum of an excited fluorophore is shifted towards longer wavelengths. This change in emission wavelengths is termed as Stokes shift [113]. When this shift increases in value, it becomes easier to separate excitation from emission by using florescence filters [115] as these filters aid in blocking or passing specific wavelength bands. The efficiency that a certain fluorophore can absorb a photon is based on the excitation coefficient. Flouorophores with larger excitation coefficients means that absorption of a photon in a specific wavelength is more probable to occur. Another important component is the quantum yield, which denotes the ratio the number of quanta emitted to those absorbed with a value between 0.1 and 1. Non-radiative processes such as photochemical reaction or heat result in quntum yield values less than 1. These factors; excitation coefficient, quantum yield and fluorescence lifetimes, contribute to the intensity of measured fluorescence and therefore any imaging carried out using fluorescence microscopy [113].

Fluorescence microscopy has become an important instrument in various biological sciences due to the application of fluorophores that make it possible to identify cells and sub microscopic cellular components with high specificity. The basic function of fluorescence microscopy is to irradiate a sample with specific and a desired band of wavelengths and subsequently separate the emitted fluorescence from the excitation light. This results in only the emitted light reaching the detector so that the fluorescent sample are superimposed with high contrast against a dark background [116]

3.4.5 LIVE/DEAD Assay of Bacterial suspension

Another method employed in this thesis to evaluate the activity of prepared nanocomposites is the widely used LIVE/DEAD Baclight viability test purchased from ThermoFisher. In general bacterial viability assays are applied in various aspects such as in this case to evaluate antimicrobial properties or in other instances to perform microbial monitoring of water. Their application is widespread in areas such as medicine, biotechnology, environmental monitoring and also the food industry [117].

Bacterial viability is assessed indirectly based on the state of the cells by using nucleic acid stains(molecular probes), the membrane potential, redox indicators or reporter gene systems. Cellular and membrane integrity is one of the criterion in distinguishing live and dead bacteria. In the case of viable cells, these cells have intact and tight cell membranes of which are impenetrable by some staining compounds. Dead cells on the other hand have damaged membranes that are susceptible to these staining compounds. For this thesis the bacterial viability kit, Live/Dead Bacterial Viability Kit L-7007, is used to distinguish between live and dead bacterial cells. The kit is composed of two fluorophores STYO9 and propidium iodide (PI) [117].

Propidium Iodide, a red-fluorescent nucleic acid stain, intercalates to DNA and when bound its fluorescence intensity is enhanced resulting in an excitation maximum at 535 nm and fluorescence emission maximum at 617 nm. PI is used to stain dead cells as it only penetrates cells that have disrupted membranes. STYO9 on the contrary is a green fluorescent nucleic acid stain that binds to both live and dead cells. Its intensity is also enhanced when bound to nucleic acid with an excitation maximum at 483 nm and fluorescence emission maximum at 503 nm. In the case of LIVE/DEAD cell staining when both stains are used, STYO9 is displaced by PI as PI has a stronger affinity for nucleic acids and can therefore be used to label damaged (dead) cells [117].

In the case of TiO_2 NP, the live cells are represented as the control experiment without any UV exposure whilst dead cells are taken from the substrate exposed to UV light. Both control and UVA irradiated experiments are carried out for 20 mins and 120 mins.

Prior to illumination experiments, the inocculum is grown to an OD_{600nm} of 0.270 representing the 500 cells ml^{-1}. Following this 1 mL is extracted and diluted in 9 mL LB media. After a short incubation, the sample is centrifuged at 3000 rpm at 4 °C for 5 minutes. After which the supernatant is extracted and the pellet is re-suspended in PBS buffer(pH 7.4) solution. A volume of 100 µL of the bacteria solution is then deposited on the substrates. Once the indicated exposure times have elapsed, the same volume is extracted and mixed with the staining dye (1.5 µL ml^{-1} of bacteria solution) and allowed to react in the dark at room temperature for 20 mins.
Fluorescence images of bacteria subjected to Cu NPs are also acquired in the same manner, however as mentioned in the previous section section 3.3.2 illumination with UV light is not used for Cu NPs and the control samples designate bacteria suspended on bare substrate for the indicated times of 20 mins and 120 mins prior fluorescence imaging. Fluorescence microscopy measurements are then carried out using the OLYMPUSI71 microscope. The OLYMPUS IX71, fig. 3.13 is an example of an inverted epifluorescence microscope used primarily for tissue culture applications. The microscope consists of a xenon/ mercury lamp-house stationed at the rear of the microscope frame. Fluorescence illumination from the arc discharge lamp travels to a collector lens and into a cube which contains a set of interference filters that include a barrier filter, excitation filter and a dichroic mirror. The excitation filter allows light of a particular wavelength to pass through to the dichroic mirror where it is reflected into the objective and towards the sample. Secondary fluorescence emitted by the sample passes through the dichroic mirror and emission filter and on to the detector. [115] and [116] Images are then captured using the DP71 camera attached to the microscope.

After initialization of the microscope, the sample is loaded onto a glass slide by trapping 5 µL of the bacterial solution. Once loaded unto the sample holder, the desired optical zoom is chosen and the focus is corrected. For this experiment the 60/40X optical zoom is applied. In order to image the LIVE/DEAD cells the FITC filter is applied for Styo9 (emission/excitation:498 nm/485 nm) and the DAPI filter for PI(emission/excitation:617 nm/535 nm) to visualize the live and dead cells respectively.

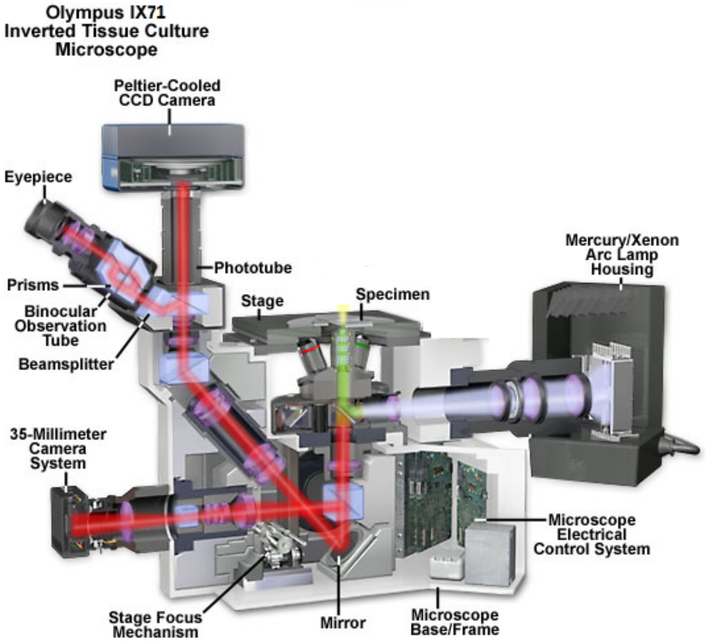

FIGURE 3.13: The Olympus IX71 inverted microscope used for fluorescence imaging of the Live/Dead Bacterial assay[118]

3.5 List of Chemicals and Equipment Used for Experiments

Listed below in table 3.3 and 3.4 are the chemicals as well as the equipment respectively, that were used to carry out the experiments for this report.

TABLE 3.3: List of chemicals used for experiments

Compound	*CAS #*	*Supplier*
Polystyrene (M_w 192,000 g/mol)	9003-53-6	Sigma Aldrich
Toluene	108-88-3	Sigma Aldrich
Acetone	67-64-1	Sigma Aldrich
Isopropanol	67-63-0	Sigma Aldrich
Yeast extract	8013-01-2	Merck Industries
Tryptone	91079-40-2	AppliChem. GMBH
Agar	9002-18-0	AppliChem. GMBH

Table 3.4: List of equipments used for experiments

Brand	*Model*
Ultrasonic bath	
Martin Walter	Ultraschalltechnik AG
Spin coater	
Laurell	WS-650S 23NPP/C2/IND
Ellipsometer	
Sentech instruments GMBH	SE850
Atomic force microscopy	
NT-MDT	Ntegra Aura
AFM cantilever	
Optical transmitance spectroscopy	
Perkin Elmer High Performance	Lambda 1050 spectrometer
Spectrophotometer	
UV Spectrophotometer	UV - 1800 shimadzu
UV Lamp	
UVA lamp	F15T8/BLB
Flourescence Microscope	
OLYMPUS I71	

Chapter 4

Results and discussion

4.1 Characterization of Polystyrene Composites with Metal Nanoparticles

4.1.1 Scanning Electron Microscopy Images of Titania Metal Composites

Using the SEM images the TiNPs diameter are then estimated by the software ImageJ. At first the scale is set by measuring the one given on the SEM image. This is done using the measure tool on the user interface using the straight line selection tool to make a line selection that corresponds to a known distance.

This is used to define the spatial scale of the active image so measurement results can be presented in calibrated units, such as nm. The measurement is calibrated under the option Analyze. The Known Distance and unit of measurement are then entered. Once the scale is set the individual particles can then be measured.

In order to measure a particle is outlined using the *oval/elliptical/brush* selection tool, once measured a result table is displayed with the parameters; Area, perimeter, major and minor axis, and shape descriptors.

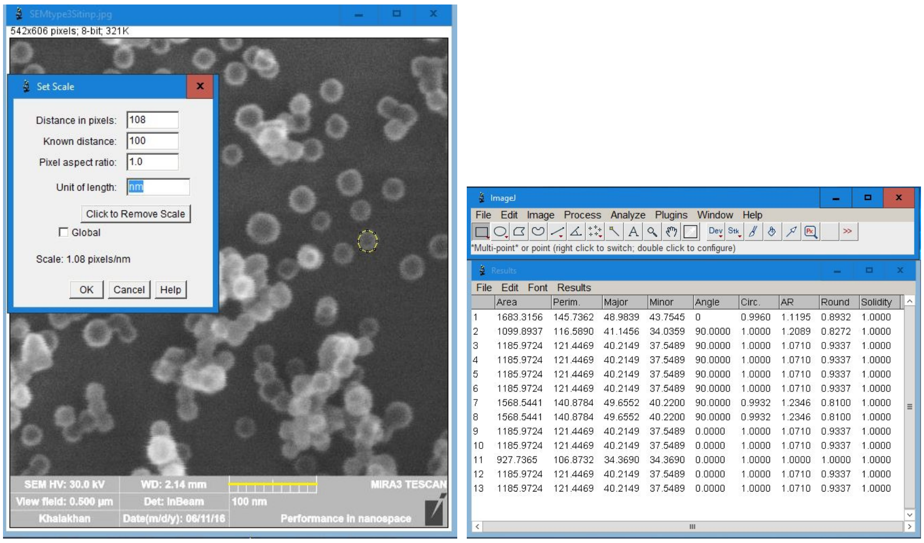

542x606 pixels; 8-bit; 321K

Distance in pixels: 108
Known distance: 100
Pixel aspect ratio: 1.0
Unit of length: nm
☐ Global
Scale: 1.08 pixels/nm

Multi-point or point (right click to switch; double click to configure)

	Area	Perim.	Major	Minor	Angle	Circ.	AR	Round	Solidity
1	1683.3156	145.7362	48.9839	43.7545	0	0.9960	1.1195	0.8932	1.0000
2	1099.8937	116.5890	41.1456	34.0359	90.0000	1.0000	1.2089	0.8272	1.0000
3	1185.9724	121.4469	40.2149	37.5489	90.0000	1.0000	1.0710	0.9337	1.0000
4	1185.9724	121.4469	40.2149	37.5489	90.0000	1.0000	1.0710	0.9337	1.0000
5	1185.9724	121.4469	40.2149	37.5489	90.0000	1.0000	1.0710	0.9337	1.0000
6	1185.9724	121.4469	40.2149	37.5489	90.0000	1.0000	1.0710	0.9337	1.0000
7	1568.5441	140.8784	49.6552	40.2200	90.0000	0.9932	1.2346	0.8100	1.0000
8	1568.5441	140.8784	49.6552	40.2200	90.0000	0.9932	1.2346	0.8100	1.0000
9	1185.9724	121.4469	40.2149	37.5489	0.0000	1.0000	1.0710	0.9337	1.0000
10	1185.9724	121.4469	40.2149	37.5489	0.0000	1.0000	1.0710	0.9337	1.0000
11	927.7365	106.8732	34.3690	34.3690	0.0000	1.0000	1.0000	1.0000	1.0000
12	1185.9724	121.4469	40.2149	37.5489	0.0000	1.0000	1.0710	0.9337	1.0000
13	1185.9724	121.4469	40.2149	37.5489	0.0000	1.0000	1.0710	0.9337	1.0000

(a) (b)

FIGURE 4.1: An example of an image used to analyze particle size distribution; (a) here the background has been subtracted and scale set. The second image displays the results obtained upon measuring the distribution of the particles (b) with parameters such as the area, shape descriptors etc.

As the particle size of a spherical object can be defined by its diameter, using the Area from the particles analysed one can then proceed to estimate the diameter. Here the diameter of the sphere is calculated using the expression below eq. (4.1).

$$r = \sqrt{\frac{A}{\Pi}} \tag{4.1}$$

Once the diameter is calculated, the size distribution of the analyzed particles is plotted as a histogram in MATLAB R2016a [119] using the *hisfit*(data,bins,'distributionfit') option that also includes a distribution fit of the data. Using the data obtained for the particle size, Matlab is also used to give the mean particle size as well as the standard deviation.

The SEM fig below fig. 4.2, shows the type 1 substrate were the TiO_2s were not treated neither during or after deposition as illustrated in fig. 3.4(a) section 3.1.2 . The first image fig. 4.2(a) is taken at a viewing field of 2 µm showing a large number of TiNPs that appear to cover most of the Si wafer surface. At some instances one can see clusters having being deposited on other clusters thereby forming aggregates. Upon close examination of the figure as shown in fig. 4.2(b) where the view field is 554 nm, one is able to see the before mentioned aggregate of clusters formed during deposition. Furthermore the TiNPs deposited represent the different polyhedral packing structure of atoms when forming clusters [120].

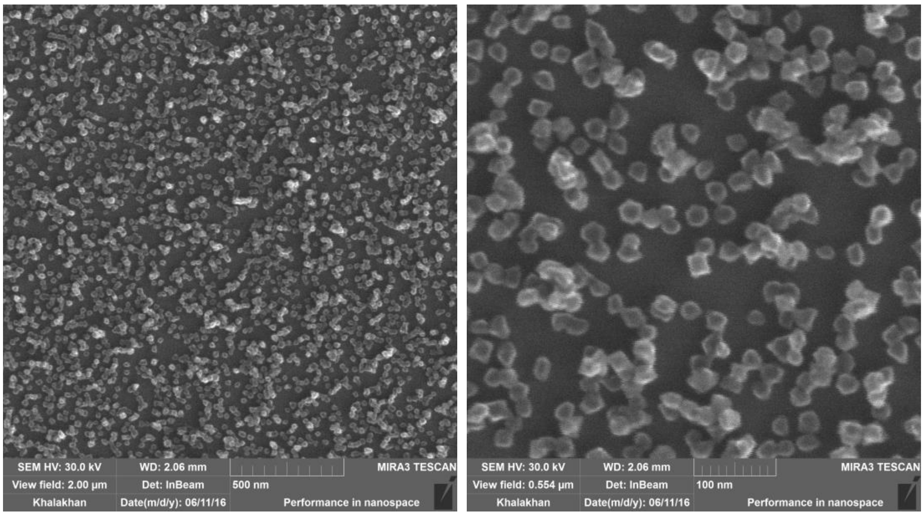

(a) (b)

Figure 4.2: SEM images showing the TiNP prepared for this thesis where (a) is type 1 substrate with TiNPs on bare Si and (b) is a high magnification of (a) .

Furthermore using the image (b) the diameter of the particles deposited were estimated as described previously using imageJ and Matlab R2016a, where the distribution of nanoparticle diameter is given in fig. 4.3. On the figure the mean distribution of the particles was calculated to be 18.9 nm with a corresponding standard deviation of 1 nm. The distribution shown in fig. 4.3 also includes both smaller and larger particles that occur at a much lower frequencies.

Type 2 substrates were also investigated with SEM and is shown below in fig fig. 4.4. As was the case in the previous image, one is able to observe cluster aggregates that formed during deposition. Furthermore upon close examination of the figure as shown in fig. 4.4(b) where the view field is 500 nm, one is able to see the aggregate of clusters formed during deposition.

Using the image, fig. 4.4(b), the diameter of the particles were estimated as described previously using imageJ and Matlab R2016a, where the distribution of the nanoparticle

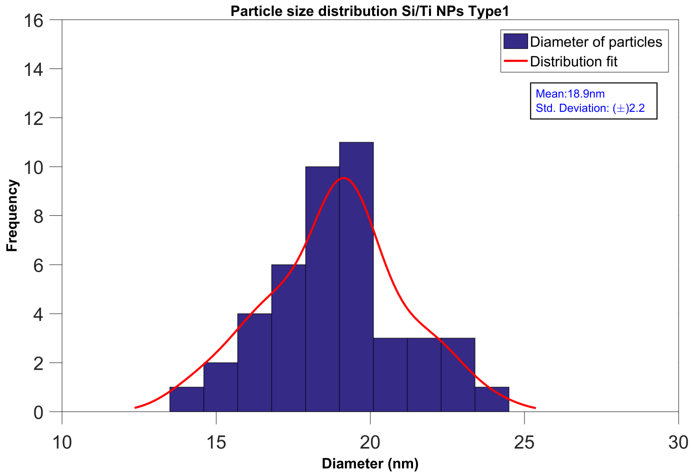

FIGURE 4.3: The diameter distribution of TiNPs on type 1 substrate shown in fig. 4.2. The mean diameter of TiNPs is calculated to be 18.9 nm with a standard deviation of ± 1 nm.

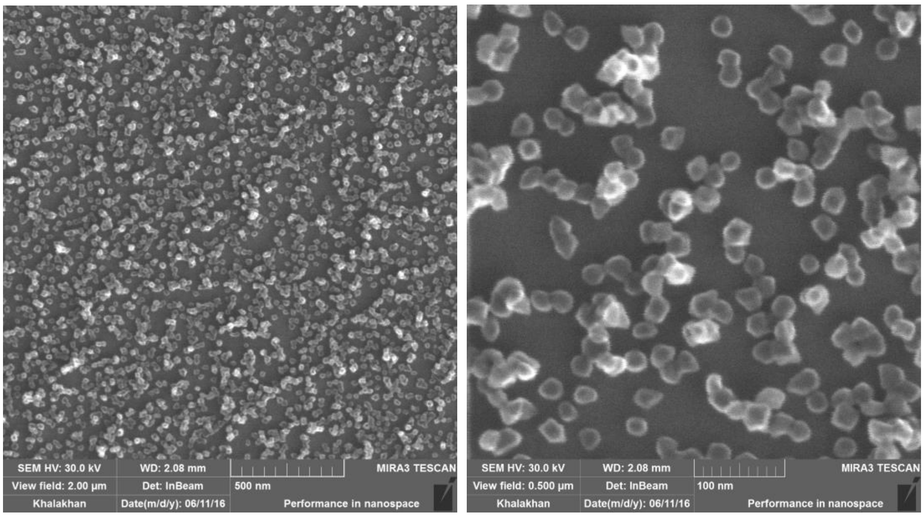

(a) (b)

FIGURE 4.4: SEM images of type 2 substrate where (a) is of low magnification and (b) is of high magnification.

diameter is given in fig. 4.5. On the figure the mean distribution of the particles was calculated to be 20.3 nm with a corresponding standard deviation of ± 1 nm. The deviation in the shape of the histogram plot shown is due to the amount of particles that were chosen for the analysis. Where in this case they were fewer to choose from due to a large number of aggregates as seen in fig. 4.4(b).

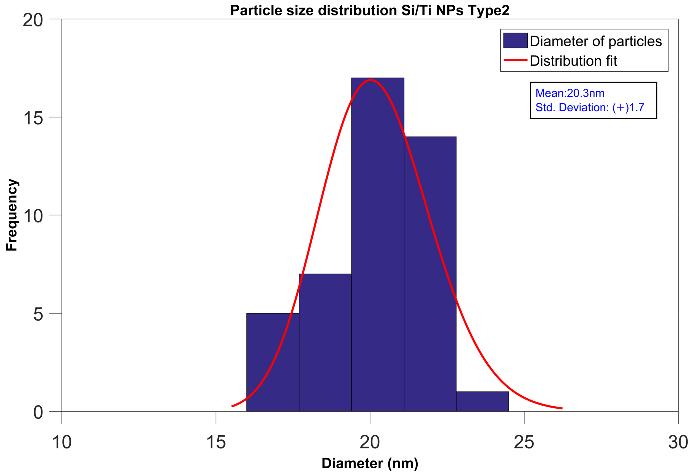

Figure 4.5: The diameter distribution of TiNPs on type 2 substrate shown in fig. 4.4. Where the TiNPs were oxidized after deposition. The mean diameter of TiNPs is calculated to be 20.3 nm with a standard deviation of ± 1 nm.

Type 3 substrates were also characterized using SEM, where the images produced can be seen in fig. 4.6. When examining the fig. 4.6(a) there is a larger number of cluster aggregates that formed during deposition due to in-flight oxidation, nonetheless the surface coverage of TiNPs is similar in the other types of substrates figs. 4.2 and 4.4. When examining the image even closer, as seen in fig. 4.6(b), the TiNPs seem to have retained their spherical/circular shape after deposition onto the surface which was not the case in figs. 4.2(b) and 4.4(b). However as seen there are larger aggregates that formed during the deposition process.

Once again using the high magnification image, fig. 4.6(b), the size distribution of the type 3 TiNPs could be estimated. The size distribution showing the diameter of the particles calculated as a function of the area can be seen in fig. 4.7. For these particles the mean diameter of the TiNPs was found to be 21.4 nm with a corresponding standard deviation of ± 1 nm. The histogram appears different than the case in fig. 4.5 due to the fewer

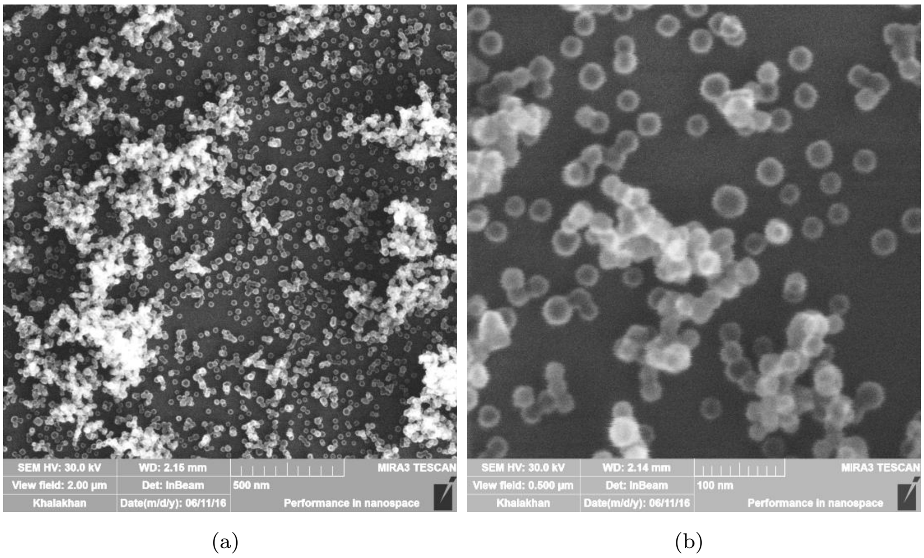

(a) (b)

FIGURE 4.6: SEM images of type 3 substrate where (a) is of low magnification and (b) is of high magnification.

number of particles chosen for the statistical analysis. The tail observed in the figure is due to larger particles measured that occur at lower counts.

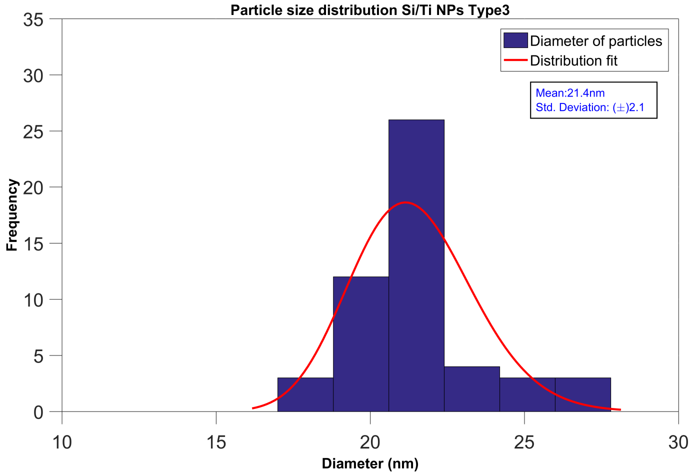

FIGURE 4.7: The diameter distribution of TiNPs on type 3 substrate shown in fig. 4.6. The mean diameter of TiNPs is calculated to be 20.4 nm with a standard deviation of ± 1 nm.

Lastly when comparing the TiNP that were deposited unto substrate with or without PS film as shown in fig. 4.8, where fig. 4.8(a) is TiNPs on bare silicon and fig. 4.8(b) is TiNPs embedded in PS film. There is no direct difference in the morphology of the TiNPs.

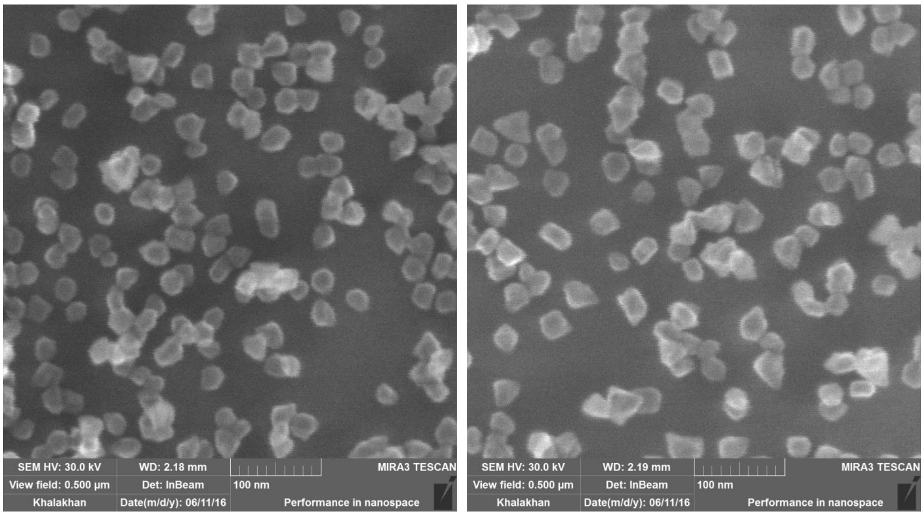

(a) (b)

FIGURE 4.8: SEM images comparing the TiNP where (a) is TiNPs on bare silicon and (b) shows TiNPs deposited on PS film.

In addition when comparing the size distribution as seen in fig. 4.9 apart from a slight deviation in the particle size; 20 nm for TiNPs on bare SI and 21.1 nm for those on substrates with PS film, then there is no difference between the two substrates. That is there is no effect of substrate on the size of the TiNPs deposited. The difference in the histogram arises due to the number of particles taken into consideration during the analysis of the size distribution.

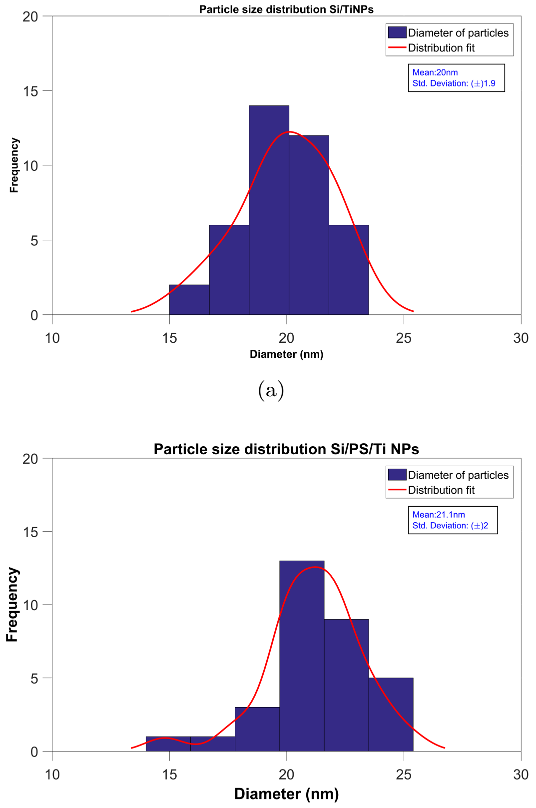

(a)

(b)

FIGURE 4.9: Comparison of diameter distribution for TiNPs deposited onto bare Si (a) and those TiNPs deposited on PS film (b). In the former case the diameter is20 nm with a standard deviation and in the latter case the diameter is 21.1 nm, both with a standard deviation of ± 1 nm

4.1.2 Atomic Force Microscopy Images of Copper Metal Composites

The Cu NPs polymer nanocomposites prepared in house where investigated using AFM prior any antibacterial experiments were performed. Cu NPs were produced by Magnetron sputtering as described previously in chapter 3.

The image shown in fig. 4.10(a) depicts Cu_n clusters that were produced using a QMS voltage of $U_Q = \pm$ 500 V deposited for a total of 20 mins. In addition, their corresponding height analysis, fig. 4.10(b), is also included. As can be seen in fig. 4.10(a) there is a significant amount of clusters on the surface with evidence of a few monolayers as shown from the height scale bar on the AFM image, as well as the wide distribution on the height analysis. The corresponding height analysis produced using the matlab [119] shows the height of this multi-layer film to be 33.6 nm with a standard deviation of ± 6 nm as seen in fig. 4.10(b). The QMS voltage applied for this deposition should have produced clusters in the size regime of 21 nm.

The samples were then annealed for 1 and later 3 mins at 120 °C. The annealing temperature is above the glass transition temperature for PS in order to facilitate the embedding of the particles by making the polymer chains more flexible. The effect of annealing can then be seen in the figures figs. 4.11(a) and 4.12(a) where the corresponding height analysisfig. 4.11(b) shows that for 1 min annealing the mean height has decreased from 31.8 nm to 28.1 nm. Similarly the mean height is also affected for the samples annealed for 3 min at 120 °C, fig. 4.12(b), where the mean height has decreased even further to 21.8 nm. This additional decrease in height shows that the particles are embedded even deeper into the polymer film. Furthermore as can be seen in fig. 4.12(b), the annealing of the samples resulted in the distribution starting from much smaller values that were not detected prior annealing due to the presence of larger clusters.

These annealing tests were carried out to show the embedding of the Cu NP into the particle and were also used as a reference for how long the sample to be used for antibacterial tests should be annealed. From the height analysis the 1 min annealing was then chosen for subsequent annealing of sample 6 prior bactericidal tests.

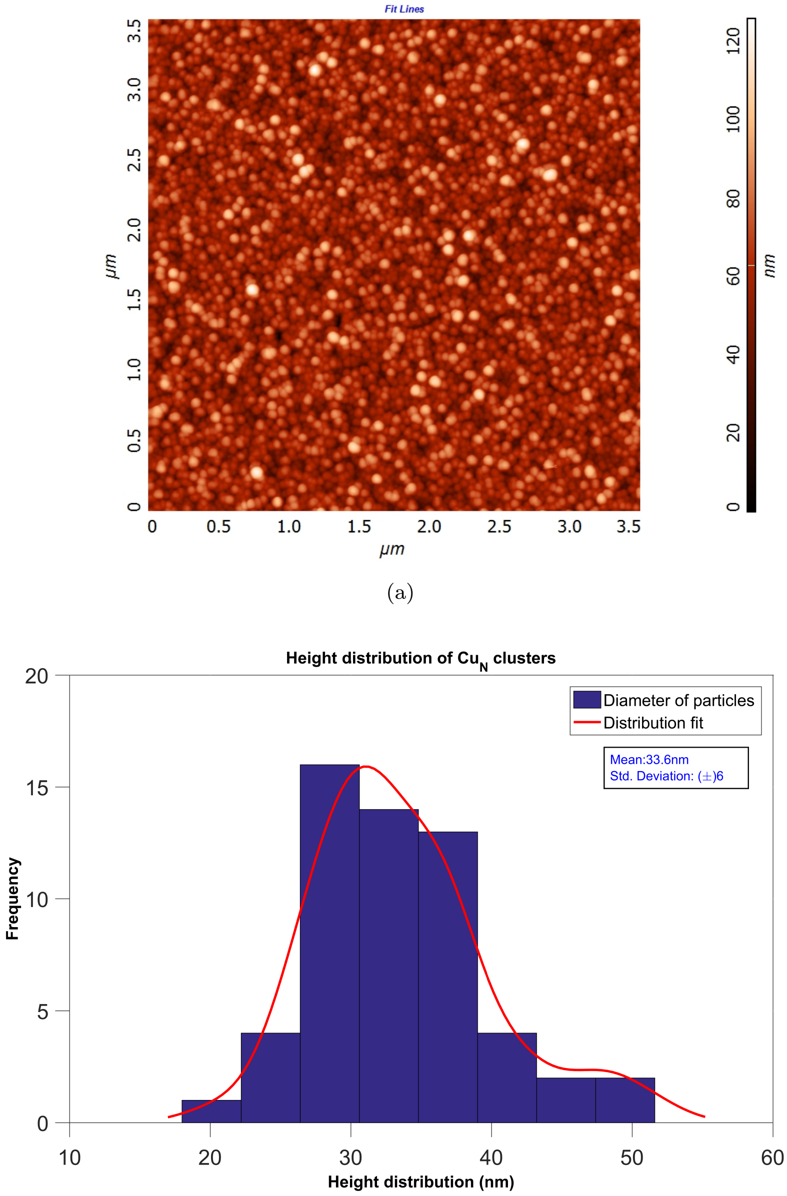

(a)

(b)

Figure 4.10: 3.5 µm by 3.5 µm AFM scan of sample 5 that was taken for Cu NPs deposited onto Si spun with 50 nm PS can be seen in (a) and the corresponding height distribution for the cluster film is given in (b).

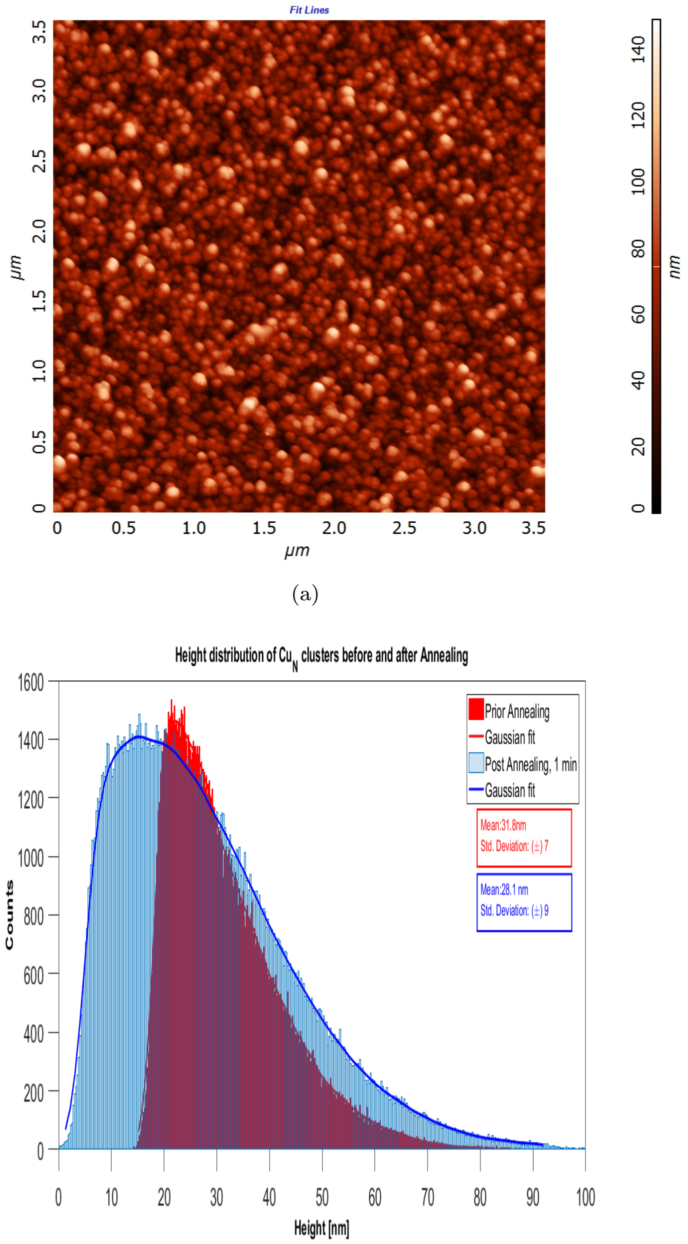

(a)

(b)

Figure 4.11: The Second AFM scan of sample 5, fig. 4.12 and the corresponding height distribution, following annealing at 120 °C for 1 min. The Cu NPs film is found to have a height of 28.1 nm ± 9 nm after annealing.

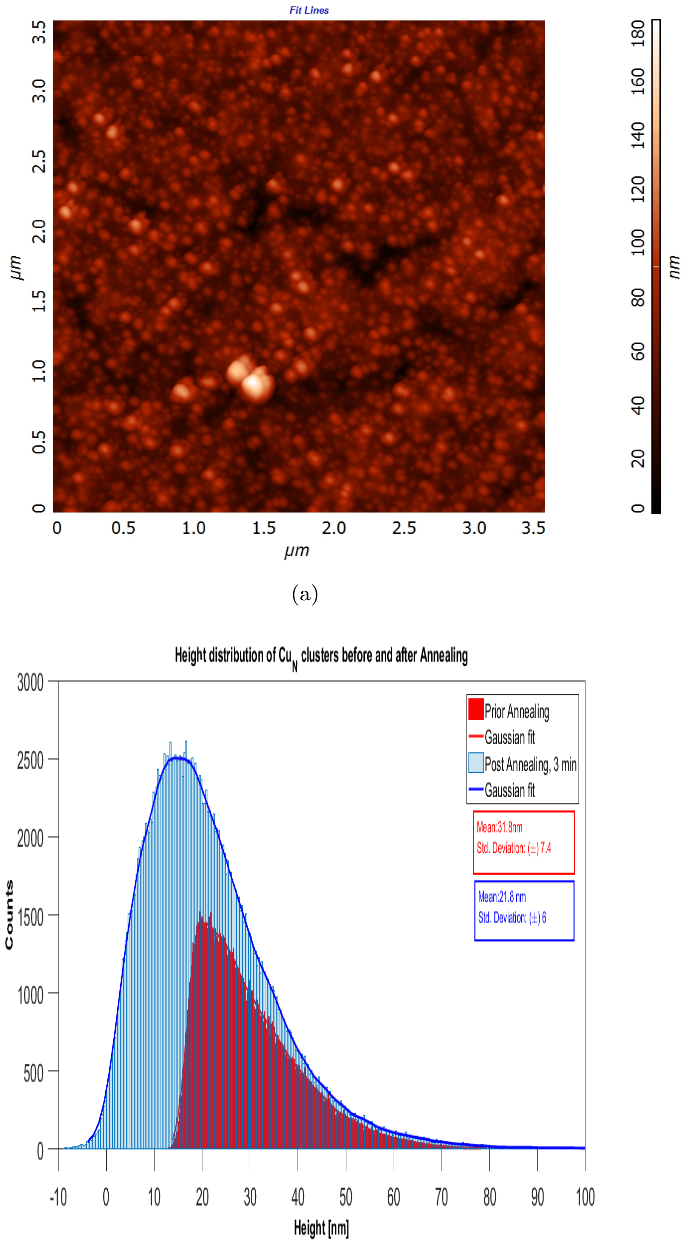

(a)

(b)

Figure 4.12: The third AFM scan of sample 5 fig. 4.12 and the corresponding height distribution, following annealing at 120 °C for 3 mins. The Cu NPs film is found to have a height of 21.1 nm ± 6 nm

4.1.3 Investigation of Copper clusters embedment using optical microscopy

Optic measurements were also carried out on Cu NP deposited on quartz substrates (sample 1 to 4) to investigate the embedding of clusters into the prepared polymer nanocomposities.

The extinction spectra shown in fig. 4.13, is that of the prepared samples before annealing was carried out. All samples show a LSPR peak in the range of 580 nm for Cu_n clusters. The sample was then annealed for 1 min at 120 °C to facilitate embedding. As can be seen in figure fig. 4.14 the relative extinction significantly increases from 12% to close to 20 %. The change in plasmonic properties is evident of the clusters being embedded in a medium that has a higher dielectric constant than air, where in this case they are embedded in PS (ϵ ;2.5-2.9). Afm images of the same sample were also taken in order to show whether or not the clusters did become embedded and can be seen in the fig. 4.15 and fig. 4.16 with the corresponding height distribution in fig. 4.17. As a result of their embedding, the extinction as well as the LSPR peak position changes due to the higher dielectric constant of PS, as depicted in the equation eq. (2.8) in section 2.2.1.

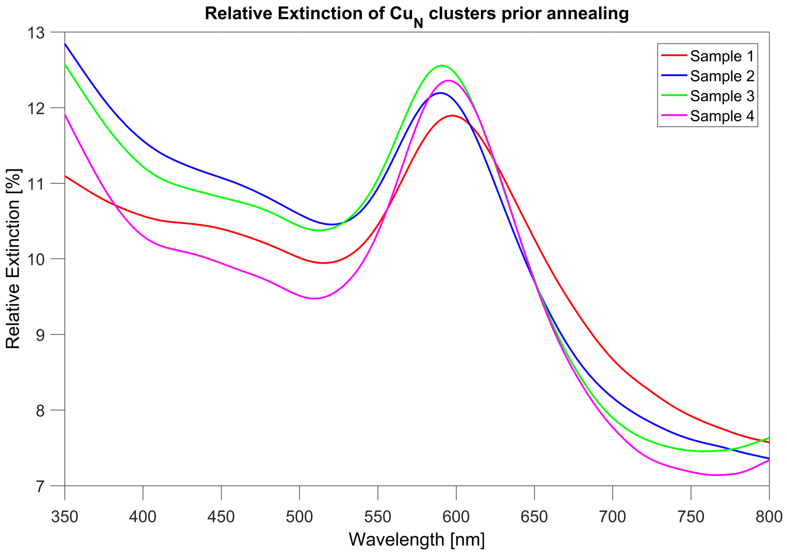

FIGURE 4.13: Cu NPs extinction spectra of sample 4 before annealing.

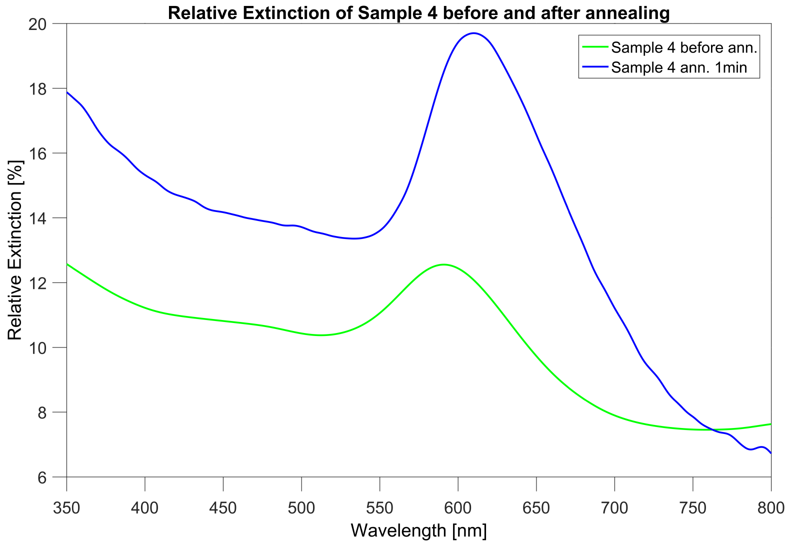

FIGURE 4.14: Cu NP Extinction spectra for sample 4 before annealing and after annealing at 1 min.

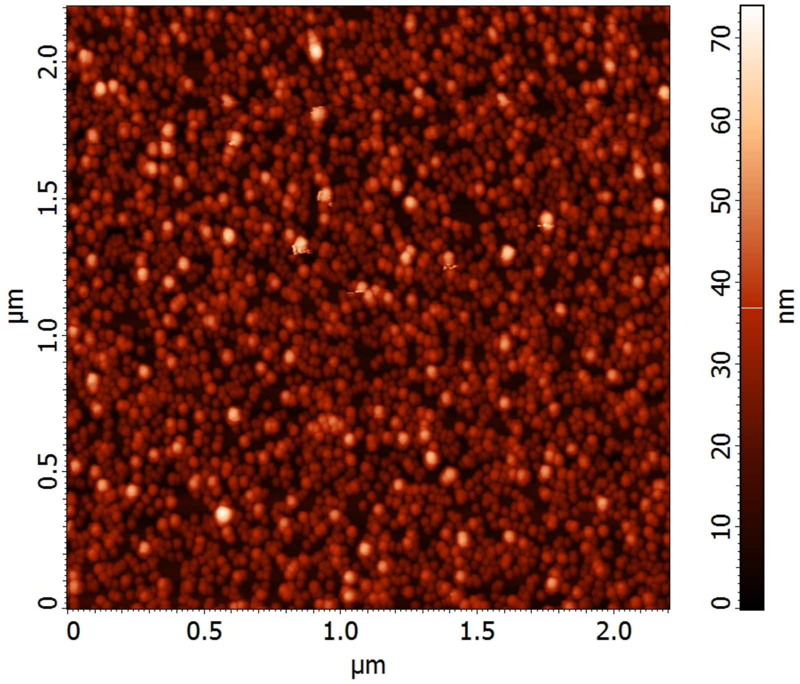

FIGURE 4.15: Afm image of sample 4 prior annealing.

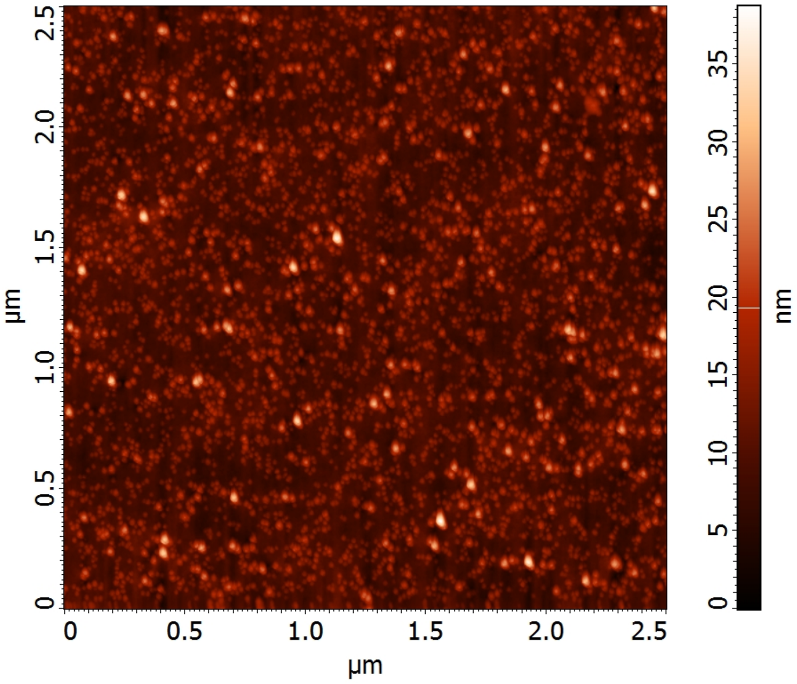

FIGURE 4.16: Afm image of sample 4 after annealing.

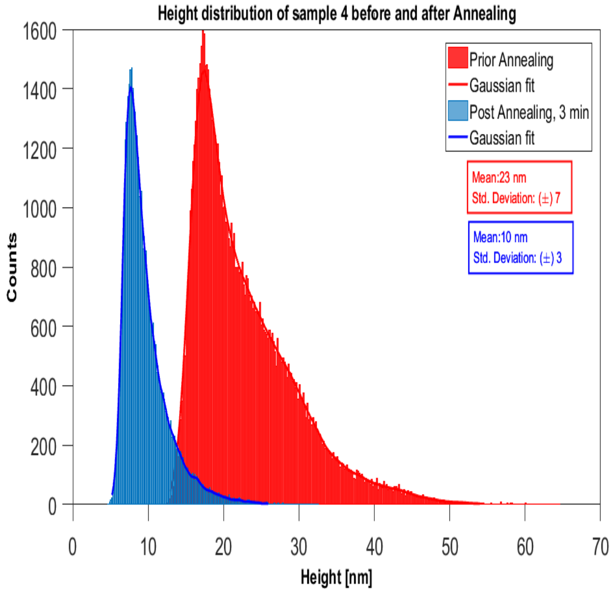

FIGURE 4.17: Corresponding height analysis before and after annealing of sample 4.

4.2 Investigation of Antibacterial aspects of prepared Nanocomposities on *E.coli*

For the bacterial assays, the growth curve for E.coli was first determined as described in section section 3.2.2, where the OD was measured periodically every 20 mins in order to obtain the growth curve displayed in figure 4.18. Furthermore after carrying the dilution series and measuring the OD as described in section 3.2.2 the appropriate dilution (1:10^5) was used to obtain the number of cells in the inoculum and used to plot the OD vs. cell number as shown in fig. 4.19. The following images were generated using MATLAB R2016a [119].

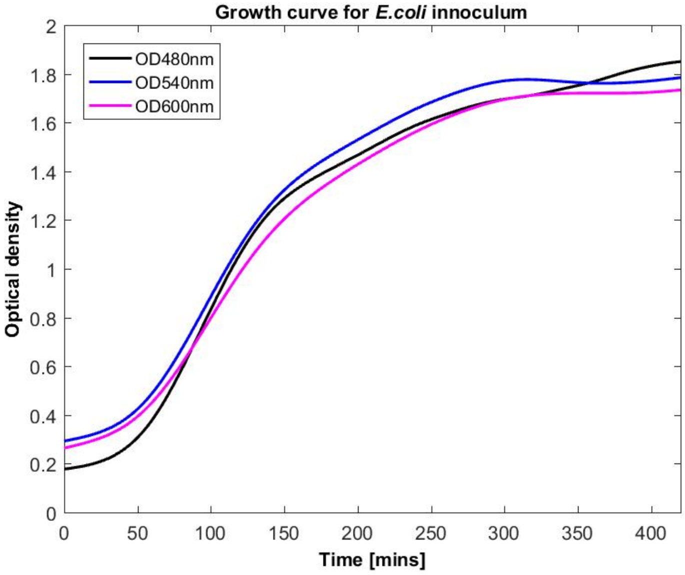

FIGURE 4.18: The growth curve of the *E.coli* inoculum that was used for the serial dilution in order to plate the 1:10^5 dilution for comparison of OD vs. cell number. The OD was measured at the various wavelengths indicated; OD_{480nm}, OD_{540nm} and OD_{600nm}

In order to obtain the cell number for the 1:10^5 dilution the procedure mentioned in section 3.2.3 was carried out. The fig. 4.19 is then used to estimate the cell number of forthcoming experiments by measuring the OD of a particular *E.coli* inoculum. . The following images were generated using MATLAB R2016a [119].

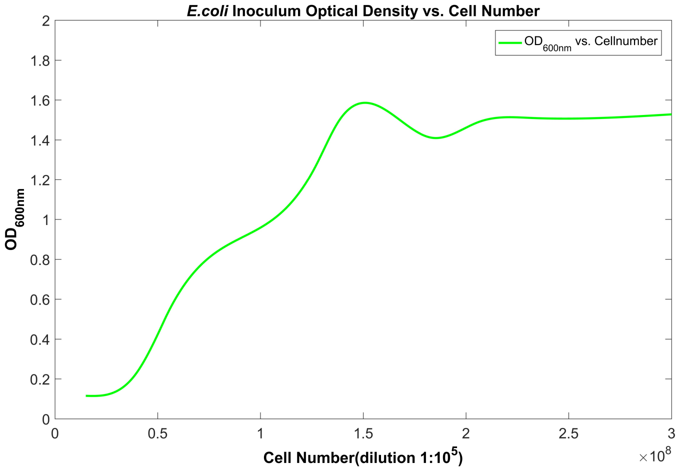

FIGURE 4.19: The 1:10^5 serial dilution comparison of OD vs. cell number. Where number of cells was estimated using the ImageJ software and the graph obtained using MATLAB R2016a

4.2.1 Effect of titania nanocomposites on *E.coli* growth

Prior to any antibacterial test a culture of bacteria is prepared as described in section 3.3.1. Once the inoculum is prepared and diluted, a volume of 200 µL is extracted and deposited on the different substrates. The distance between the UV lamp and the sample surface is 30 cm and is kept constant throughout the experiment. Furthermore in order to take into account the bactericidal effect of the UV lamp itself, the tests were conducted using titanium coated samples and uncoated reference samples to avoid any false positive results. Two of each substrate (Type 1-3) are used where one is used as the control(unexposed to UV) and the other is exposed to illumination by a fluorescent UVA lamp(λ = 320-380 nm) fig. 3.7. The substrates used for the antibacterial experiments are all annealed for 5 mins at 120 °C in order to embed the TiO_2 NPs into the polymer.

Once deposited the bacterial solution are left on for 1, 5, 10, 20 and 120 mins before 50 µL is extracted and spread on to already prepared agar plates. The results obtained after plating the bacterial solutions for over night and counting the number of viable cells are represented in the following figs. 4.20 and 4.22 to 4.24

In fig. 4.20, the effect of the type 1 TiNPs deposited on bare Si against *E.coli* can be seen. For this substrate the TiNPs were not treated during/after deposition. From fig. 4.20 one can observe a decrease in the number of viable cells for the control substrate(TiNP no UV) without any UV illumination(control). The number of viable cells for the control is initially 667 which slightly decreases after 5 mins (to 584) and even further to 540 cells after 20 mins. When the substrate is irradiated with UV for a minute, the cell number decreases from 667 (initial control value) to 422(TiO_2 NPwith UV). The cell number then decreases further after 10 minutes of illumination from 584(control) to 267(TiO_2 NPwith UV). Lastly upon further photo-activation, the cell number decreases from 540 to 228. Overall after 20 minutes of illumination the viable cell number decreases to 228 from an initial number of 667 cells (at 0 mins) signifying a decrease of 34% in cell viability.

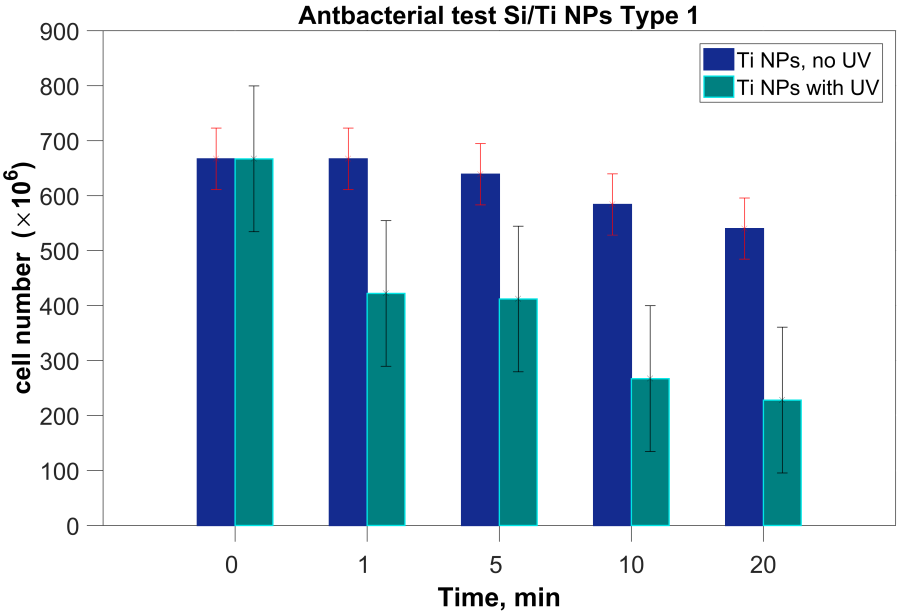

FIGURE 4.20: Type 1 substrate of TiO_2s deposited on bare Si, where the number of cells between the control and UVA sample are compared.

The effect of Type 2 substrates containing TiO_2 NPs deposited on bare Si on *E.coli* is shown in fig. 4.21. For these substrates, type 2, the TiNPs were oxidized after the deposition. For this sample apart from a higher cell density in the beginning there is also a slight decrease in the control cell number which is seen to decrease from 771 to 530 after 20 mins. Similarly as was the case before, the number of viable cells decreases even further after photoactivation of the substrate with UV. It can be seen that after 1 minute of illumination the number of cells decreases from 700(control) to 409 cells. There is an even further decrease after 10 mins. where the cell number has decreased to 314 cells. Lastly after 20 mins. irradiation, the cell number decrease to 282 from a control number of 530 cells. In this case the overall decrease in the number of viable cells for the photoactivated subsbtrate decreases from a control value of 771 signifying a 37% loss in cell viability after 20 mins of UV irradiation.

Upon comparison with the previous graph fig. 4.20 there is a higher density of cells in the beginning, which could be a result of pipetting inconsistencies during plating. The decrease seen in both instances for the control cell number can be a result of the direct contact of bacterial cell with TIO_x nanparticles [121]. Furthermore in both cases upon exposure of the TiO_2 NP to UV the valence band electrons are excited to the conduction band. The electron-hole pair that is formed can then react with the aqueous environment and oxygen in order to generate the ROS responsible for the photo-induced activity of TiO_2 NPs. Upon further exposure more ROS are generated and cause more damage to the cells leading to the significant decrease in viable cells.

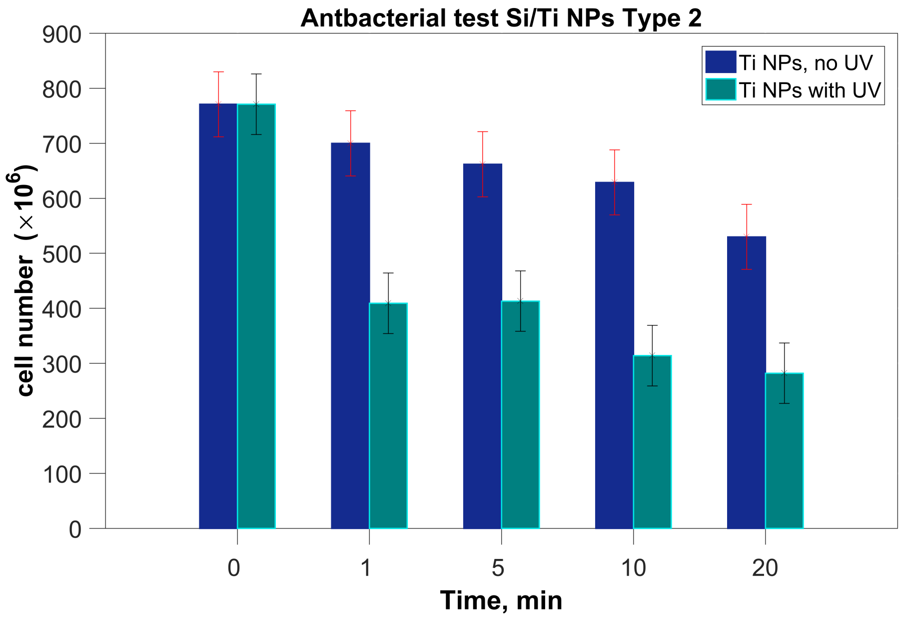

FIGURE 4.21: Comparison of cell number for Type 2 substrate.

For the other substrates,i.e Si with TiNPs embedded in 50 nm PS the samples were first annealed for 5 mins. at 120 °C before any experiments were carried out. A longer exposure time of 120 mins was also implemented to observe any further decrease in E.coli cell number(viable cells). The prolonged exposure time is carried out to test the self-cleansing effect of TiO_2 NP as well as the possible generation of more ROS on cell viability. Furthermore for these substrates the effect of UV on bacteria deposited on bare Si substrate (no TiO_2 NP) was also tested to show the effect of UV itself on *E.coli*.

Upon observing fig. 4.22, there is a slight decrease in viable cells when comparing the Si substrate(with UV) and that of the TiO_2 NP without photo-activation, i.e 443 compared to 440 cells, showing that bacteria cell number is decreased due to direct contact of bacteria with TiO_2 NPs. However this decrease in cell number is even more pronounced after photo-activation of TiO_2 NP with UV, where after 1 min the cell number has dropped to 395.

Furthermore a significant decrease in cell viability is first observed after 20 mins of exposure to UV. At this point the number of viable cells has reduced from 470(control;TiO_2 NP no UV) to 343 (TiO_2 NP with UV). Upon further exposure to UV, the cell number is reduced significantly to 196. There is a 42% drop in the number of viable cells following activation of TiO_2 NPs with UV light when compared to the initial control value of 470 cells. These results further prove that a prolonged exposure time leads to a higher decline in viable cell number.

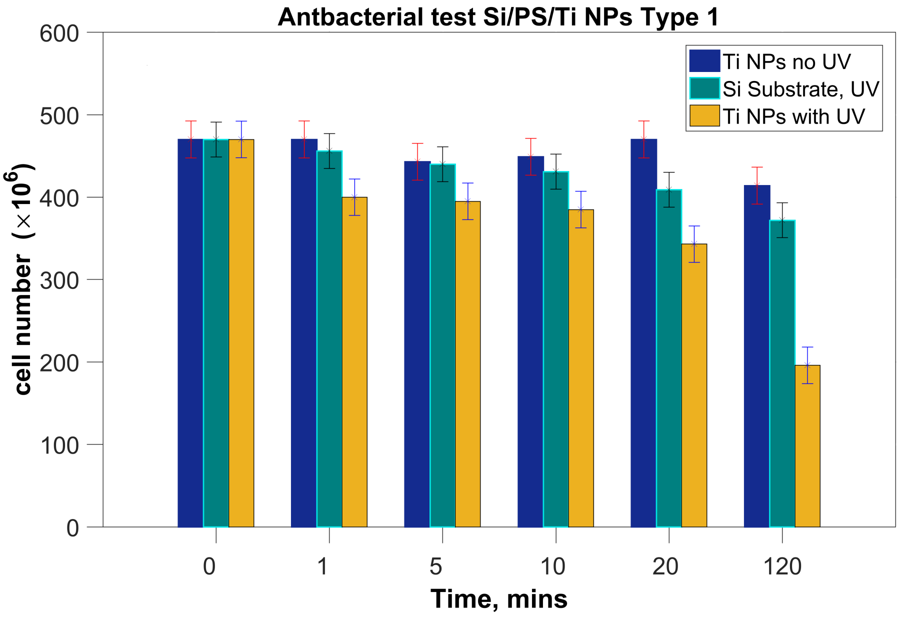

FIGURE 4.22: The bactericidal effect of Si/PS/TiNP type 1 substrate on bacterial viability with and without UV illumination.

In the fig. 4.23, type 2 substrates were used, which also contained TiO_2 NPs embedded in 50 nm PS film on a Si wafer. However for these substrates (Type 2) the TiNPs were treated after deposition with an oxygen plasma. Once again apart from starting with a higher cell number between control samples (468 for type 1 and 486 for type 2) that there is only a slight difference between the control sample(TiO_2 NP no UV), Si with UV and UVA sample(TiO_2 NP with UV) for the times 1, 5 and 10 mins and 20 mins as was observed previously. At these indicated times the decrease in viable cell number for the different substrates remains constant. However as was the case before, a significant drop in cell viability is observed after 120 mins for the photo-activated substrate. At this point the number of viable *E.coli* cells is seen to decrease to 217 cells signifying a 45% drop in the number of viable cells after photo activation of the TiO_2 NP. In comparison to fig. 4.22 there seems to be no effect of treating the TiNPs with oxygen plasma after deposition as the antibacterial effect seems to be similar for these Type 2 substrates.

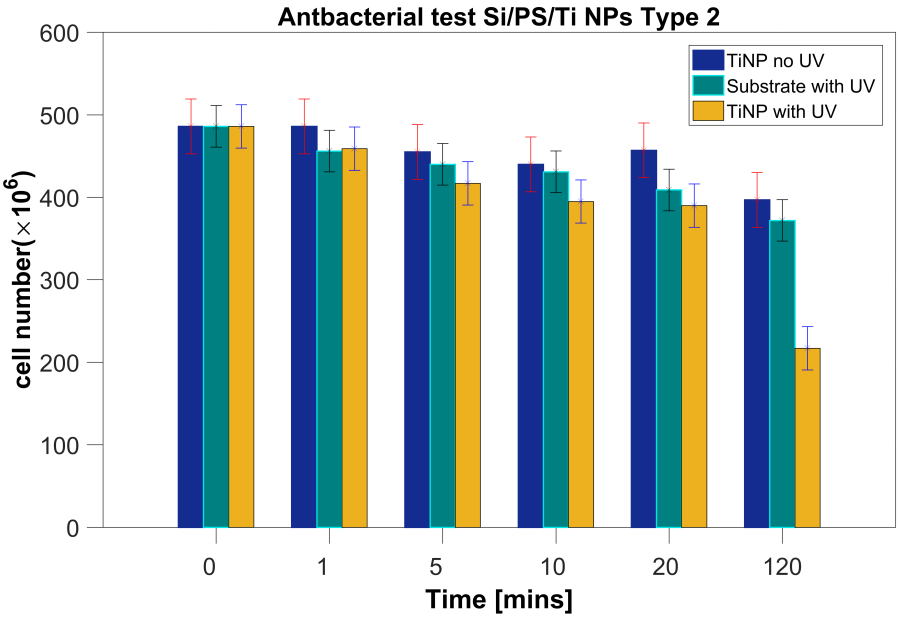

FIGURE 4.23: The bactericidal effect of Si/PS/TiO_x type 2 substrate on bacterial viability.

Lastly In the fig. 4.24, type 3 substrates were used, in which the TiNPs were oxidized in flight before being embedded in the PS film. For this type of substrates, the cell number between control(TiO_2 NP no UV) samples and UV irradiated samples(TiO_2 NP with UV) has already decreased significantly within the first minute of exposure, 445 cells (control) to 281 cells(UV irradiated) and remain constant up to an exposure time of 10 mins. Additionally the number of viable cells then further declines from 440 cells (control) to 217 cells(TiO_2 NP with UV). Once again as was shown for the previous substrates, the number of viable cells drops even further after 120 mins. of exposure. In this case the number of viable cells after 120 mins is 169 cells. When compared to the other substrates, figs. 4.22 and 4.23, the number of viable cells after 20 mins of uv exposure is 217 cells for this substrate. This value is much lower than that for type 1 and type 2 substrates for the same condition; 343 and 390 cells respectively. The same tendency is observed after 120 mins exposure to UV, where for type 3 the number of viable cells is 169 compared to 196(type 1) and 217(type 2) figs. 4.22 and 4.23. Overall the type 3 substrate seems to be more efficient in killing the *E.coli* cells. The in-flight oxidation during the synthesis of this substrate has an effect on the bactericidal nature for these polymer nanocomposites.

In the previous cases figs. 4.22 and 4.23 the low bactericidal effect in the initial stages (1 to 10 mins) can be explained by the preliminary attack of the outer membrane of the *E.coli* cells by the ROSs. At this stage, the bacteria can recover from the damage and re-grow once plated in agar media, meaning that the damage on the outer membrane is insufficient in killing the bacteria as reported by Dunlop *et al.* [122] and Sundua *et al.* [95]. In addition, due to the elongated exposure time (120 mins.) the damage of the outer membrane increases as more ROS are generated and are able to penetrate the bacteria membrane and cause more damage, as is seen by the apparent decrease in viable cells seen in figs. 4.22 to 4.24. Consequently the longer exposure times is then adequate for the photoinduced hydrophilicity to take effect thus removing any layer of dead bacteria, enabling mobility of the generated ROS [86].

Error bars are also included which show the deviation in cell number for the Control samples and UV irradiated samples, these deviations could be due to an error during pipetting as well as during spreading the solutions on the agar plates. The figure and corresponding error bars were generated using MATLAB [119]

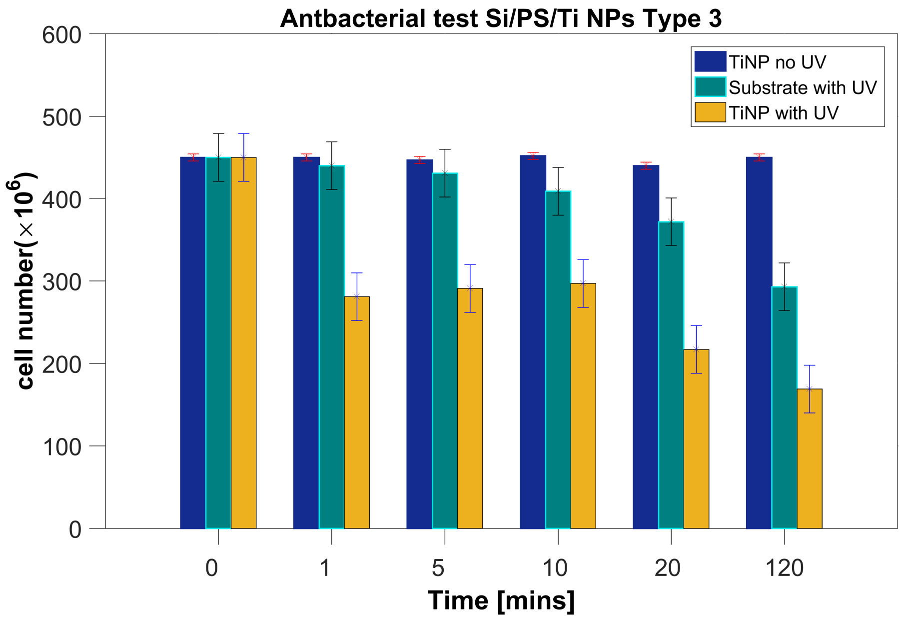

FIGURE 4.24: The bactericidal effect of Si/PS/TiO_x type 3 substrate on bacterial viability.

The antibacterial effects of the TiNPs were tested further by repeating for a total of seven cycles.The graphs for the different TiO_2 NP substrates after the seventh cycle can be observed in fig. 4.25 and ????. For type 1 substrate there is a step-wise decrease in viable cells for the bare Si exposed to UV as bacterial cells are also damaged by UV. For the TiNP that was not photo-activated, the viable cell number does not seem to be affected with a slight change from 513 to 500 nonetheless there is still slight damage to the cells. This however can also be due to pipetting inconsistencies during platting. What is of interest is the decrease in viable cells once the substrate containg TiNP is photo-activated. After the first minute the number of cells is at 364 which then gradually decrease to 292 cells at 120 mins. Furthermore at 180 mins the number of viable cells after the TiNP are photo-activated falls further to 279.

For the type 2 substrate the same tendencies are observed as for type 1 in the seventh cycle. The number of viable cells for the bare substrate with no TiNP decreases in the same fashion as type 1, due to the sole effect of UV radiation. The number of viable cells at the first minute then decreases from 513 cells to 362 once the TiNP are photo-activated as was observed in fig. 4.25 . The number of viable cells then gradually decreases and

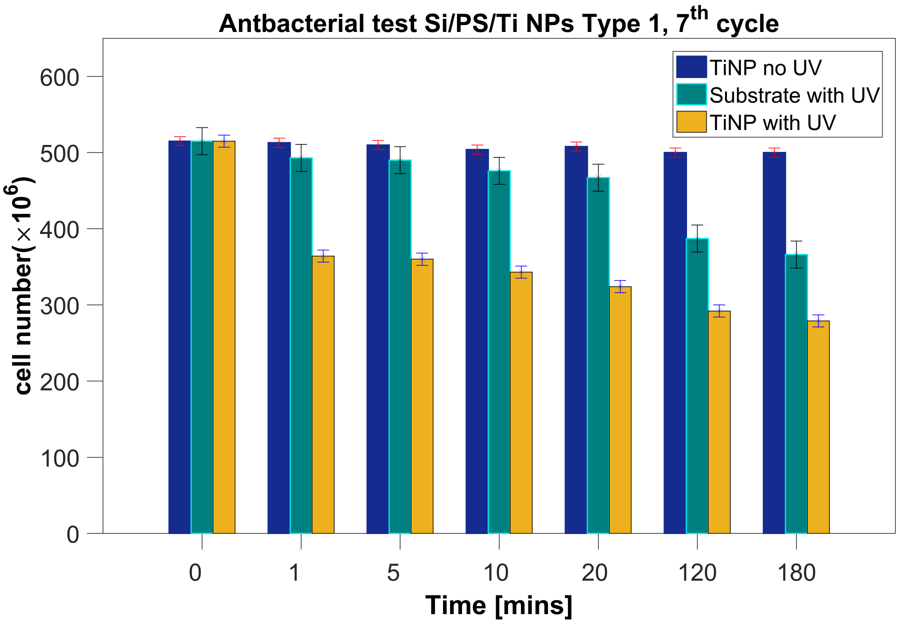

Figure 4.25: The bactericidal effect of Si/PS/TiO_x type 1 substrate on bacterial viability after the seventh cycle.

after 180 mins of exposure to UV the number of viable cells is 275. The decrease in viable cells follows the same pattern as in fig. 4.25, further showing that there was no significant difference between the bactericidal effects of the type 1 and type 2 substrates. Upon comparision of these results to the first cycle fig. 4.22 and ??, there is a better bactericidal efficiency after photo-activation of the substrate for 1 to 20 mins. This is due to the better production of ROS for these substrates after the seventh cycle. For the first cycle, the initial accumulation of ROS until a lethal concentration occurs at a lower rate than in the seventh cycle and therefore leads to a slower decline in viable cell number. However in contrast to the first cycle there are a higher number of viable cells after 120 mins of UV exposure. The reduced bactericidal efficiency for these substrates (type 1 and type 2) after 120 mins can be due to layers of dead bacteria that would hinder the amount of UV light transferred to the TiO_2 NP substrate and consequently affect the production of ROSs.

Similarly the graph for type 3 substrate after the seventh cycle can be observed in fig. 4.27. Once again there is an effect of UV on viable cells deposited on bare si substrate as bacteria are also susceptible to damage by UV irradiation. On the other hand there is no decrease in cell number for the control TiNP substrate (TiNP no UV) . There is a much higher

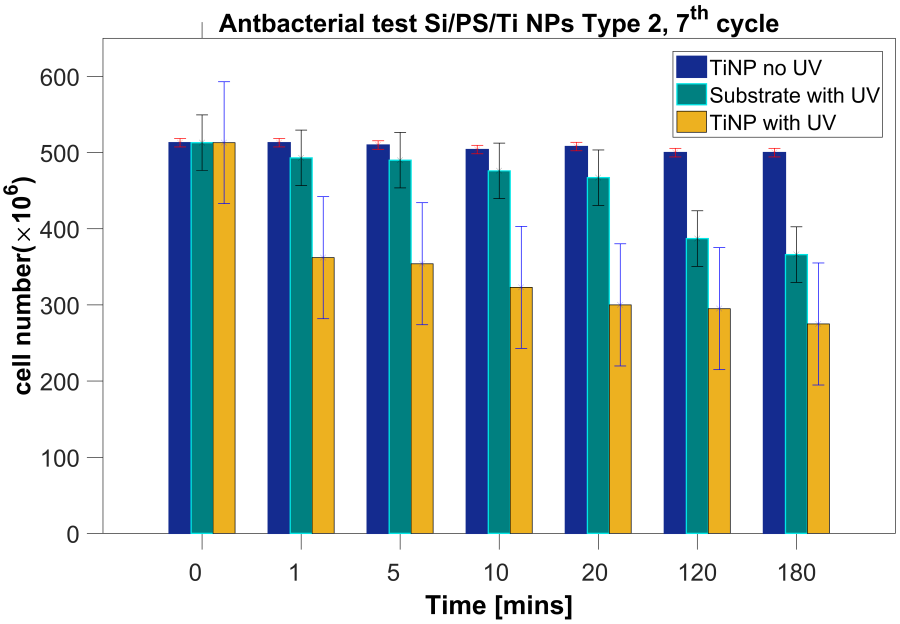

FIGURE 4.26: The bactericidal effect of Si/PS/TiO_x type 2 substrate on bacterial viability after the seventh cycle.

mortality rate for this substrate once photo-activated, as was the case for the first cycle. Within the first minute the number of viable cells is decreased to 243 cells and then gradually decreases even further to 192 cells after 180 mins. For this substrate the amount of ROS produced from the first minute is sufficient to cause a significant decrease in viable cells. The release of ROS from this substrate then remain sufficiently high in order to cause further decline in the number of viable cells after prolonged exposure to UV. The decline in cell number for this substrate after the seventh cycle is more pronounced for 1 to 10 mins than in the first cycle. However after 120 mins the number of viable cells is 200 compared to 169 cells in the first cycle. This could be due to pipetting inconsistencies, error in counting or more probable the accumulation of a layer of bacteria on the TiO_2 NP substrate surface. Nonetheless the bactericidal efficiency for this substrate still remains high given the higher cell density for this cycle (initial number of viable cells is 513 compared to 470 for cycle1). In addition as was the case in the first cycle, this type of substrate is seen to have a greater bactericidal effect when compared to type 1 and type 2 substrates.

The survivability ratio of the bacteria was tested for the different substrates and can be seen in section 4.2.2. Here the number of live cells at the beginning are compared to the

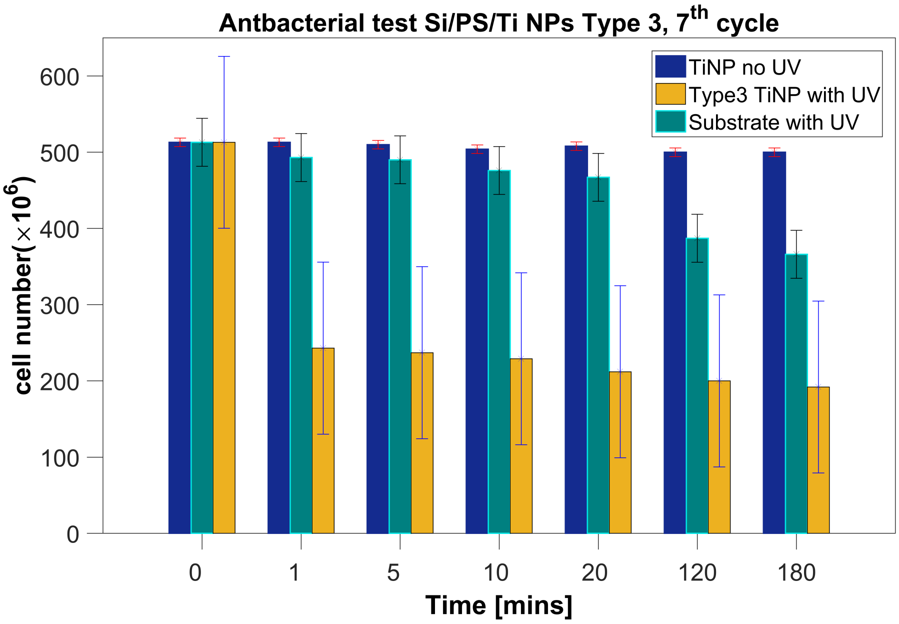

FIGURE 4.27: The bactericidal effect of Si/PS/TiO_x type 3 substrate on bacterial viability after the seventh cycle.

number of live cells after 120 mins. As can be seen in the table, the survivability of cells for type 1 and type 2 are relatively similar. After the first cycle 42% of cells are still alive after 120 mins whereas for type 2 45% are still alive. On the other hand only 37% of the cells are alive for type 3 substrate. The survivability ratio and hence the efficiency for type 1 and 2 then gradually decreases to 57% and 56% for type 1 and 2 respectively after the seventh cycle. For type 3 the survivability ratio is at 39% after the seventh cycle indicating the efficiency of this type of substrate. The production ofROS for this substrate(type 3) over repeated cycles remains sufficiently high in order to kill the bacteria, whereas the other two substrates (type 1 and 2) loose this efficiency over repeated cycles. However, despite the loss in efficiency after 120 mins for type 1 and 2 substrates, the graphs shown in fig:t1c7,fig:t2c7 showed that there was a higher production of ROS for 1 to 20 mins of exposure leading to a faster decline in the number of viable cells.

For the type 3 substrate, there was a higher cell density in the third cycle and the obtained results can be seen in fig. 4.27. Here the higher cell density is seen to affect the reduction of viable cell numbers were presumably not enough ROS are produced to effectively reduce the cell count. Nonetheless, there is still a reduction in cell number within the first

SUBSTRATE	*TYPE 1*	*TYPE 2*	*TYPE 3*
1^{st} *Cycle*	0.42	0.45	0.37
2^{nd} *Cycle*	0.56	0.58	0.24
3^{rd} *Cycle*	0.55	0.56	0.27
4^{th} *Cycle*	0.48	0.45	0.30
5^{th} *Cycle*	0.55	0.60	0.32
6^{th} *Cycle*	0.59	0.56	0.38
7^{th} *Cycle*	0.57	0.56	0.39

TABLE 4.1: Survival Ratio of *E.coli* after 120 minutes tested against the different substrates during various cycles.

minute of exposure where the decline in viable cells then decreases further after 20 mins of exposure. The higher density in comparison to the first cycle fig. 4.24 adversely affect the photocatalytic effect within the first 20 mins. This is likely a result of what is termed 'shadowing-effect' [123] which decreases the light transferred to the TiNP coated surface. This in turn would cause the production of less ROS responsible for the bactericidal effect. However after 120 mins of exposure the cell viability is significantly diminished following increased production of ROS after prolonged exposure of the TiNP coated surface to UV.

The different TiNP coated surfaces used for these test have been shown to have a bactericidal effect especially after activation of these substrates with UV. The photocatalysis is based on the absorption of photons by the crystal structure of the TIO_x species that leads to the transfer of electrons from the conduction band to the valence band. Consequently as a result of this process, free electrons and holes generated react with adsorbed bacteria on the surface. The decomposition of the bacteria then follows from the intermediate production of radicals as a result of the reaction of the e^-/h^+ couple produced by TIO_x NPs which in turn react with the aqueous environment and oxygen to generate ROS. The typical reaction products include superoxide radicals, hydroxyl radicals and hydrogen peroxide that have been shown to induce bacterial lysis [95, 124–128]. According to *kuhn et al.* and *Mitoraj et al.* [126, 129] hydroxyl radicals are the main agent responsible for the bactericidal effect due to their high oxidation potential. As shown by *Muranyi et al.* [123] and increase in relative humidity can aid in the production of more hydroxyl radicals thereby enhancing the bactericidal effect of TiNP polymer compositions. This is the case as hydroxyl radicals arise from the the reaction of the electron hole in the crystal structure with water molecules present in the air [123].

Additionally another positive effect of using TiNP coated surfaces is the formation of the photo-induced super-hydrophilic surface due to metastable hydroxyl groups [130]. This phenomena is characterized by the formation of a thin film liquid layer due to a very small contact angle between the water molecule and the TiO_2 NP film surface. This water film supports the self sterilizing effect of these substrates and enables fast evaporation of the formed film. In doing so the growth of microorganisms can be prohibited as water (essential for microbial growth) is removed. Of interest is the work by *Ohko et al.* [125] were they showed a decrease of *E.coli* viability for TiO_x coated catheter surfaces. They inoculated the surface with 100 µL of $2 * 10^5 CFU ml^{-1}$ and observed a decrease in *E.coli* viability after 60 min exposure to UVA.

4.2.2 Effect of Copper nanocomposites on *E.coli.*

Similarly the effect of the Cu NPs on *E.coli* is also tested and the experiment was carried out as described in section 3.3.2. The antimicrobial effect is tested by depositing a volume of 200 µL on the Cu NP substrate. For these experiments bare Si with no Cu NPs are used for the control substrates. Following exposure to the samples at times ranging from 1 to 180 mins a volume of 50 µL is extracted and spread unto pre-prepared agar plates. The plates are then stored in an incubator and the cells are allowed to grow over night before counting the number of viable cells.

The results obtained for the first cycle are shown in fig. 4.28. The number of viable cells after exposure to Cu NP is seen to drop from 104 cells to 60 cells signifying a 58% drop in viable cells. The number of viable cells after contact with Cu NP remains constant until 10 mins of exposure where it drops to 52 cells. After 20 mins the viable cell count is then decreased to 47 cells before further dropping to 35 cells after 120 mins. As seen from the figure, there is a steady release of copper ions during the contact of bacteria with the Cu NP substrate. This leads to the eventual decline in viable cells as observed in fig. 4.28.

A second test was carried out after washing the substrate with deionized water. Following this 200 µL is deposited on the substrate and the experiment is repeated. The results

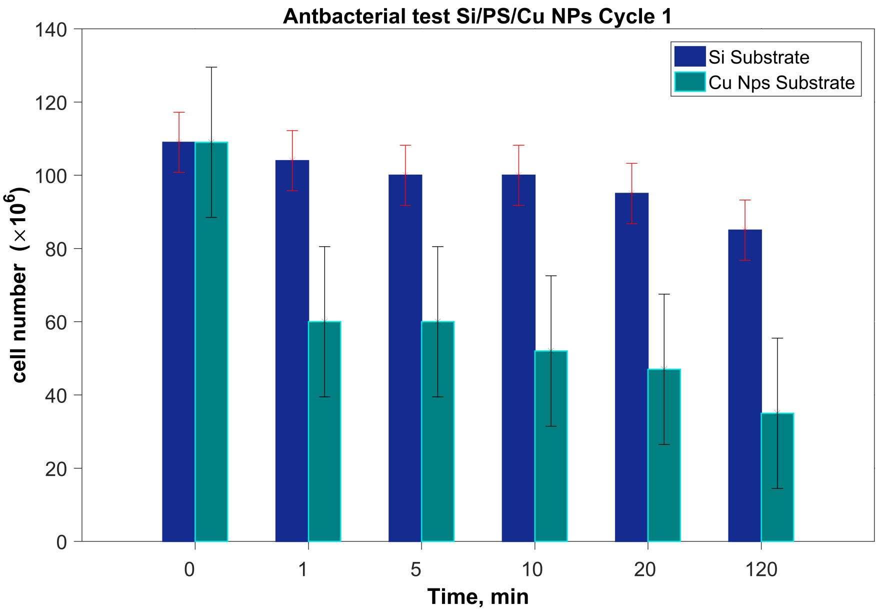

FIGURE 4.28: Graph depicting the viability of the bacterial cells after incubation on Cu NPs in PS compared to deposition on Si without NPs.

obtained in the second cycle can be seen in fig. 4.29.Furthermore a longer exposure time of 180 mins was also tested to quantify any further decrease in cell viability. For this experiment there was a higher cell density with the control number counted to be 227 cells. Unlike in the previous case fig. 4.28, the number of viable cells after 1 min of contact with Cu NP is slightly decreased to 222 cells. A gradual drop in viable cell number is then observed for 5, 10, 20 and 120 mins. For theses indicated times the cell number drops to 189 at 5 mins, 172 at 10 mins, 143 at 20 mins and lastly to 106 at 120 mins following prolonged contact between bacteria and Cu NP. After 180 mins the viable cell number is then decreased to 83 cells following longer contact between the bacterial cells and hence adequate time for the release of copper ions. There is still evidence of bactericidal effect for the Cu NP substrate, however the efficiency is not as dominant as in the first cycle.

Unlike TiO_2 NPs, Cu NPs lack the self cleansing photo-induced mechanism [130].

Further cycles were also carried out as was the case for TiO_2 NP in order to test for the killing efficiency over repeated cycles. For the Cu NP substrtes the third cycle can be seen in fig. 4.30 and the forth cycle in fig. 4.31. The same tendencies are evident in the third cycle as in the second, where there is still a high percentage of viable cells after 1

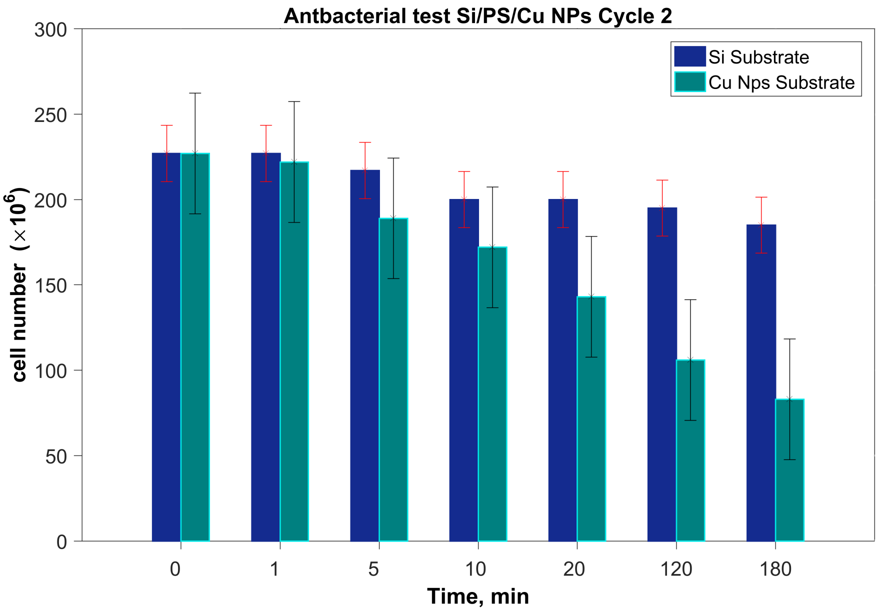

FIGURE 4.29: Graph depicting the viability of the bacterial cells after the second cycle.

min contact with the Cu NP in contrast to the drop observed for the first cycle fig. 4.28. Similarly as in the second cycle, the cell number slightly decreases to 166 cells after 5 mins of contact from 181 cells at 1 min contact. The number of viable cells then remains constant for the other contact times (10-120 mins) before decreasing slightly to 119 cell after 180 mins. In this case after 180 mins the number of viable cells is at 119 compared to 83 in the previous cycle further showing the decline in efficiency for the Cu NP where an even longer exposure time is needed for the bactericidal effect of the Cu NP substrate to manifest. It is clear that there is still a bactericidal effect, however as in the case for the second cycle the efficiency is declining.

In the forth cycle, fig. 4.31, a similar decrease in viable cell number is also observed (from 258 to 218 cells) from the first minute. This value then gradually falls to 174 cells after 120 mins of bacteria and substrate contact. In addition as was in the case for the third cycle, the number of viable cells falls to 119 after 180 mins. Hence as observed for cycle, the number of cells is significantly reduced only after 180 mins as less ions are released from the Cu NP substrate (or released slower) and require longer period of time to have any adverse effect on the bacteria.

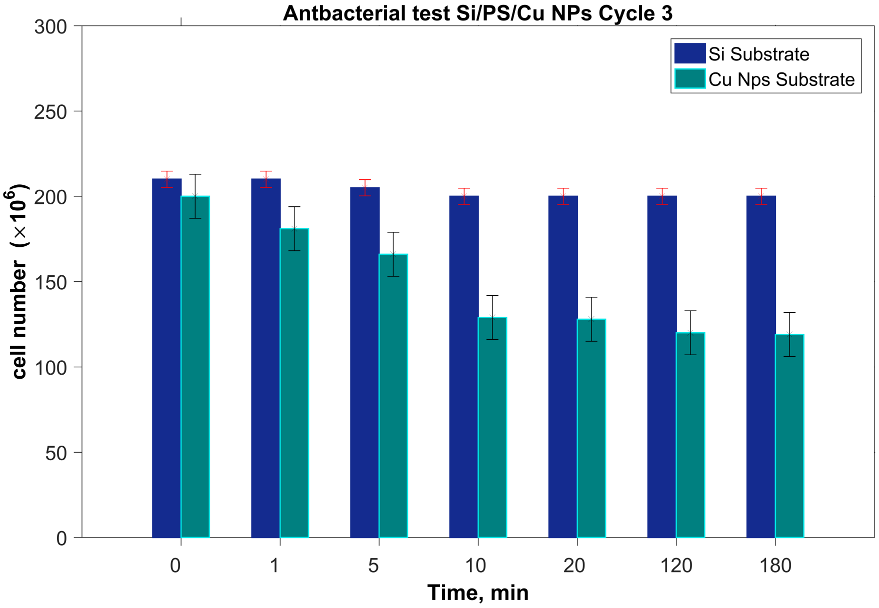

FIGURE 4.30: Graph depicting the viability of the bacterial cells after the third cycle.

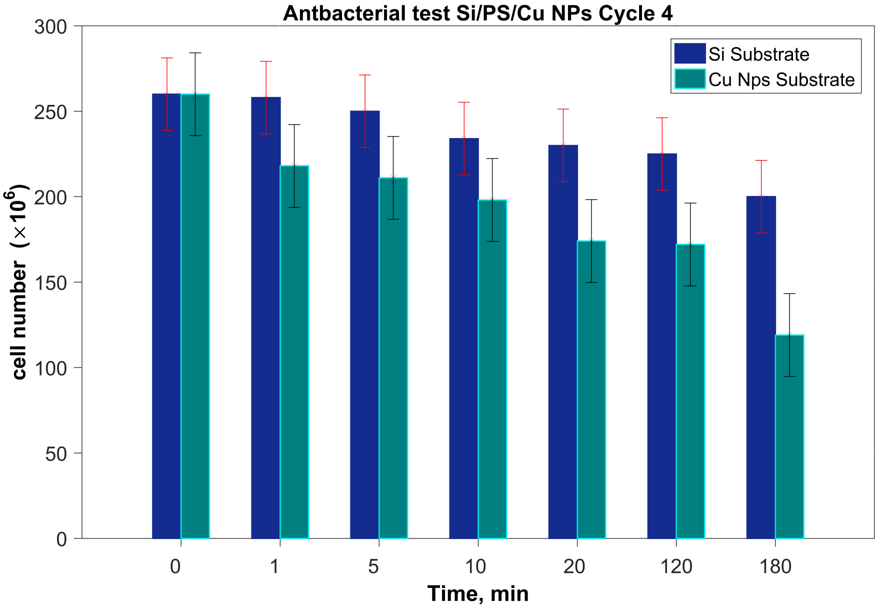

FIGURE 4.31: Graph depicting the viability of the bacterial cells after the fourth cycle.

A table of the survival ratio after 120 mins is also shown in section 4.2.2, where a clear reduction in efficiency is evident as more bacteria are able to survive after 120 mins. As seen in the tabel, 57%, of bacteria are still alive after the third cycle. The efficiency of killing the bacteria further decreases where after the seventh cycle 70% of the bacteria are still alive.

When compared to TiO_2 NP substrates, the killing efficiency is much lower for Cu NP substrates. The TiO_2 NP substrates maintain a better killing efficiency due to the production of ROS and the ability to self sterilize the surface [130]. As observed for the seventh cycle 70% of bacteria are still alive for for Cu NP substrates compared to 57% for type 1, 56% for type 2 and 43% for type 3 TiO_x substrates after the seventh cycle.
The decrease in bactericidal efficiency for the Cu NP polymer nanocomposites could be a consequence of the degradation of Cu NP after subsequent usage during the bactericidal tests. Upon examination of the Cu NP substrate after the first (fig. 4.33(a)) and seventh cycle (fig. 4.33(b)) using AFM, the Cu NPs are still present but agglomerate. A probable cause for the agglomeration is the repeated exposure of the substrates to solutions during the bactericidal experiment and cleansing of the substrate. In addition since the substrates have more than one mono-layer, fig. 4.10(a), the clusters situated at the top layer are more mobile and can therefore form agglomerates as a result of repeated washing and usage. Optical measurements were also carried out, on a different sample (sample 4) to check for any plasmon peak after the antibacterial tests, as seen in fig. 4.32 the plasmon peak is no longer present serving gas a probable indication that the Cu NP have been degraded.

Consequently once the Cu NP become oxidized, copper ions are not released as efficiently and the contact killing efficiency is diminished.

SUBSTRATE	*Cu NPs*
1^{st} *Cycle*	0.32
2^{nd} *Cycle*	0.47
3^{rd} *Cycle*	0.57
4^{th} *Cycle*	0.62
5^{th} *Cycle*	0.63
6^{th} *Cycle*	0.68
7^{th} *Cycle*	0.70

TABLE 4.2: Survival Ratio of *E.coli* after 120 minutes tested against the different substrates during various cycles.

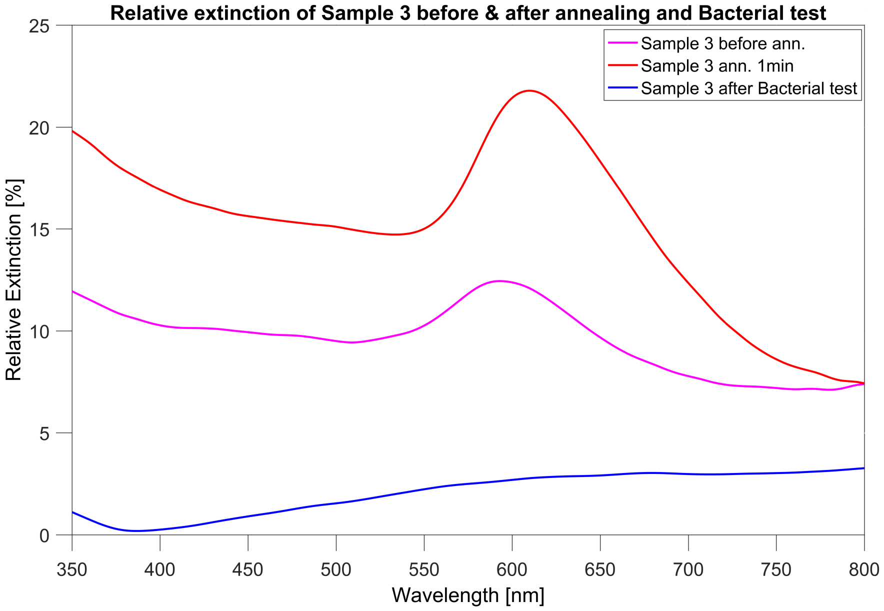

FIGURE 4.32: Cu NP relative extinction of sample 4 after bactericidal tests.

4.3 LIVE/DEAD Baclight and polymer metal composites

As stated previously the LIVE/DEAD Baclight assay was used as an alternative means to investigate the antibacterial effect of the prepared metal polymer nanocomposites.A loss of membrane integrity for the bacteria can be shown as a consequence of Propidium iodide (PI) to penetrate damaged cells as discussed in section 3.4.5. These tests were all carried out after the seven cycles comparing the efficiency of the Cu NP and TiO_2 NP substrates. The procedure for this analysis is given in section 3.4.5. The image shown in fig. 4.34 is that of Live cells on bare Si without any NP showing no effect on cell viability.

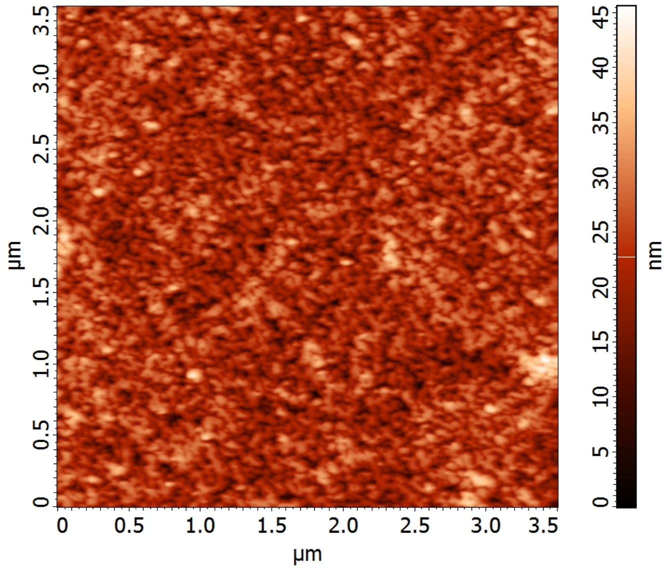

(a)

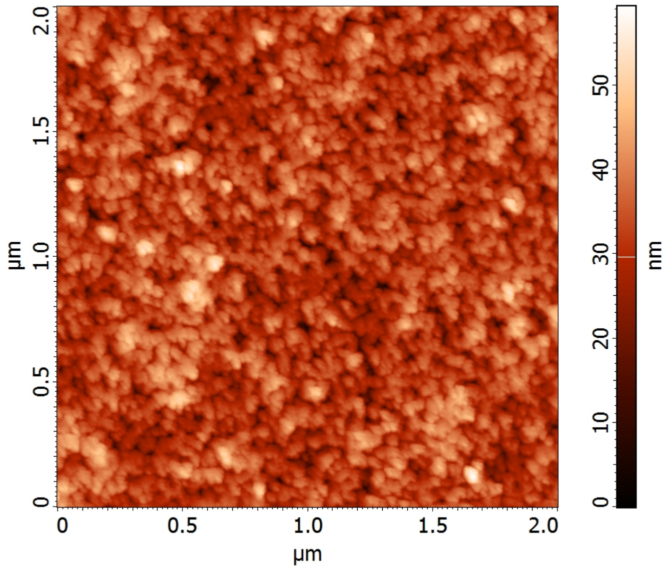

(b)

FIGURE 4.33: AFM images of sample 6 after the first cycle, fig. 4.33(a), and the seventh cyclefig. 4.33(b).

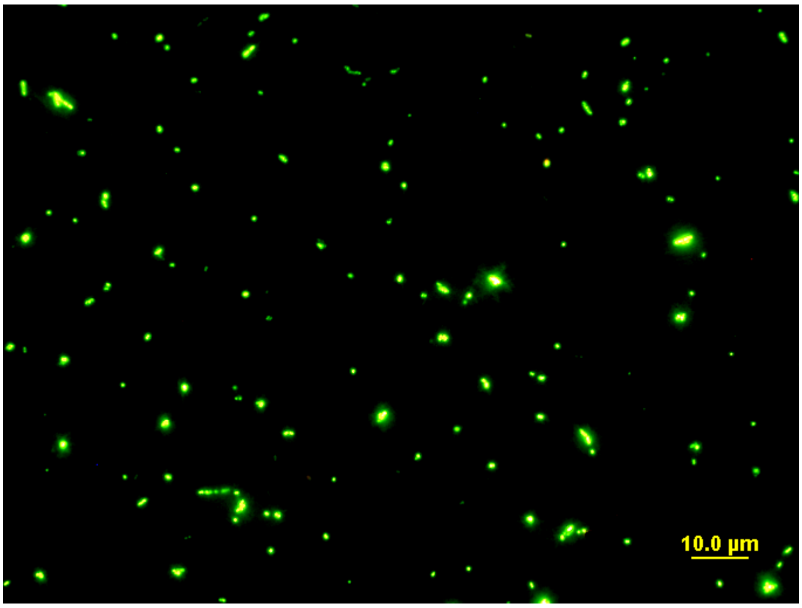

FIGURE 4.34: Live *E.coli* bacterial cells on bare Si substrate.

4.3.1 Fluorescence experiments with TiO_2 NP substrates

Fluorescence images of the live and dead cells after 20 mins exposure to type 2 TiO_2 NP are represented in fig. 4.35 . The number of live cells without any UV illumination is seen in fig. 4.35(a), whereas the number of cells after UV illumination is seen in fig. 4.35(b) whereas the number of dead cells after uv illumination is seen in fig. 4.35(c). Apart from the slight deviation in cell density in fig. 4.35(a) and fig. 4.35(b), there is a greater number of live cells than that of dead cells fig. 4.35(c). This case was also observed in fig. 4.23 with the probable cause being insufficient time for significant damage to the bacterial cells and hence in this case PI cannot bind.

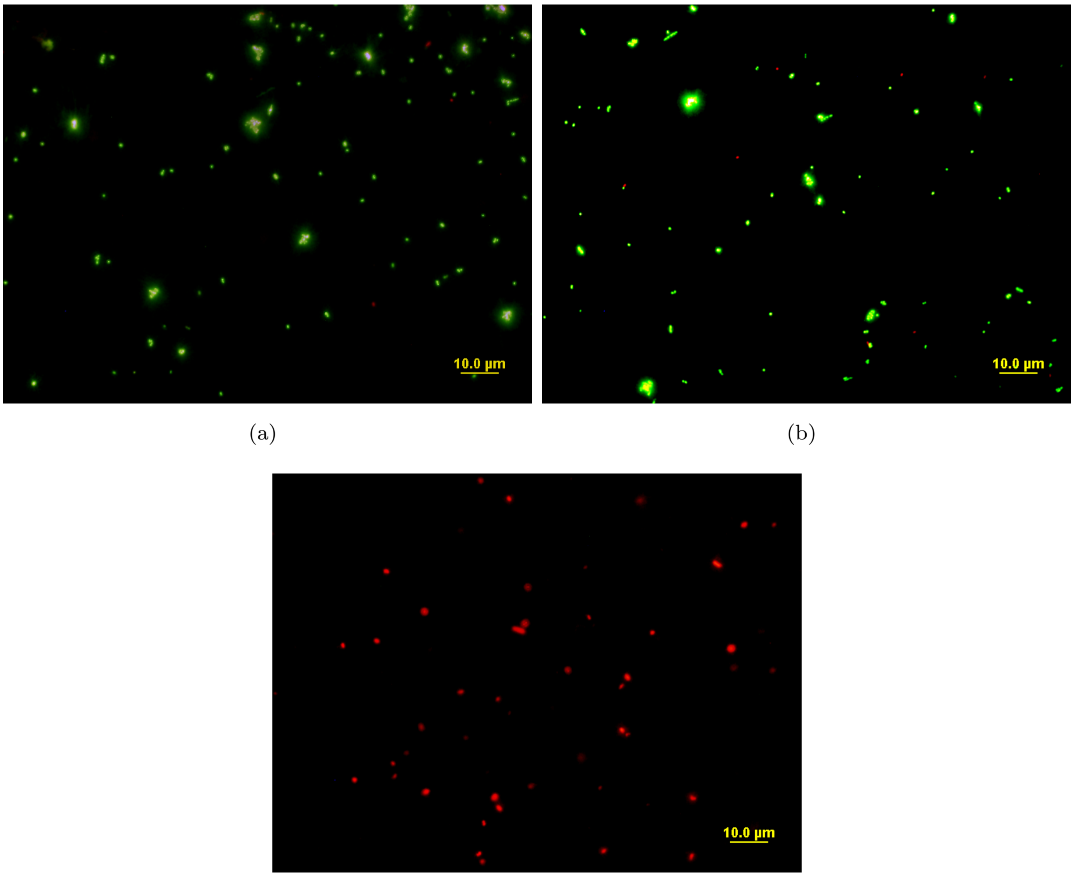

(a) (b)

(c)

FIGURE 4.35: Flourescence images of live and dead cells taken after exposure to type 2 TiNP substrate for a period of 20 mins. Live cells without UV exposure are shown in **??**, live cells after UV exposure in fig. 4.35(b) and dead cells after uv exposure in fig. 4.35(c).

Furthermore as was the case in the efficiency tests, the effect of a longer exposure time to type 2 TiO_2 NPs was also investigated. The fluorescence images are shown in fig. 4.36. Upon comparison of the live cells without UV exposure,fig. 4.36(a), to the live cells exposed to UV fig. 4.36(b) there is a slight decrease in viable cells with the presence of a few dead cells. The effect of UV illumination is more pronounced when observing the number of dead cells seen in, fig. 4.36(c).It is evident that there are higher number of dead cells. When comparing fig. 4.35(c) to fig. 4.36(c) there is an increase in the number of dead cells after 120 mins of UV illumination. This is in accordance to the previous results obtained in fig. 4.23 showing a decrease in viable cells after 120 mins exposure.

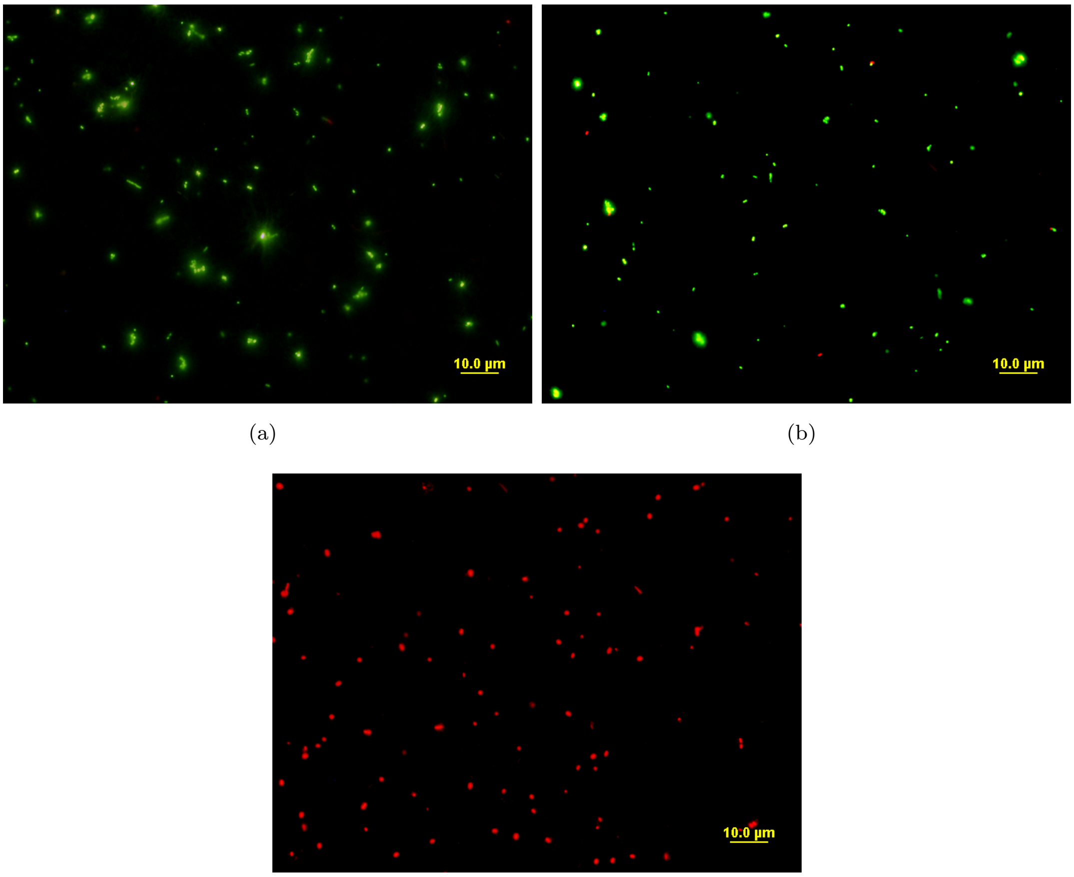

(a) (b)

(c)

FIGURE 4.36: Images shown are those of live and dead cells taken after exposure to type 2 TiNP substrate for a period of 120 mins.

Using the Fluorescence images shown in fig. 4.35 and fig. 4.36, the number of live cells and dead cells were counted and plotted using matlab (codes provided in the appendix) [119]. At first the images were converted from rgb to grey-scale before a binary image is produced and the number of objects displayed for the different images counted.

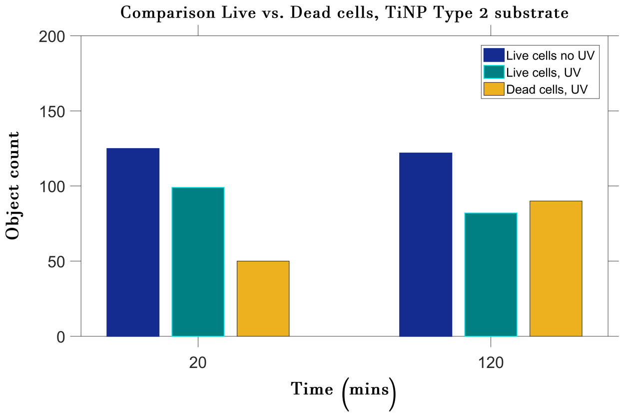

FIGURE 4.37: Plot showing the contrast between live and dead cells from 4.35 and 4.36 after 20 mins and 120 mins exposure for type 2 substrate.

There is a larger decrease in live cells after exposure to UV at a time of 120 min. The number of dead cells after 120 mins exposure is also higher than the case after 20 mins. The number of live cells with UV exposure decreases from 99 (at 20 mins) to 82 after 120 mins UV exposure. On the contrary as observed the number of dead cells increases from 36(20 mins) to 90 after 120 mins of UV illumination.

Type 3 substrates were also tested and the fluorescence images acquired in the same manner. The images in fig. 4.38 represent those obtained after 20 mins of exposure. The number of live cells without any UV illumination is seen in fig. 4.38(a), whereas the number of viable cells after UV illumination is seen in fig. 4.38(b). IN addition the number of dead cells after UV illumination is seen in fig. 4.38(c). There is a decrease in live cell density as seen in fig. 4.38(b)and furthermore there are already a number of dead cells in fig. 4.38(b). In addition the number of dead cells,fig. 4.38(c), is slightly higher than in the case for the type 2 substrates(fig. 4.35(c)) after 20 mins exposure. These results are in parallel to those presented in fig. 4.24 where for this type of substrate there is already a higher decrease of viable cells after 20 mins exposure to UV.

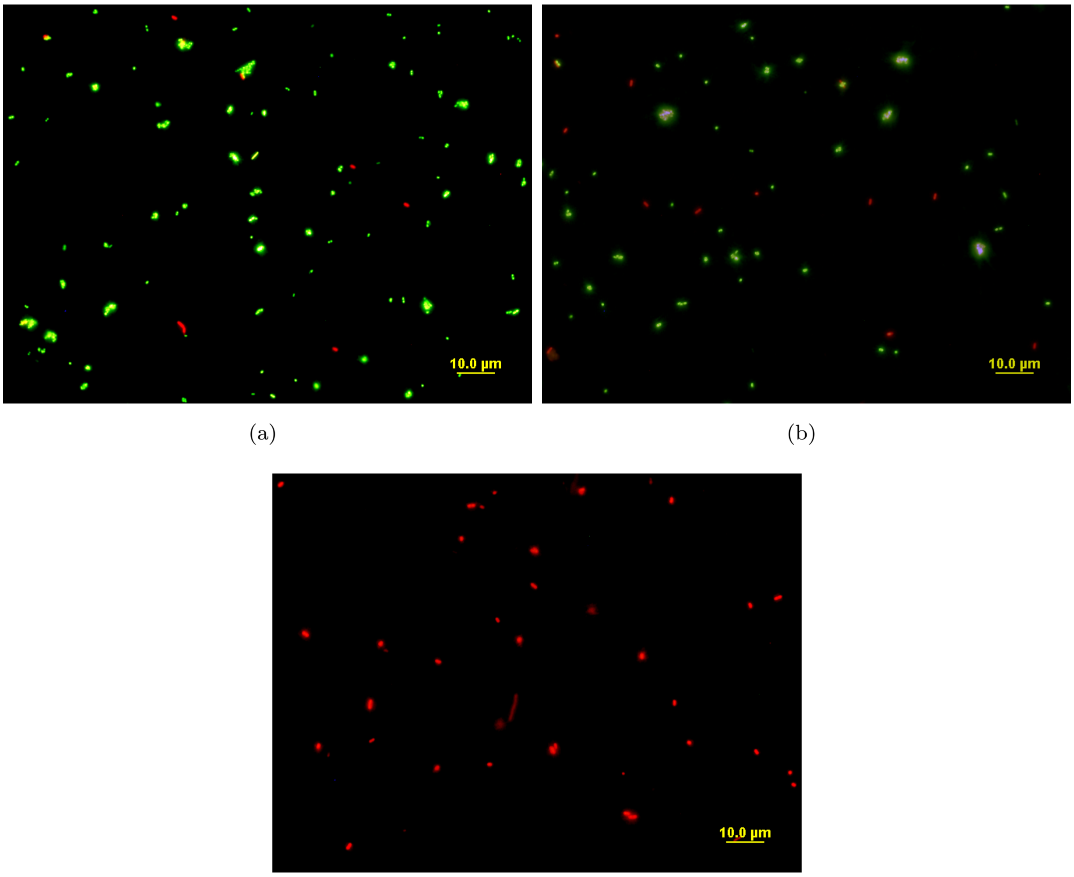

(a)

(b)

(c)

FIGURE 4.38: Images shown are those of live and dead cells taken after exposure to type 3 TiNP substrate for a period of 120 mins.

Similarly the live/dead assay using type 3 substrates was also carried out for 120 mins, and the fluorescence images can be seen in fig. 4.39. The live cells without any UV exposure are seen in fig. 4.39(a) and live cells after UV exposure are seen in fig. 4.39(b). Upon comparison there is a significant decrease in live cells after exposure to UV. Similarly the dead cells after UV exposure,fig. 4.39(c), are greater in number than the live cells. These results for this TiO_2 NP substrates conquer with those presented in section 4.2.1,fig. 4.24 where there is a higher mortality rate for the cells after 120 mins exposure for this substrate compared to both type 1 and 2 substrates.

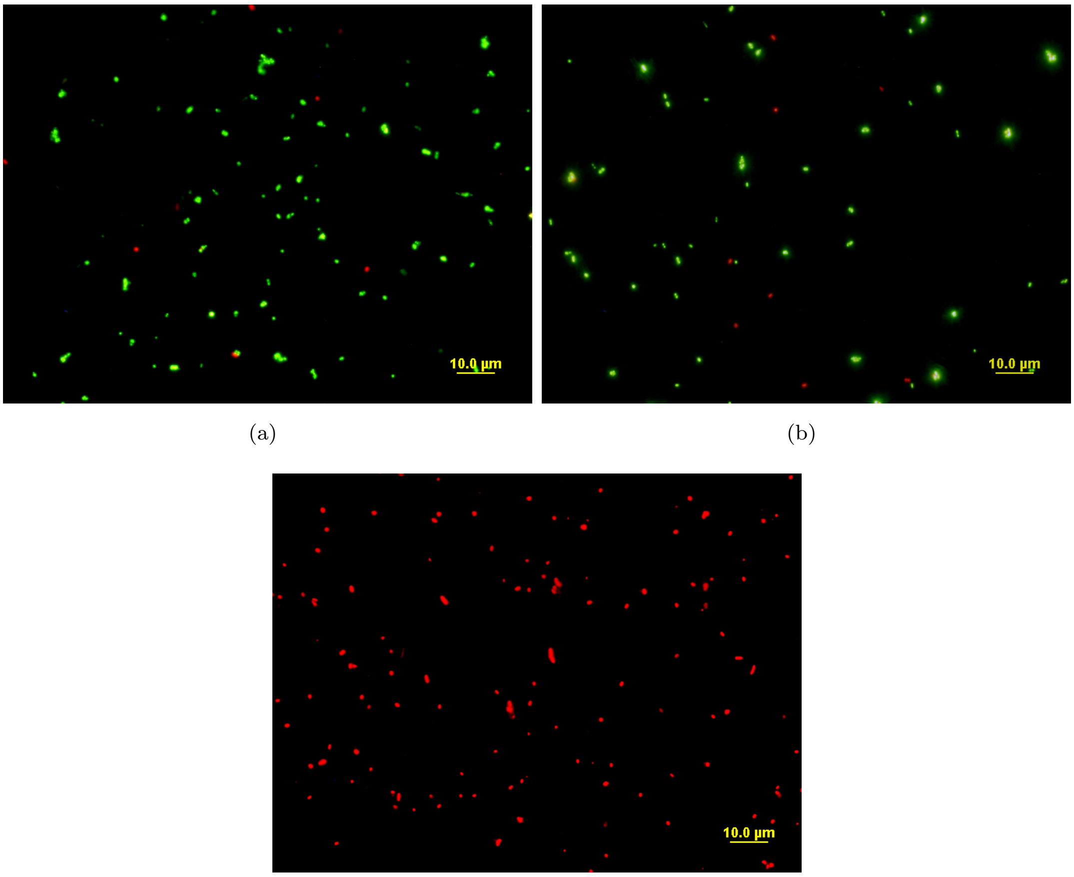

(a) (b)

(c)

FIGURE 4.39: Images shown are those of live and dead cells taken after exposure to type 3 TiNP substrate for a period of 120 mins.

Once again the fluorescence images presented in fig. 4.38 and fig. 4.39 were used to plot the number of live and dead cells and can be seen in 4.40. For this substrate the number of dead cells after 20 mins exposure (50 cells) is already higher than for type 2 substrate (36) after 20 mins exposure. Furthermore the ratio between live and dead cells at 120 mins is also significantly higher when compared to the type 2 substrate, i.e 133 dead cells for type 3 compared to 90 dead cells for type 2. These results for the TiO_2 NP type 3 substrates conquer with those presented in section 4.2.1,fig. 4.24. It was shown that even after repeated cycles thus type of substrate still maintained its bactericidal efficiency, where there is a higher mortality rate for the cells after 120 mins exposure compared to both type 1 and 2 substrates.

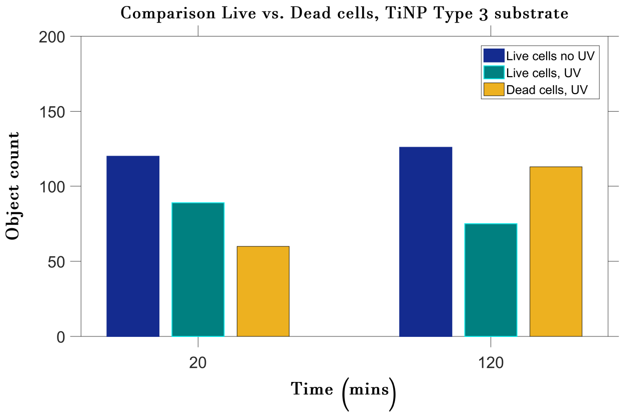

FIGURE 4.40: Plot showing the contrast between live and dead cells from fig. 4.38 and fig. 4.39 after 20 mins and 120 mins exposure to type 3 substrate.

4.3.2 Fluorescence experiments with Cu NP substrates

For comparative reasons the Cu NPs containing substrates were also tested. The images shown in 4.41 are fluorescence images of *E.coli* bacteria stained after 20 mins exposure to Cu NPs. The 4.41(a) is that of live cells in contrast to the image shown in fig. 4.41(b) that is of the dead cells obtained as stated in section 3.4.5. It is seen that there is a greater ratio of live cells as compared to dead cells. These results are in accordance to those presented in section 4.2.2 where the loss in bactericidal efficiency results in a higher number of live cells than dead cells.

In addition a longer exposure time of 120 mins was tested in order to see if the ratio between live and dead cells would change as seen in fig. 4.28 . The fluorescence images

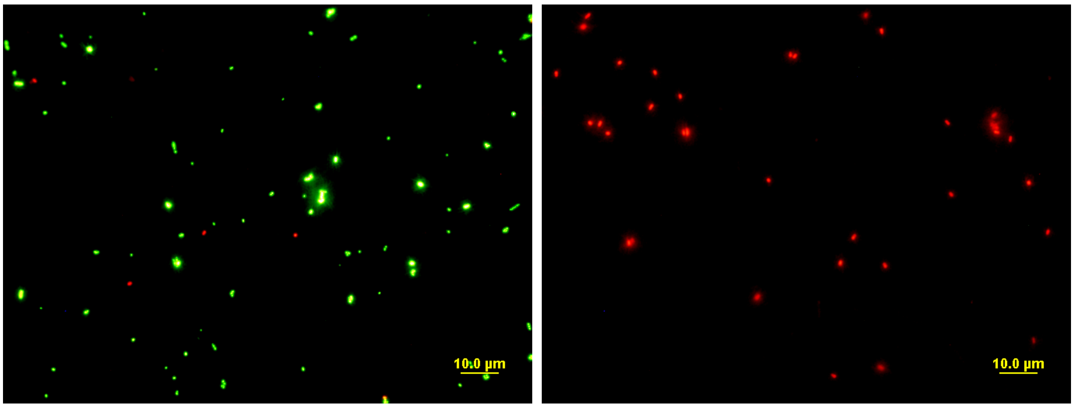

(a) (b)

FIGURE 4.41: Fluorescence images of the live and dead cells taken after exposure to Cu NPs for a period of 20 minutes.

obtained can be seen in 4.42 where due to a longer contact time between the Cu NPs and the bacteria, the number of dead cells,fig. 4.42(b) is seen to be significantly larger than the amount of live cells fig. 4.42(a). This is the case as more damage has occurred to the cells making it possible for PI to stain the damaged cells. After 120 mins exposure to Cu NP more copper ions are able to penetrate the damaged cell wall and cause cell lysis as described in 2.4.1.1.

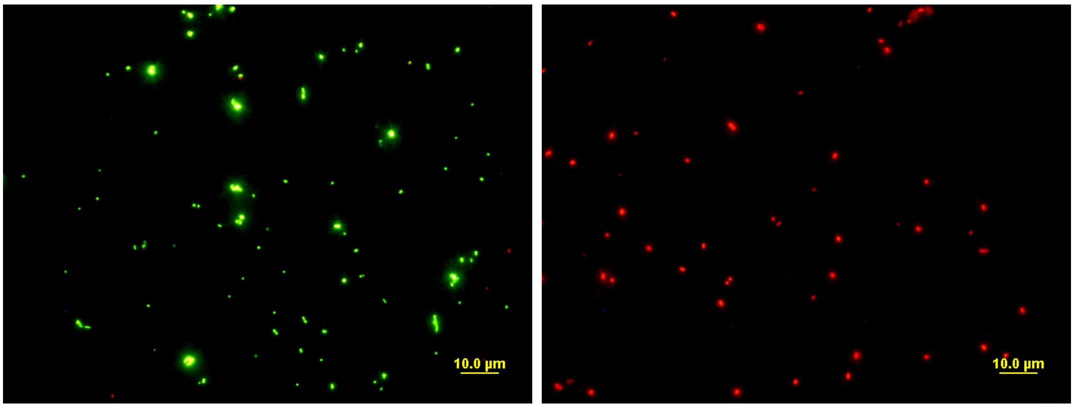

(a) (b)

FIGURE 4.42: Fluorescence images of the live and dead cells that were taken after exposure to Cu NPs for a period of 120 minutes.

Using the Fluorescence images shown in fig. 4.41 and fig. 4.42, the number of live cells and dead cells were counted and plotted. There is a difference between both the number of live and dead cells after 20 mins and 120 mins exposure to Cu NP. The number of live cells decreases from 110 at 20 mins to 74 at 120 mins. Furthermore the number of dead cells increases from 43 at 20 mins to 69 at 120 mins. This result is in accordance to those presented in 4.28, which also showed a decline in cell number after 120 mins.

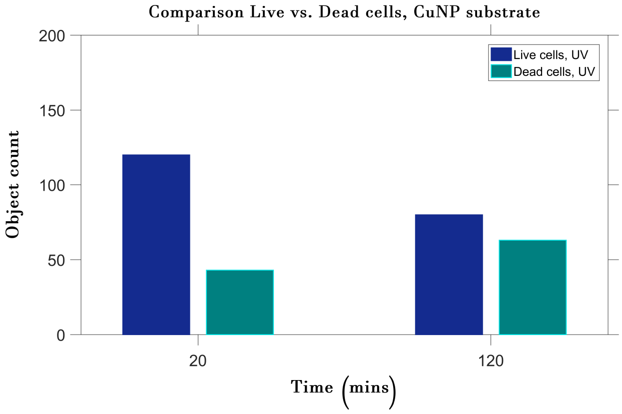

FIGURE 4.43: Plot showing the contrast between live and dead cells from 4.41 and 4.42 after 20 mins and 120 mins exposure.

There is a difference between the volumes pipetted for the flourescence microscopy tests and the viable tests. For flourescence measurements a volume of 5 µL is pippeted on the glass slide after the contact/exposure with the substrates. For the viable tests, 50 µL is used for plating. Despite the differnce when comparing the data presented in the tables, sections 4.3.2 and 4.3.2, there is a greater decrease in viable cells for the TiNP substrates than for the Cu NP. These results are consistent with those observed for the substrates same substrates in sections 4.2.1 and 4.2.2 where the efficiency for Cu NP substrates was shown to decrease after repeated cycles due to Cu NP degredation as was shown in fig. 4.32.

SUBSTRATE	*Control(20 mins)*	*Live cells(20 mins)*	*Control(120mins)*	*Live(120mins)*
glsCunp	140	110	112	74
Type 2 TiNP	125	99	122	82
Type 3 TiNP	120	89	126	75

TABLE 4.3: The number of viable *E.coli* cells after 20 mins and 120 minutes contact/-exposure to the Cu NP substrate and TiNP substrate for the fluorescence experiments.

The control substrate for Cu NP experiments is bare Si without any deposited copper clusters. The control for TiNP experiments are substrates containing TiNP, however these substrates are not exposed to UVA.

SUBSTRATE	*Control(0 mins)*	*Viable cells(20 mins)*	*Viable(120mins)*
glsCunp	200	143	174
Type 1 TiNP	515	324	292
Type 2 TiNP	513	300	274
Type 3 TiNP	513	212	200

TABLE 4.4: The number of viable *E.coli* cells after contact/exposure to the Cu NP and TiNP substrates after the seventh cycle.

In addition when comparing the TiNP bactericidal efficiency to Cu NPs, TiNP substrates shows a higher antibacterial activity due to the production of ROS after photoactivation and does not require direct contact with the bacteria as with Cu NPs. Bacteria once exposed to the photoactivated TiO_2 NPs are damaged and are unable to repair their cell wall making it possible for ROS to penetrate and cause further damage [86, 122].

Chapter 5

Conclusion and Outlook

The TiNP and Cu NP clusters for the polymer nanocomposites were produced using magnetron sputtering for this thesis and characterised by SEM and AFM respectively. TiNPs were found to be in the size regime of 19 to 20 nms whereas copper nanoparticles were found to be 33.6 nm ± 1 nm. During Cu NP deposition formation of monolayers was observed using AFM height analysis thereby causing a larger diameter distribution during particle analysis.Apart from height analysis, the AFM measurements gave an indication of a significant coverage of the deposited cluster on the PS film. Any variations for surface coverage was then done by altering the deposition time of the clusters. Subsequent annealing of the samples was used to control the immersion of the NP into the polymer matrix. The effect of annealing on Cu NP was then proven by AFM and optical measurements, that showed a decrease in height distribution and the improved plasmon peak for Cu NPs respectively. Apart from the characterization of prepared polymer nanocomposities, antibacterial experiments were also performed using the prepared substrates. Using the viable count method the antibacterial effect of the prepared substrates were quantified. The number of viable cells were counted after exposure to the different substrates under the same conditions. For TiNP the effect of photo-activating the substrate is compared to control experiments where the substrate is not activated with UV light. It is seen that there is a greater bactericidal efficiency for the TiNP substrates that are photo activated which is in accordance to the theory presented. Furthermore it is shown that the type 3 substrate is more effective than the type 1 and type 2 substrates. Repeated cycles using the same substrates were also carried out to investigate the bactericidal efficiency over repeated tests . The bactericidal efficiency for type 1 and 2 substrates is seen to be slightly higher at exposure times of 1 to 20 mins and then declines at 120 minutes. Additionally For type 3 substrates, the bactericidal efficiency is maintained over repeated cycles regardless of exposure time.

The antimicrobial effects of Cu NPs are also investigated in the same manner and are shown to initially have an adverse effect on the viability of bacterial cells, however this effect is reported to diminish after subsequent tests. The degradation of Cu NP is then reported using optical measurements in order to account for the loss of bactericidal efficiency. A significant advantage of the self sterilizing effect of TiNP coated surfaces also plays an important role for the lasting functionality of these TiNP coated surfaces in comparison to Cu NP coated surfaces that lose their bactericidal effect from oxidation.

Live/Dead assays were also performed after the efficiency tests. The results therein were used to show any membrane damage after exposure to Cu NP and TiNP substrates. In addition, using the fluorescence tests, the dead cells were visualized in contrast to the viable count method where only viable cells were considered. The results from these tests were also in agreement with those presented in the viable count method, showing that the TiNP substrates were more effective in killing the bacteria.

For future work the bactericidal efficiency of the prepared polymenr nanocomposities can be investigated. It has been shown that for the photocatalytic TiNPs, the efficiency can be enhanced by doping the NP with metal ions which can in turn improve the trapping to recombination ratio. Furthermore doping of these semiconductors would induce a bathochromic shift where the band gap would decrease resulting in photoactivation of these substrates in the visible light spectrum [80]. The release of copper ions can also be monitored to see if there is any decrease over repeated cycles. This can be done by using the metallochromic dye Alizarin Red S (ARS) which can bind to released copper ions forming a complex that absorbs at 510 nm [131]. SEM could also be implemented as an additional method to show any disruption in membrane integrity.

Appendix A

Matlab codes for the analysis of cluster height distribution, Annealing effects and Flourescent cells quantification

ANALYSIS OF CLUSTER HEIGHT DISTRIBUTION

```
clear global;
clear variables;

% Reading data from wsxm software (AFM images) that have been saved as text
% files
image_orig = dlmread('text_files/Cu35_center__NOTannealed Image 3.5um.txt');  % Reading height text file
image = mat2gray(image_orig);    % convert image to gray-scale image (normalizes it)
%image_max = max(image_orig(:));
phase_orig = dlmread('text_files/Cu35_center__NOTannealed_Phase3.5um.txt'); %reads the phase file saved as text as well
phase = mat2gray(phase_orig);

% Adjusting fg and bg here you will be able to adjust the treshold of the fore- and background
% The output image mybinaryimage(before,threshold range) replaces
% all pixels in the input image with luminance greater than level with the
% value 1 (white) and replaces all other pixels with the value 0 (black).
% Specify level in the range [0,1].This range is relative to the signal levels.
[image_fg,image_bg] = mybinaryimage(image,0.5,0.8);

saveas(gcf,'binary_radius_Cu35','epsc');
saveas(gcf,'binary_radius_Cu35','png');


% this is only if you want to crop your image
I = imread('binary_radius.png');
[I2, rect] = imcrop(I);

% Get points at this point you will chose what you consider to be clusters ( a hole in the analysis since
% you will be a bit bias :) left click to select then when selecting your last cluster right click )
blending(image_fg+0,phase);
[x, y] = getpts;
close;
working_fg = bwselect(image_fg,x,y,1);

% Plotting
figure;
plotting(image_orig(working_fg));

figure;
plotting(image_orig(image_bg));
```

```
% At this point one can then plot cluster height after having defined
 the
% background and foreground
figure;
plotting(image_orig(working_fg)-mean(image_orig(image_bg)));
%this is your figure  showing the foreground(clusters minus the
 background
%polymer film)


box,'on';

set(gca,'TickDir','out')
set(gca,'TickLength',[0.02 0.025])
set(gca,'FontSize',18)

%set(gcf,'Units','normalized','Position',...
%[0.00 0.0322 1.00 0.92])

set(gcf,'Units','normalized','Position',...
[0.00 0.0322 0.75 0.82])

title( '\bfHeight distribution of Cu_N
 clusters','FontSize',14,'Color','k');
legend( 'Diameter of particles', 'Distribution
 fit','Location', 'Northeast');
set(legend,'FontSize',14);
% Label axes
xlabel ('Height distribution
 (nm)','FontSize',14,'FontWeight','bold','Color','k')
ylabel ('\bfFrequency', 'FontSize',14,'FontWeight','bold','Color','k')
ylim([0 20])
xlim([10 60])

box,'on';
rez=500; %resolution (dpi) of final graphic
b1=gcf; %f is the handle of the figure you want to export
figpos=getpixelposition(b1); %dont need to change anything here
resolution=get(0,'ScreenPixelsPerInch'); %dont need to change anything
 here
%set(b1,'paperunits','inches','papersize',figpos(3:4)/
resolution,'paperposition',[0 0 figpos(3:4)/resolution]); %dont need
 to change anything here
set(b1,'paperunits','inches','papersize',figpos(3:4)/
resolution,'paperposition',[0 0 figpos(3:4)/resolution]); %dont need
 to change anything here
path='C:\Users\00jambazi\Desktop\NB3\particleanalysis\AFMmatlab
\CuNPs'; %the folder where you want to put the file
 name='HeightAFM_cu35'; %what you want the file to be called
print(b1,fullfile(path,name),'-dtiff',['-r',num2str(rez)],'-opengl')
```

Published with MATLAB® R2016a

ANALLYSIS OF CLUSTER HEIGHT DISTRIBUTION BEFORE AND AFTER ANNEALING

This will enable you to compare the height distribution before and after annealing your clusters

```
% Read Files where 'text_files/Cu_PS_Q.txt' looks for the text files
 saved from the wsxm program
% and converts them to matgrey scale
image_before = dlmread('text_files/Cu35_center__NOTannealed Image
 3.5um.txt');
image_after = dlmread('text_files/Cu35_center__annealed(3min)Image
 3.5um.txt');
before = mat2gray(image_before);
after = mat2gray(image_after);

% Binary Image Processing, where you can adjust the threshold of the
 images
% to select what u want to check the height of  by setting a range of
 the
% threshold.  The output image mybinaryimage(before,threshold range)
 replaces
% all pixels in the input image with luminance greater than level with
 the
% value 1 (white) and replaces all other pixels with the value 0
 (black).
% Specify level in the range [0,1].This range is relative to the
 signal levels.

%[before_fg,before_bg] = mybinaryimage(before,0.7,0.94); %for 1 min
%[after_fg,after_bg] = mybinaryimage(after,0.9,0.83);     %for 1 min

[before_fg,before_bg] = mybinaryimage(before,0.69,0.9); %for 3min
 analysis
[after_fg,after_bg] = mybinaryimage(after,0.9,0.8); %for 3 min
 analysis
before_max = max(image_before(:));
after_max = max(image_after(:));

% Plotting
figure;
plotting(image_before(before_fg));
figure;
plotting(image_before(before_bg));
figure;
plotting(image_after(after_fg));
figure;
plotting(image_after(after_bg));


% At this point the difference in mean for the foreground and
 background  before annealing are computed
%  and represents the height before Annealing. As for after annealing
 mean
%  values for the foreground and background are also subtracted to
 give the
```

```
%  height.
before_h = image_before(before_fg)- mean(image_before(before_bg));
after_h = image_after(after_fg) - mean(image_after(after_bg));
figure;
hold on;
box,'on';
plotting(before_h);
%str1 = {'Mean:28.1 nm','Std. Deviation: ','(\pm)' , '9.7'};
%annotation('textbox',...
  %  [0.766471449487555 0.601374570446735 0.129575402635432
 0.0927936787845888],...
  %  'Color',[1 0 0],...
  %  'String',{'Mean:31.8nm','Std. Deviation: (\pm) 7.4'},...
  %  'LineWidth',1.5,...
  %  'FontSize',11,...
  %  'FitBoxToText','off',...
  %  'EdgeColor',[1 0 0]);

plotting(after_h);
%str2 = {'Mean:28.1 nm','Std. Deviation: ','(\pm)' , '9.7'};
%annotation('textbox',...
  %  [0.766471449487555 0.506584601433329 0.129575402635432
 0.0859106508726927],...
  %  'Color',[0 0 1],...
  %  'LineWidth',1.5,...
  %  'FontSize',11,...
  %  'FitBoxToText','off',...
   % 'EdgeColor',[0 0 1]);
hold off;

box,'on';

set(gca,'TickDir','out')
set(gca,'TickLength',[0.02 0.025])
set(gca,'FontSize',18)
set(gcf,'Units','normalized','Position',...
[0.00 0.0322 0.75 0.82])
legend('Prior Annealing','Gaussian fit','Post Annealing, 3
 min','Gaussian fit','Location','NorthEast');
set(legend,'FontSize',14);
ylabel('Counts','FontWeight','bold','Color','k','FontSize',15)
xlabel('Height [nm]','FontWeight','bold','Color','k','FontSize',15)
xlim([-10 100])

title('Height distribution of Cu_N clusters before and after
 Annealing','FontWeight','bold','Color','k','FontSize',15)
box,'on';

rez=500; %resolution (dpi) of final graphic
b1=gcf; %f is the handle of the figure you want to export
figpos=getpixelposition(b1); %dont need to change anything here
resolution=get(0,'ScreenPixelsPerInch'); %dont need to change anything
 here
```

```
%set(b1,'paperunits','inches','papersize',figpos(3:4)/
resolution,'paperposition',[0 0 figpos(3:4)/resolution]); %dont need
 to change anything here
set(b1,'paperunits','inches','papersize',figpos(3:4)/
resolution,'paperposition',[0 0 figpos(3:4)/resolution]); %dont need
 to change anything here
%path='C:\Users\00jambazi\Desktop\NB3\particleanalysis\AFMmatlab
\CuNPs'; %the folder where you want to put the file
% name='Type1'; %what you want the file to be called
%print(b1,fullfile(path,name),'-dtiff',['-r',num2str(rez)],'-opengl')
```

Published with MATLAB® R2016a

ANALYSIS OF FLUORESCENCE CELLS WITH MATLAB

```
folder = 'G:\LIVEDEAD\Matlab Analysis\images analyzed'; % location
 specifier
baseFileName1 = 'Image13.png'; %Reads the individual image, of live or
 dead cells.


% Get the full filename, with path prepended.
fullFileName1 = fullfile(folder, baseFileName1);
if ~exist(fullFileName1, 'file')
 % Didn't find it there.  Check the search path for it.
 fullFileName1 = baseFileName1; % No path this time.
 if ~exist(fullFileName1, 'file')
  % Still didn't find it.  Alert user.
  errorMessage = sprintf('Error: %s does not exist.', fullFileName1);
  uiwait(warndlg(errorMessage));
  return;
 end
end

rgbImage1 = imread(fullFileName1);
% Get the dimensions of the image.  numberOfColorBands should be = 3.
[rows columns numberOfColorBands] = size(rgbImage1);
% Display the original color image.
%subplot(2, 4, 1);


%figure;
imshow(rgbImage1);

I = rgb2gray(rgbImage1);
%figure
%imshow(I)

%BW = imbinarize(I,0.09);
% BW = imbinarize(I) creates a binary image from image I by replacing
 all values above a globally...
...determined threshold with 1s and setting all other values to 0s. By
 default, imbinarize uses...
...Otsu's method, which chooses the threshold value to minimize the
 intraclass variance of the...
...thresholded black and white pixels. imbinarize uses a 256-bin image
 histogram to compute Otsu's threshold.


BW =
 imbinarize(I,'adaptive','ForegroundPolarity','bright','Sensitivity',0.1);
% Convert the image to a binary image using adaptive thresholding. Use
 the ForegroundPolarity..
...parameter to indicate that the foreground is darker/brighter than
 the background.
```

```
figure
imshow(BW)
%figure
%imshowpair(rgbImage1,BW,'montage')

%set(gcf,'Units','normalized','Position',...
%[0.00 0.0322 0.75 0.82])   code sets the position and size of image
%produced


cc = bwconncomp(BW);
number  = cc.NumObjects;

% CC = bwconncomp(BW) returns the connected components CC found in
 the...
...binary image BW. bwconncomp uses a default connectivity of 8 for
 two dimensions,...
    ...26 for three dimensions, and conndef(ndims(BW),'maximal') for
 higher dimensions.

%  PLOTING


y = [130 43 ; 119 63]; % CUNP test values for 20 and 120 mins live and
 dead cells
%y = [110 36 ; 132 88]; % TINP type 2
%y = [120 55 ; 115 108]; % TINP type 3

time = [20 120];
x = time ;
%xplot = 1:numel(time); %// Define modified x values


%b1 = bar(x,y);

set(b1(2),'FaceColor',[1 0 0],'EdgeColor',[0 0 0],'LineWidth',1.0);
set(b1(1),'FaceColor',[0 1 0],...
    'EdgeColor',[0 0 0],'LineWidth',1.0);
ylim([0 200])

title( '\bfComparison Live vs. Dead cells, CuNP
 substrate','FontWeight','bold','FontSize',12,'Color','k','FontName','Javanese
 Text');
legend( 'Live cells', 'Dead cells','Location', 'Northeast');
set(legend,'FontSize',14);
% Label axes
xlabel ('Time
 (mins)','FontSize',10,'FontWeight','bold','Color','k','FontName','Javanese
 Text')
ylabel ('Object
 count', 'FontSize',10,'FontWeight','bold','Color','k','FontName','Javanese
 Text')
```

```
box,'on';

set(gca,'TickDir','out')
set(gca,'TickLength',[0.02 0.025])
set(gca,'FontSize',18)

%set(gcf,'Units','normalized','Position',...
%[0.00 0.0322 1.00 0.92])

set(gcf,'Units','normalized','Position',...
[0.00 0.0322 0.75 0.82])

%set(gca,'plotboxaspectratio',[100 1 100]) % 4Length and 1 height

box,'on';
rez=500; %resolution (dpi) of final graphic
b1=gcf; %f is the handle of the figure you want to export
figpos=getpixelposition(b1); %dont need to change anything here
resolution=get(0,'ScreenPixelsPerInch'); %dont need to change anything
 here
%set(b1,'paperunits','inches','papersize',figpos(3:4)/
resolution,'paperposition',[0 0 figpos(3:4)/resolution]); %dont need
 to change anything here
set(b1,'paperunits','inches','papersize',figpos(3:4)/
resolution,'paperposition',[0 0 figpos(3:4)/resolution]); %dont need
 to change anything here
path='G:\LIVEDEAD\Matlab Analysis\images analyzed\plots'; %the folder
 where you want to put the file
 name='CuNPtest'; %what you want the file to be called
print(b1,fullfile(path,name),'-dtiff',['-r',num2str(rez)],'-opengl')
```

Published with MATLAB® R2016a

Bibliography

[1] C. M. J. Svetomir T Hitov, "Polystyrene- based nanocomposite materials and their antibacterial properties," 2016.

[2] R. P. Feynman, "There's plenty of room at the bottom," *Engineering and science*, vol. 23, no. 5, pp. 22–36, 1960.

[3] S. Noimark, C. Dunnill, M. Wilson, and I. Parkin, "The role of surfaces in catheter-associated infections," *Chemical Society Reviews*, vol. 38, no. 12, pp. 3435–3448, 2009. cited By 91.

[4] A. K. Chatterjee, R. Chakraborty, and T. Basu, "Mechanism of antibacterial activity of copper nanoparticles.," *Nanotechnology*, vol. 25, p. 135101, apr 2014.

[5] L. Hall-Stoodley, J. Costerton, and P. Stoodley, "Bacterial biofilms: From the natural environment to infectious diseases," *Nature Reviews Microbiology*, vol. 2, no. 2, pp. 95–108, 2004. cited By 1905.

[6] M. Madigan, *Brock Biology of Microorganisms*. Brock Biology of Microorganisms, Benjamin Cummings, 2012.

[7] A. Simchi, E. Tamjid, F. Pishbin, and A. R. Boccaccini, "Recent progress in inorganic and composite coatings with bactericidal capability for orthopaedic applications," *Nanomedicine*, vol. 7, pp. 22–39, 2011.

[8] S. Prabhu and E. K. Poulose, "Silver nanoparticles: mechanism of antimicrobial action, synthesis, medical applications, and toxicity effects," *International Nano Letters*, vol. 2, no. 1, pp. 1–10, 2012.

[9] L. Visai, L. De Nardo, C. Punta, L. Melone, A. Cigada, M. Imbriani, and C. R. Arciola, "Titanium oxide antibacterial surfaces in biomedical devices," vol. 34, pp. 929–946, 2011.

[10] K. Kon, M. Rai, *et al.*, "Metallic nanoparticles: mechanism of antibacterial action and influencing factors," *Journal of Comparative Clinical Pathology Research*, vol. 2, no. 1, pp. 160–174, 2013.

[11] P. Stoimenov, R. Klinger, G. Marchin, and K. Klabunde, "Metal oxide nanoparticles as bactericidal agents," *Langmuir*, vol. 18, no. 17, pp. 6679–6686, 2002.

[12] J. Kim, E. Kuk, K. Yu, J.-H. Kim, S. Park, H. Lee, S. Kim, Y. Park, Y. Park, C.-Y. Hwang, Y.-K. Kim, Y.-S. Lee, D. Jeong, and M.-H. Cho, "Antimicrobial effects of silver nanoparticles," *Nanomedicine: Nanotechnology, Biology, and Medicine*, vol. 3, no. 1, pp. 95–101, 2007.

[13] P. Appendini and J. Hotchkiss, "Review of antimicrobial food packaging," *Innovative Food Science and Emerging Technologies*, vol. 3, no. 2, pp. 113–126, 2002. cited By 600.

[14] J. Erichsen, J. Kanzow, U. Schürmann, K. Dolgner, K. Günther-Schade, . Thomas Strunskus, V. Zaporojtchenko, , and F. Faupel, "Investigation of the surface glass transition temperature by embedding of noble metal nanoclusters into monodisperse polystyrenes," *Macromolecules*, vol. 37, no. 5, pp. 1831–1838, 2004.

[15] R. D. Deshmukh and R. J. Composto, "Direct observation of nanoparticle embedding into the surface of a polymer melt," vol. 23, pp. 13169–13173, 2007.

[16] A. Pomogailo and V. Kestelman, *Metallopolymer Nanocomposites*. Materials science, Springer, 2005.

[17] D. B. Hamal, J. A. Haggstrom, G. L. Marchin, M. A. Ikenberry, K. Hohn, and K. J. Klabunde, "A multifunctional biocide/sporocide and photocatalyst based on titanium dioxide (TiO_2) codoped with silver, carbon, and sulfur.," *Langmuir : the ACS journal of surfaces and colloids*, vol. 26, pp. 2805–10, feb 2010.

[18] J. Kiwi, "Evidence for the mechanism of photocatalytic degradation of the bacterial wall membrane at the TiO_2 interface by ATR-FTIR and laser kinetic spectroscopy," *Langmuir*, vol. 21, no. 10, pp. 4631 – 4641, 2005.

[19] J. Alonso, *Structure and Properties of Atomic Nanoclusters.* Imperial College Press, 2005.

[20] R. Johnston, *Atomic and Molecular Clusters.* Master's Series in Physics and Astronomy, Taylor & Francis, 2002.

[21] H. Haberland, *Clusters of Atoms and Molecules: Theory, Experiment, and Clusters of Atoms.* Springer Series in Chemical Physics, Springer Berlin Heidelberg, 2013.

[22] P. J. Kelly and R. D. Arnell, "Magnetron sputtering: a review of recent developments and applications," vol. 56, pp. 159–172, 2000.

[23] V. N. Popok, "Beams of atomic clusters: Effects on impact with solids," vol. 11, pp. 19–45, 2006.

[24] L. Bardotti, B. Prével, P. Mélinon, A. Perez, Q. Hou, and M. Hou, "Deposition of au n clusters on au (111) surfaces. ii. experimental results and comparison with simulations," *Physical Review B*, vol. 62, no. 4, p. 2835, 2000.

[25] J. Blackman, *Metallic Nanoparticles.* Handbook of Metal Physics, Elsevier Science, 2008.

[26] S. A. Mody VV, Siwale R and M. HR, "Introduction to metallic nanoparticles," *Journal of Pharmacy and Bioallied Sciences.*, vol. 2, no. 4, pp. 282–289, 210.

[27] A. Heilmann, *Polymer Films with Embedded Metal Nanoparticles.* Springer Series in Materials Science, Springer Berlin Heidelberg, 2013.

[28] J. Prakash, J. C. Pivin, and H. C. Swart, "Noble metal nanoparticles embedding into polymeric materials: From fundamentals to applications," vol. 226, pp. 187–202, 2015.

[29] F. Faupel, V. Zaporojtchenko, T. Strunskus, and M. Elbahri, "Metal-polymer nanocomposites for functional applications," vol. 12, pp. 1177–1190, 2010.

[30] A. L. Stepanov, "Synthesis of silver nanoparticles in dielectric matrix by ion implantation: A review," vol. 26, pp. 1–29, 2010.

[31] D. K. Avasthi, Y. K. Mishra, D. Kabiraj, N. P. Lalla, and J. C. Pivin, "Synthesis of metal?polymer nanocomposite for optical applications," vol. 18, pp. 125604–, 2007.

[32] R. D. Deshmukh, , and R. J. Composto*, “Surface segregation and formation of silver nanoparticles created in situ in poly(methyl methacrylate) films,” *Chemistry of Materials*, vol. 19, no. 4, pp. 745–754, 2007.

[33] M. C. Tanzi, S. Bozzini, G. Candiani, A. Cigada, L. De Nardo, S. Farè, F. Ganazzoli, D. Gastaldi, M. Levi, P. Metrangolo, F. Migliavacca, R. Osellame, P. Petrini, G. Raffaini, G. Resnati, P. Vena, S. Vesentini, and P. Zunino, “Trends in biomedical engineering: focus on smart bio-materials and drug delivery,” vol. 9, pp. 87–97, 2011.

[34] E.-R. Kenawy, S. D. Worley, and R. Broughton, “The chemistry and applications of antimicrobial polymers: A state-of-the-art review,” vol. 8, pp. 1359–1384, 2007.

[35] H. A. Foster, I. B. Ditta, S. Varghese, and A. Steele, “Photocatalytic disinfection using titanium dioxide: spectrum and mechanism of antimicrobial activity,” vol. 90, pp. 1847–1868, 2011.

[36] D. Barber and I. Freestone, “An investigation of the origin of the colour of the lycurgus cup by analytical transmission electron microscopy,” *Archaeometry*, vol. 32, no. 1, pp. 33–45, 1990.

[37] A. K. Gupta and M. Gupta, “Synthesis and surface engineering of iron oxide nanoparticles for biomedical applications,” vol. 26, pp. 3995–4021, 2005.

[38] C. Louis and O. Pluchery, *Gold nanoparticles for physics, chemistry and biology.* World Scientific, 2012.

[39] K. Kelly, E. Coronado, L. Zhao, and G. Schatz, “The optical properties of metal nanoparticles: The influence of size, shape, and dielectric environment,” *Journal of Physical Chemistry B*, vol. 107, no. 3, pp. 668–677, 2003.

[40] A. Moores and F. Goettmann, “The plasmon band in noble metal nanoparticles: an introduction to theory and applications,” vol. 30, pp. 1121–1132, 2006.

[41] P. B. Johnson and R. W. Christy, “Optical constants of the noble metals,” vol. 6, pp. 4370–4379, 1972.

[42] U. Bogdanović, V. Vodnik, M. Mitrić, S. Dimitrijević, S. D. Škapin, V. Žunič, M. Budimir, and M. Stoiljković, "Nanomaterial with high antimicrobial efficacy—copper/polyaniline nanocomposite," *ACS Applied Materials & Interfaces*, vol. 7, no. 3, pp. 1955–1966, 2015. PMID: 25552193.

[43] H. Palza, "Antimicrobial polymers with metal nanoparticles," vol. 16, pp. 2099–2116, 2015.

[44] J. Prakash, A. Tripathi, S. Gautam, K. Chae, J. Song, V. Rigato, J. Tripathi, and K. Asokan, "Phenomenological understanding of dewetting and embedding of noble metal nanoparticles in thin films induced by ion irradiation," *Materials Chemistry and Physics*, vol. 147, no. 3, pp. 920 – 924, 2014.

[45] G. J. Kovacs and P. S. Vincett, "Formation and thermodynamic stability of a novel class of useful materials: Close-packed monolayers of submicron monodisperse spheres just below a polymer surface," vol. 90, pp. 335–351, 1982.

[46] G. J. Kovacs and P. S. Vincett, "Subsurface particle monolayer and film formation in softenable substrates: Techniques and thermodynamic criteria," vol. 111, pp. 65–81, 1984.

[47] A. G. Emslie, F. T. Bonner, and L. G. Peck, "Flow of a viscous liquid on a rotating disk," vol. 29, pp. 858–862, 1958.

[48] N. Sahu, B. Parija, and S. Panigrahi, "Fundamental understanding and modeling of spin coating process: A review," *Indian Journal of Physics*, vol. 83, no. 4, pp. 493–502, 2009.

[49] S. Middleman, *An Introduction to Fluid Dynamics: Principles of Analysis and Design.* New York:John Wiley and Sons, 1997.

[50] S. Hellstrom, "Basic models of spin coating," *Submitted as coursework for Physics*, vol. 210, 2007.

[51] C. Walsh and E. Franses, "Ultrathin pmma films spin-coated from toluene solutions," *Thin Solid Films*, vol. 429, no. 1-2, pp. 71–76, 2003. cited By 68.

[52] Y. Liu, T. P. Russell, M. G. Samant, J. Stöhr, H. R. Brown, A. Cossy-Favre, and J. Diaz, "Surface relaxations in polymers," *Macromolecules*, vol. 30, no. 25, pp. 7768–7771, 1997.

[53] K. Talaro, *Foundations of Microbiology: Brief Edition.* McGraw-Hill College, 1999.

[54] N. institute of Health, "Urinary tract infection in adults." http://www.niddk.nih.gov/health-information/health-topics/urologic-disease/urinary-tract-infections-in-adults/Pages/facts.aspx.

[55] J. A. Lemire, J. J. Harrison, and R. J. Turner, "Antimicrobial activity of metals: mechanisms, molecular targets and applications," vol. 11, pp. 371–384, 2013.

[56] P. Kenneth Todar, "Online textbook of bacteriology." http://textbookofbacteriology.net/index.html.

[57] C. R. Arciola, L. Montanaro, and J. W. Costerton, "New trends in diagnosis and control strategies for implant infections," vol. 34, pp. 727–736, 2011.

[58] I. Armentano, C. R. Arciola, E. Fortunati, D. Ferrari, S. Mattioli, C. F. Amoroso, J. Rizzo, J. M. Kenny, M. Imbriani, and L. Visai, "The interaction of bacteria with engineered nanostructured polymeric materials: A review," vol. 2014, pp. 1–18, 2014.

[59] K. Lewis, "Persister cells," vol. 64, pp. 357–372, 2010.

[60] J. P. Ruparelia, A. K. Chatterjee, S. P. Duttagupta, and S. Mukherji, "Strain specificity in antimicrobial activity of silver and copper nanoparticles," vol. 4, pp. 707–716, 2008.

[61] I. Perelshtein, G. Applerot, N. Perkas, E. Wehrschetz-Sigl, A. Hasmann, G. M. Guebitz, and A. Gedanken, "Antibacterial properties of an in situ generated and simultaneously deposited nanocrystalline ZnO on fabrics.," *ACS applied materials & interfaces*, vol. 1, pp. 361–6, feb 2009.

[62] W.-R. Li, X.-B. Xie, Q.-S. Shi, H.-Y. Zeng, Y.-S. Ou-Yang, and Y.-B. Chen, "Antibacterial activity and mechanism of silver nanoparticles on Escherichia coli.," *Applied microbiology and biotechnology*, vol. 85, pp. 1115–22, jan 2010.

[63] M. Raffi, F. Hussain, T. M. Bhatti, J. I. Akhter, A. Hameed, and M. M. Hasan, “Antibacterial characterization of silver nanoparticles against E.coli ATCC-15224,” *Journal of Materials Science and Technology*, vol. 24, no. 2, pp. 192–196, 2008.

[64] M. Raffi, S. Mehrwan, T. M. Bhatti, J. I. Akhter, A. Hameed, W. Yawar, and M. M. ul Hasan, “Investigations into the antibacterial behavior of copper nanoparticles against Escherichia coli,” *Annals of Microbiology*, vol. 60, pp. 75–80, feb 2010.

[65] U. Diebold, “The surface science of titanium dioxide,” *Elsevier*, vol. 48, pp. 53–229, 2003.

[66] N. A. Carrington and Z.-L. Xue, “Inorganic sensing using organofunctional sol–gel materials,” *Accounts of Chemical Research*, vol. 40, no. 5, pp. 343–350, 2007. PMID: 17465520.

[67] G. Grass, C. Rensing, and M. Solioz, “Metallic copper as an antimicrobial surface,” vol. 77, pp. 1541–1547, 2011.

[68] S. Shleev, J. Tkac, A. Christenson, T. Ruzgas, A. I. Yaropolov, J. W. Whittaker, and L. Gorton, “Direct electron transfer between copper-containing proteins and electrodes,” vol. 20, pp. 2517–2554, 2005.

[69] X. Liu, T. Lin, B. Peng, and X. Wang, “Antibacterial activity of capsaicin-coated wool fabric,” *Textile Research Journal*, vol. 82, no. 6, pp. 584–590, 2012.

[70] A. Azam, A. S. Ahmed, M. Oves, M. S. Khan, and A. Memic, “Size-dependent antimicrobial properties of cuo nanoparticles against gram-positive and -negative bacterial strains,” vol. 7, pp. 3527–3535, 2012.

[71] H. L. Karlsson, P. Cronholm, Y. Hedberg, M. Tornberg, L. De Battice, S. Svedhem, and I. O. Wallinder, “Cell membrane damage and protein interaction induced by copper containing nanoparticles–importance of the metal release process,” vol. 313, pp. 59–69, 2013.

[72] C. Gunawan, W. Y. Teoh, C. P. Marquis, and R. Amal, “Cytotoxic origin of copper(ii) oxide nanoparticles: Comparative studies with micron-sized particles, leachate, and metal salts,” vol. 5, pp. 7214–7225, 2011.

[73] L. Tamayo, M. Azócar, M. Kogan, A. Riveros, and M. Páez, “Copper-polymer nanocomposites: An excellent and cost-effective biocide for use on antibacterial surfaces,” vol. 69, pp. 1391–1409, 2016.

[74] E. Ghasemian, A. Naghoni, H. Rahvar, M. Kialha, and B. Tabaraie, “Evaluating the effect of copper nanoparticles in inhibiting pseudomonas aeruginosa and listeria monocytogenes biofilm formation,” vol. 8, 2015.

[75] C. W. e. a. Hoffmann MR, Martin ST, “Environmental applications of semiconductor photocatalysis.,” *Chem. Review*, vol. 95, pp. 69–96, 1995.

[76] C. Wei, W. Y. Lin, Z. Zainal, N. E. Williams, K. Zhu, A. P. Kruzic, R. L. Smith, and K. Rajeshwar, “Bactericidal activity of tio2 photocatalyst in aqueous media: Toward a solar-assisted water disinfection system,” vol. 28, pp. 934–938, 1994.

[77] O. J. Zhu X, Kim K and J. Y., “Surface analysis of anodic oxide film containing phosphorous on titanium.,” *Int. Journal Oral Maxillofac implants*, vol. 17, pp. 331–336, 2002.

[78] H. Zhang, “Thermodynamic analysis of phase stability of nanocrystalline titania,” vol. 8, pp. 2073–2076, 1998.

[79] T. B. Ghosh, S. Dhabal, and A. K. Datta, “On crystallite size dependence of phase stability of nanocrystalline tio2,” vol. 94, pp. 4577–4582, 2003.

[80] O. Carp, “Photoinduced reactivity of titanium dioxide,” vol. 32, pp. 33–177, 2004.

[81] A. Sclafani, “Comparison of the photoelectronic and photocatalytic activities of various anatase and rutile forms of titania in pure liquid organic phases and in aqueous solutions,” vol. 100, pp. 13655–13661, 1996.

[82] A. Selloni, “The adsorption of small molecules on the tio2 anatase (101) surface by first-principles molecular dynamics,” vol. 402-404, pp. 219–222, 1998.

[83] A. Vittadini, “Structure and energetics of water adsorbed at tio<inf>2</inf> anatase (101) and (001) surfaces,” vol. 81, pp. 2954–2957, 1998.

[84] B. Ohtani, “Photocatalytic activity of amorphous-anatase mixture of titanium(iv) oxide particles suspended in aqueous solutions,” vol. 101, pp. 3746–3752, 1997.

[85] Q. Guo, “Fundamental processes in surface photocatalysis on tio_2, language = Chinese, year = 2016, issn = 1000-6818, volume = 32, pages = 28–47, doi = 10.3866/PKU.WHXB201512081,,”

[86] A. Fujishima, X. Zhang, and D. Tryk, “Tio2 photocatalysis and related surface phenomena,” vol. 63, pp. 515–582, 2008.

[87] T. Matsunaga, “Photoelectrochemical sterilization of microbial cells by semiconductor powders,” vol. 29, pp. 211–214, 1985.

[88] J. Chen and C.-S. Poon, “Photocatalytic construction and building materials: From fundamentals to applications,” vol. 44, pp. 1899–1906, 2009.

[89] N. Suketa, T. Sawase, H. Kitaura, M. Naito, K. Baba, K. Nakayama, A. Wennerberg, and M. Atsuta, “An antibacterial surface on dental implants, based on the photocatalytic bactericidal effect,” vol. 7, pp. 105–111, 2005.

[90] N. S. Allen, M. Edge, J. Verran, J. Stratton, J. Maltby, and C. Bygott, “Photocatalytic titania based surfaces: Environmental benefits,” vol. 93, pp. 1632–1646, 2008.

[91] T. Matsunaga, R. Tomoda, T. Nakajima, N. Nakamura, and T. Komine, “Continuous-sterilization system that uses photosemiconductor powders.,” vol. 54, pp. 1330–1333, 1988.

[92] C. Hu, J. Guo, J. Qu, and X. Hu, “Photocatalytic degradation of pathogenic bacteria with agi/tio_2 under visible light irradiation,” vol. 23, pp. 4982–4987, 2007.

[93] V. S. R. Kambalal, V. S. R. Kambala, and R. Naidu, “Disinfection studies on tio_2 thin films prepared by solgel method,” vol. 5, pp. 121–129, 2009.

[94] W. J. Wang, J. C. Yu, P. K. Wong, and B. Xu, “Photocatalysts for solar-induced water disinfection: New developments and opportunities,” vol. 734, pp. 63–89, 2012.

[95] K. Sunada, T. Watanabe, and K. Hashimoto, “Studies on photokilling of bacteria on tio_2 thin film,” vol. 156, pp. 227–233, 2003.

[96] Y. Nosaka, T. Daimon, A. Y. Nosaka, and Y. Murakami, “Singlet oxygen formation in photocatalytic tio2 aqueous suspension,” *Phys. Chem. Chem. Phys.*, vol. 6, pp. 2917–2918, 2004.

[97] T. Berger, M. Sterrer, O. Diwald, and E. Knözinger, "Charge trapping and photoadsorption of o2 on dehydroxylated tio2 nanocrystals–an electron paramagnetic resonance study," vol. 6, pp. 2104–2112, 2005.

[98] D. S. Muggli and F. J.L., "Parallel pathways for photocatalytic decomposition of acetic acid on tio2," vol. 187, pp. 230–237, 1999.

[99] Y. Kikuchi, K. Sunada, T. Iyoda, K. Hashimoto, and A. Fujishima, "Photocatalytic bactericidal effect of tio2 thin films: dynamic view of the active oxygen species responsible for the effect," *Journal of Photochemistry and Photobiology A: Chemistry*, vol. 106, no. 1–3, pp. 51 – 56, 1997.

[100] M. Hanif, *Synthesis of Nanostructured Materials Using Metal Cluster Ion Beams.* PhD thesis, Aalborg University, 2016.

[101] O. applied research, "Nanocluster deposition source-model nc200u-b." http://www.oaresearch.co.uk/oaresearch/cluster/.

[102] H. Hartmann, V. N. Popok, I. Barke, V. Von Oeynhausen, and K. H. Meiwes-Broer, "Design and capabilities of an experimental setup based on magnetron sputtering for formation and deposition of size-selected metal clusters on ultra-clean surfaces," vol. 83, pp. 073304–, 2012.

[103] A. Shelemin, O. Kylian, J. Hanuvs, A. Choukourov, I. Melnichuk, A. Serov, D. Slavínska, and H. Biederman, "Preparation of metal oxide nanoparticles by gas aggregation cluster source," vol. 120, pp. 162–169, 2015.

[104] P. Bio-research, "Methodological instructions to lesson." https://www.pinterest.com/pin/201043570844528477/.

[105] F. o. S. Bruno Vieira, University of Lisbon, "Colony counter." https://imagej.nih.gov/ij/plugins/colony-counter.html.

[106] F. o. S. Cesarino Mario Jeppesen, Aalborg University, "Colony counter." Image produced for Thesis.

[107] J. Woollam, "Ellipsometry data analysis." https://www.jawoollam.com/resources/ellipsometry-tutorial/ellipsometry-data-analysis.

[108] S. I. GmbH, "Uv / vis / nir spectroscopic ellipsometer se 850." http://eavangard-micro.ru/files/SE850.pdf.

[109] M. Losurdo, M. Bergmair, G. Bruno, D. Cattelan, C. Cobet, A. De Martino, K. Fleischer, Z. Dohcevic-Mitrovic, N. Esser, M. Galliet, R. Gajic, D. Hemzal, K. Hingerl, J. Humlicek, R. Ossikovski, Z. V. Popovic, and O. Saxl, "Spectroscopic ellipsometry and polarimetry for materials and systems analysis at the nanometer scale: state-of-the-art, potential, and perspectives," vol. 11, pp. 1521–1554, 2009.

[110] P. Eaton and P. West, *Atomic Force Microscopy.* 2010.

[111] N.-M. S. instruments, "Amplitude modulation afm." http://www.ntmdt-si.com/spm-principles/view/semicontact-techniques.

[112] N. Tkachenko, *Optical Spectroscopy.* 2006.

[113] J. R. Lakowicz, ed., *Principles of fluorescence spectroscopy*, pp. 1–954. 2006.

[114] J. R. Albani, ed., *Principles and Applications of Fluorescence Spectroscopy*, pp. 1–255. 2008.

[115] K. R. Spring, "introduction to fluorescence microscopy." Scientific Consultant, Lusby, Maryland,.

[116] M. W. Davidson, "introduction to fluorescence microscopy." National High Magnetic Field Laboratory,.

[117] N.-M. S. instruments, "Live/dead baclight bacterial viability kit, for microscopy." https://www.thermofisher.com/order/catalog/product/L7007.

[118] M. W. Davidson, "Fluorescence microscopes." http://www.olympusmicro.com/primer/techniques/fluo

[119] MATLAB, *version 9.0.0.341360 (R2016a).* Natick, Massachusetts: The MathWorks Inc., 2016.

[120] I. Barke, H. Hartmann, D. Rupp, L. Flückiger, M. Sauppe, M. Adolph, S. Schorb, C. Bostedt, R. Treusch, C. Peltz, S. Bartling, T. Fennel, K. H. Meiwes-Broer, and T. Möller, "The 3d-architecture of individual free silver nanoparticles captured by x-ray scattering," vol. 6, pp. 6187–, 2015.

[121] T. Verdier, M. Coutand, A. Bertron, and C. Roques, “Antibacterial activity of tio2 photocatalyst alone or in coatings on e. coli: The influence of methodological aspects,” *Coatings*, vol. 4, no. 3, pp. 670–686, 2014.

[122] P. S. M. Dunlop, J. A. Byrne, N. Manga, and B. R. Eggins, “The photocatalytic removal of bacterial pollutants from drinking water,” vol. 148, pp. 355–363, 2002.

[123] C. S. P. Muranyi and J. Wunderlich, “Antimicrobial efficiency of titanium dioxide-coated surfaces,” *Journal of Applied Microbiology*, vol. 108, pp. 1966–1973, 2009.

[124] P. C. Maness, “Bactericidal activity of photocatalytic tio2 reaction: Toward an understanding of its killing mechanism,” vol. 65, pp. 4094–4098, 1999.

[125] Y. Ohko, “Self-sterilizing and self-cleaning of silicone catheters coated with tio2 photocatalyst thin films: A preclinical work,” vol. 58, pp. 97–101, 2001.

[126] K. P. Kühn, I. F. Chaberny, K. Massholder, M. Stickler, V. W. Benz, H. G. Sonntag, and L. Erdinger, “Disinfection of surfaces by photocatalytic oxidation with titanium dioxide and uva light,” vol. 53, pp. 71–77, 2003.

[127] M. Machida, K. Norimoto, and T. Kimura, “Antibacterial activity of photocatalytic titanium dioxide thin films with photodeposited silver on the surface of sanitary ware,” vol. 88, pp. 95–100, 2005.

[128] B. Kim, D. Kim, D. Cho, and S. Cho, “Bactericidal effect of tio2 photocatalyst on selected food-borne pathogenic bacteria,” vol. 52, pp. 277–281, 2003.

[129] D. Mitoraj, A. Jańczyk, M. Strus, H. Kisch, G. Stochel, P. B. Heczko, and W. Macyk, “Visible light inactivation of bacteria and fungi by modified titanium dioxide,” vol. 6, pp. 642–648, 2007.

[130] S. Banerjee, D. D. Dionysiou, and S. C. Pillai, “Self-cleaning applications of tio2 by photo-induced hydrophilicity and photocatalysis,” vol. 176-177, pp. 396–428, 2015.

[131] M. N. Yazdinejad, “Spectrophotometric determination of trace amount of copper(ii) ion based on complexation with an anthraquinone derivative,” *Analytical Sciences*, vol. 22, no. 4, pp. 617–619, 2006.